DISSERTATION

# BARIUM EXTRACTION FROM LIQUID XENON ON A CRYOPROBE FOR THE NEXO EXPERIMENT AND A NUCLEON DECAY SEARCH USING EXO-200 DATA

Submitted by

Adam B. Craycraft

Department of Physics

In partial fulfillment of the requirements

For the Degree of Doctor of Philosophy

Colorado State University

Fort Collins, Colorado

Fall 2019

Doctoral Committee:

Advisor: William M. Fairbank, Jr.

Jacob Roberts
Robert Wilson
Thomas E. Johnson

ABSTRACT

BARIUM EXTRACTION FROM LIQUID XENON ON A CRYOPROBE FOR THE NEXO EXPERIMENT AND A NUCLEON DECAY SEARCH USING EXO-200 DATA

Neutrinoless double beta decay ($0\nu\beta\beta$) is a theorized decay that is beyond the standard model of particle physics. Observation of this decay would establish the Majorana nature of neutrinos and show violation of lepton number. Nucleon decay is another theorized decay that is beyond the standard model of particle physics that would violate baryon number. Observation of baryon number violation has been pursued for sometime in a wide variety of experiments. EXO-200 is an experiment that utilized a time projection chamber (TPC) filled with liquid xenon (LXe) enriched in the isotope xenon-136 to search for $0\nu\beta\beta$. In this thesis, an analysis of EXO-200 data in search of evidence for triple-nucleon decays in $^{136}$Xe is presented. Decay of $^{136}$Xe to $^{133}$Sb and decay to $^{133}$Te were the particular decays searched for in this analysis. No evidence for either decay was found. Limits on the lifetimes of these decays were set that exceed all prior limits. The proposed nEXO experiment will be next generation LXe TPC search for $0\nu\beta\beta$. In order to eliminate background events that are not associated with two neutrino double beta decay, a technique to tag the barium-136 decay daughter is under development. In this thesis, continued development is presented of a scheme to freeze the barium daughter in a solid xenon sample on the end of a cryoprobe dipped into LXe and subsequently tag it using its fluorescence in the solid matrix.

# ACKNOWLEDGEMENTS

I must first acknowledge God who made the universe and apportioned me the lavish gift of seeking to understand it. For giving me the circumstances, ability, and object of this study I thank you. Sarah, thank you for supporting me in this effort through some undeniably trying circumstances. I love you so much. Without you I would never have made it here. Henry and Norah, you are the reason I finished this thing. You're both so amazing, and I cannot wait to share what I've learned with you. To my family I can only say that you made me who I am and I love each of you deeply: Dad, Mom, Ben, Anna, and Abby. I am also grateful to my scientific colleagues and friends Cesar, Kendy, Chris, Tim, Alec, James, Trey, and David. You each helped in your own way to make this work possible. Jon Gilbert deserves momentous thanks for his moral support as we slogged through this race together. Finally, to my advisor, William Fairbank Jr. I offer my gratitude for giving me the opportunity to do this work and for sharing your insights which made it possible. I must also thank you for graciously giving me many chances to fail while still supporting me faithfully. You also supported me through many hard personal times with astonishing grace. For that I thank you as well. This work was supported by the National Science Foundation under grants number PHY-1649324 and number PHY-1132428 and by the Department of Energy under award number DE-FG02-03ER41255.

TABLE OF CONTENTS

# Chapter 1

# Introduction

Wolfgang Pauli first postulated the existence of the neutrino in 1930 in order to understand the phenomenon of beta decay. He proposed that a small neutral particle was responsible for carrying away the energy that was missing from $\beta$ decay experiments. This particle is now known as the neutrino and was first detected by Fred Reines and Clyde Cowan in 1956 [1]. It is a very low mass, neutral particle that interacts only via the weak nuclear force. It comes in three flavors; electron ($\nu_e$), muon ($\nu_\mu$), and tau ($\nu_\tau$). They were originally thought to be massless, but all recent experimental evidence indicates that they do have mass. What mechanism it is that provides this mass remains in question, as does the absolute scale of the mass. One of the primary ways to answer these questions is via the detection of neutrinoless double $\beta$ decay ($0\nu\beta\beta$) [2]. Observation of this decay would establish that neutrinos are Majorana particles i.e. their own antiparticles. It would also demonstrate violation of lepton number conservation [3]. These two demonstrations would have huge impacts on the understanding of the universe.

Beta minus ($\beta$) decay occurs when a neutron transforms into a proton, expelling an electron and an anti-neutrino. The Feynman diagram for this decay is shown in Fig.1.1. Double $\beta$ decay occurs in various even-even nuclei in which single $\beta$ decay is forbidden. Two electrons are emitted in the double $\beta$ decay. These electrons carry away all of the decay energy in the case of $0\nu\beta\beta$ or less than the total decay energy in the case of two neutrino double $\beta$ decay ($2\nu\beta\beta$).

Lepton number conservation is a symmetry that has never been shown to be broken. A similar conservation principle is baryon number conservation. Lepton number conservation would be violated by $0\nu\beta\beta$. Baryon number conservation is violated in the case of decays of particles in the nucleus. These decays are called nucleon decays. This thesis focuses on work done in search of nucleon decays and work done to help develop experiments searching for $0\nu\beta\beta$. Baryon number violation is a crucial aspect of many potential theories regarding baryogenesis. Theories of baryogenesis seek to answer the question, why is there no excess of anti-matter on macroscopic

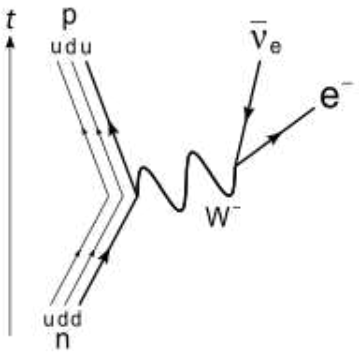


**Figure 1.1:** The Feynman diagram for beta decay. The neutrino was originally postulated because the electron emitted with this decay was measured at a lower energy than expected [6].

scales while there is clearly an excess of matter. It has been shown that there are no regions of excess anti-matter in the entire observable universe [4]. Baryon number conservation must be violable by interactions on some scale in order for this apparent global excess of baryons to exist. This fact is set down theoretically in the three Sakharov conditions [5]. Baryon number violation is the first condition. the other two are charge and charge-parity symmetry violation and the possibility that these interactions can occur outside of thermal equilibrium.

## 1.1 Neutrinos

Neutrinos are known to be produced in one of three flavor states defined by the flavor of charged lepton with which it is produced. Thus neutrinos associated with $\beta$ decay are electron flavor. For many years it was assumed that neutrinos were massless. However, in the late 1960's Ray Davis first detected an apparent lack of $\nu_e$'s arriving from the sun in the Homestake Solar Neutrino Detector [7]. This experiment was carried out at the Homestake Mine in South Dakota. It used a radiochemical detection technique based on an inverse $\beta$ reaction in $^{37}$Cl:

$$\nu_e + {}^{37}\mathrm{Cl} \rightarrow {}^{37}\mathrm{Ar} + e^- \tag{1.1}$$

The $\nu_e$ in this reaction can be generated by various reaction chains in the sun. Thus the experimenters expected to see a specific amount of inverse $\beta$ decays in their detector based on calcula-

tions of the rate of $\nu_e$ production in the sun. They saw only about a third of the expected signal. The experiment eventually accumulated a very large dataset that confirmed this discrepancy [7].

The puzzle was resolved when it was confirmed that neutrinos oscillate between flavor states [8]. Oscillations occur because neutrinos have a basis of mass eigenstates that are distinct from the flavor eigenstates. This means that the flavor eigenstates can be written as:

$$|\nu_\alpha\rangle = \sum_i U^*_{\alpha i} |m_i\rangle \tag{1.2}$$

where the $\alpha$'s are the flavor states ($e$,$\mu$,$\tau$), the $i$'s are the mass states (1,2,3) and $U^*_{\alpha i}$ is the Pontecorvo-Maki-Nakagawa-Sakata (PMNS) mixing matrix [9]. This matrix can be written as:

$$U = \begin{pmatrix} 1 & 0 & 0 \\ 0 & c_{23} & s_{23} \\ 0 & -s_{23} & c_{23} \end{pmatrix} \begin{pmatrix} c_{13} & 0 & s_{13}e^{-i\delta} \\ 0 & 1 & 0 \\ -s_{13}e^{i\delta} & 0 & c_{13} \end{pmatrix} \begin{pmatrix} c_{12} & s_{12} & 0 \\ -s_{12} & c_{12} & 0 \\ 0 & 0 & 1 \end{pmatrix} \begin{pmatrix} 1 & 0 & 0 \\ 0 & e^{i\frac{\alpha_1}{2}} & 0 \\ 0 & 0 & e^{i\frac{\alpha_2}{2}} \end{pmatrix} \tag{1.3}$$

where $c_{ij} \equiv \cos\theta_{ij}$ and $s_{ij} \equiv \sin\theta_{ij}$. The $\theta_{ij}$ are the mixing angles between mass state i and j. There are also up to three Charge-Parity (CP) violating phases $\delta$, $\alpha_1$, and $\alpha_2$. The $\alpha$'s are associated with Majorana neutrinos.

As a simplified illustration of the relationship between neutrino flavor oscillation and non-zero mass consider a two flavor oscillation scenario. In this case there is one mixing angle $\theta$ and one mass squared difference $\Delta m^2$. The Hamiltonian $H$ and mixing matrix $U$ can be written:

$$\begin{aligned} H &= \frac{c^4}{4E\hbar} \begin{pmatrix} -\Delta m^2 & 0 \\ 0 & \Delta m^2 \end{pmatrix} \\ U &= \begin{pmatrix} \cos\theta & \sin\theta \\ -\sin\theta & \cos\theta \end{pmatrix} \end{aligned} \tag{1.4}$$

where $E$ is the energy of the neutrino, $c$ is the speed of light and $\hbar$ is the reduced Planck constant. Beginning with a pure electronic state such as a neutrino originating from the sun and allowing it to propagate through time with a defined mass, the time-dependent flavor state becomes:

$$\begin{aligned} |\nu(t)\rangle = (e^{itc^4\Delta m^2/4E\hbar}\cos^2\theta + e^{-itc^4\Delta m^2/4E\hbar}\sin^2\theta)\,|\nu_e\rangle \\ + \cos\theta\sin\theta(-e^{itc^4\Delta m^2/4E\hbar} + e^{-itc^4\Delta m^2/4E\hbar})\,|\nu_\mu\rangle \end{aligned} \tag{1.5}$$

From Eq. 1.5 it can be seen that if the mass basis is identical to the flavor basis (i.e. $\theta = 0$), then there is no probability of oscillation to the muonic state. This is also true in the case where $\Delta m^2 = 0$. Therefore, the observation of neutrino oscillation indicates the existence of distinct neutrino masses and, thus, at least one of the two distinct masses is non-zero.

The probability of oscillation from an electron neutrino to muon neutrino over a given time can be derived from Eq. 1.5. It can be expressed in terms of the baseline ($L$) of the neutrino flight as:

$$P(\nu_e \to \nu_\mu) = \sin^2 2\theta \sin^2(\frac{c^4\Delta m^2}{4E\hbar c}L) \tag{1.6}$$

From this equation it can be seen that two flavor oscillation depends on $\Delta m^2$ not the individual masses. The full three flavor oscillation scenario results in analogous expressions for oscillation probability. In that case, there are 3 mass-squared differences ($\Delta m^2_{12}$, $\Delta m^2_{13}$, and $\Delta m^2_{23}$) and the three mixing angles. Oscillation experiments measure the appearance or disappearance of the various flavors after a flight over a given $L$ and $E$. An experiment with a certain $L$ and $E$ will be more sensitive to specific mixing angles and mass-squared differences. For example, solar neutrino experiments like the Homestake experiment are more sensitive to $\theta_{12}$ and $\Delta m^2_{12}$. For this reason $\Delta m^2_{12}$ is also known as $\Delta m^2_{sol}$. For $\Delta m^2_{23}$, atmospheric experiments are more sensitive, so it is known as $\Delta m^2_{atm}$. The results of oscillation experiments are summarized in table 1.1.

There remain two primary questions associated with this picture of neutrino masses. First the absolute scale of the neutrino mass is not known. Second the sign of $\Delta m_{23}$ is not known. So it is possible that mass state 1 is the lightest. This arrangement is called the Normal Hierarchy (NH).

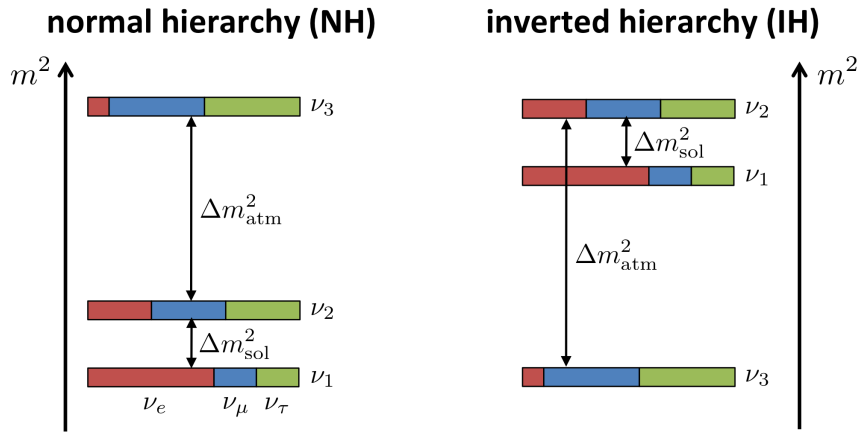


**Figure 1.2:** Neutrino mass hierarchies represented graphically. The color bars indicated the flavor mixture of each mass state. The vertical dimension represents the relative masses of the mass eigenstates [10] .

The case in which mass state 3 is the lightest is known as the Inverted Hierarchy (IH). These mass relationships are represented in Fig. 1.2 If the neutrino is a Majorana particle, neutrinoless double $\beta$ decay experiments may help in determining the absolute mass scale and the hierarchy.

## 1.2 Double Beta Decay

If neutrinos are their own anti-particle i.e. Majorana particles, then $0\nu\beta\beta$ maybe possible. A Feynman diagram of $0\nu\beta\beta$ is shown in Fig. 1.3. Double $\beta$ decay is a nuclear decay that typically involves two anti-neutrinos ($2\nu\beta\beta$). It occurs in even-even nuclei in which single $\beta$ decay is

**Table 1.1:** Best-fit values for neutrino oscillation parameters are listed from [9]. The values(in parentheses) are for the NH(IH). The $3\sigma$ allowed region is listed in all cases except for $\delta/\pi$ where the values in the final column of that row are the $2\sigma$ allowed values. For the splitting between mass states 1 and 2 there is no distinction between NH and IH. Thus there is no value in parentheses in the rows associated with that splitting.

| Parameter | Best-Fit | $3\sigma$ |
|---|---|---|
| $\Delta m^2_{21}$ [$10^{-5}$ eV$^2$] | 7.37 | 6.93 - 7.96 |
| $\Delta m^2_{31(23)}$ [$10^{-3}$ eV$^2$] | 2.56(2.54) | 2.45 - 2.69(2.42 - 2.66) |
| $\sin^2\theta_{12}$ | 0.297 | 0.250 - 0.354 |
| $\sin^2\theta_{23}$ | 0.425(0.589) | 0.381 - 0.615(0.384 - 0.636) |
| $\sin^2\theta_{13}$ | 0.0215(0.216) | 0.0190 - 0.0240(0.0190 - 0.0242) |
| $\delta/\pi$ | 1.38(1.31) | 1.0 - 1.9(0.92-1.88) |

energetically forbidden. It has been observed in a number of such nuclei including $^{136}$Xe. The half-life for $2\nu\beta\beta$ in $^{136}$Xe is reported in [11] as:

$$\mathrm{T}_{1/2}^{2\nu\beta\beta} = 2.165 \pm 0.016(\mathrm{statistical}) \pm 0.059(\mathrm{systematic}) \times 10^{21}\mathrm{yr} \tag{1.7}$$

For $2\nu\beta\beta$, since some of the energy is carried off by the neutrinos, the observed energy of the decay will be less than the Q-value, which is defined as the difference between the initial and final energies of all decay components. In the case of $0\nu\beta\beta$, the measured energy of the decay will be close to the Q-value of the decay. Fig. 1.4 shows the energy spectra for the case that $0\nu\beta\beta$ occurs $10^{-4}$ as often as $2\nu\beta\beta$. This difference in energy spectrum is the an experimentally observable distinction between the two decay modes. Neutrinoless double $\beta$ decay has not yet been observed. Limits on its half-life have been established in Xe$^{136}$ up to the level of $10^{26}$ yr by the KamLAND-Zen (KZ) experiment [12]. The half-life of $0\nu\beta\beta$ can be expressed as

$$\frac{1}{\mathrm{T}_{1/2}^{0\nu}} = G^{0\nu}|M^{0\nu}|^2|\langle m_{\beta\beta}\rangle|^2 \tag{1.8}$$

where $G^{0\nu}$ is the phase space factor, $M^{0\nu}$ is the nuclear matrix element, and $\langle m_{\beta\beta}\rangle$ is the effective neutrino mass. The effective (or Majorana) neutrino mass can be written as:

$$\langle m_{\beta\beta}\rangle = \Big|\sum_{i=1}^{3} U_{ei}^2 m_i\Big| \tag{1.9}$$

Eq. 1.8 shows that a measurement or limit on the half-life can be translated into a measurement or limit on the effective neutrino mass for a given nuclear matrix element value $|M^{0\nu}|^2$. Because there is a range of these values, the KZ collaboration reports an upper limit on the neutrino mass over a range of 60-161 meV. A phase space plot of the minimum neutrino mass and $\langle m_{\beta\beta}\rangle$ with the exclusion from this limit is shown in Fig. 1.5 [12].

## 1.3 The EXO-200 Experiment

The Enriched Xenon Observatory (EXO-200) is a $0\nu\beta\beta$ search that makes use of the liquid xenon time projection chamber (TPC) technology to measure the energy of events occurring within the liquid. Liquid xenon serves as both the source of events and detection medium for the experiment. When an energy deposit occurs energy goes into two primary phenomena, ionization and scintillation. Ionization produces free electrons that are drifted via the electric field to wires that detect them. The LXe scintillation occurs at a wavelength of 178 nm and is detected by a plane of photo-detectors on the ends of the detector. The EXO-200 detector consists of two LXe TPCs placed back to back sharing a central cathode. It has a total of $\sim$190 kg of LXe enriched to 80.7% abundance of $^{136}$Xe. A schematic depiction of the TPC is shown in Fig. 1.6. A central cathode is held at high voltage [14]. On the end caps of the detector an anode plane is at virtual ground. Field shaping rings form a cylinder on the outside of the detector creating a uniform electric field within.

Ionization creates a cloud of electrons that are drifted to the anodes where they create an induction current as they drift past a set of wires (V-wires) and are collected on another set (U-wires). The U and V wires are separated by 6 mm in the z-direction defined along the axis of the detector. They are also oriented 60° from one another. The charge signal on the U-wires is used to measure the ionization energy associated with an energy deposit. Fig. 1.7 shows a schematic of these two wire planes. The U and V-wires together provide x and y-coordinates perpendicular to the axis of the detector. The z coordinate of the energy deposit is obtained from the time difference, $\Delta t$,

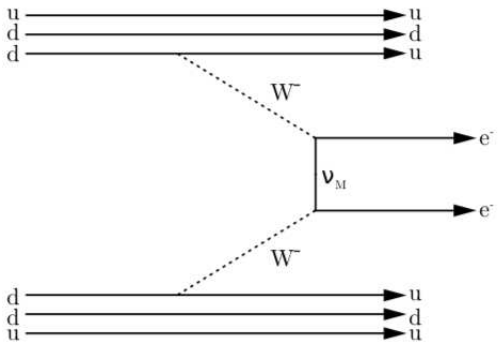


**Figure 1.3:** Feynamn diagram of neutrinoless double $\beta$ decay, in which no neutrinos are emitted from the nucleus. Instead the Majorana neutrinos ($\nu_M$) are exchanged [13].

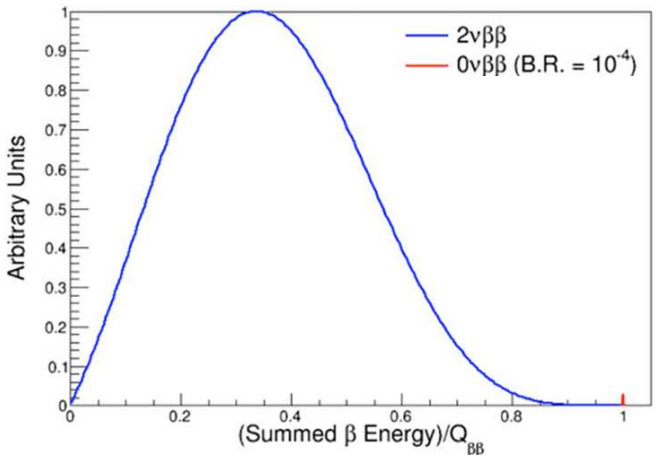


**Figure 1.4:** Energy spectra of $2\nu\beta\beta$ and $0\nu\beta\beta$ with a branching ratio of $10^{-4}$. This indicates the observable distinction between the two decay modes. Increased here for aesthetic purposes, the actual branching ratio is necessarily $< 10^{-5}$ based on current half-life limits.

between the flash of scintillation light and the arrival of the electrons at the charge tiles using: $z = v_{drift}\Delta t$, where $v_{drift}$ is the known drift velocity of electrons in LXe for the particular field. The z-coordinate is obviously required to give 3D reconstruction of events, but it is also used to correct the charge signal since electrons may be absorbed by impurities in the LXe as they travel to the anode. The nearer the cathode an energy deposit occurs the more it will be attenuated by this effect. The electron lifetime in the detector is measured periodically in order to give a correction that accurately captures the z-dependence of this effect. The scintillation is detected by large area avalanche photo diodes (LAAPDs), which sit 6 mm behind the U-wires [14]. The LAAPDs were chosen to provide good quantum efficiency at the scintillation wavelength as well as low radioactivity. They are attached directly to specially built support platters without their typical ceramic casings. This decreases radioactivity and mechanical stress caused by cryogenic temperatures.

As stated above, the crucial observable that allows for the detection of $0\nu\beta\beta$ is the energy of events in the LXe. Therefore a critical consideration regarding experimental sensitivity is events in the detector that have energy at or near the Q-value but are not caused $0\nu\beta\beta$ decays. These are called background events. One source of backgrounds are Compton scatters of gamma rays emitted from materials composing or outside of the detector. EXO-200 employs several strategies to reduce these background events. One of which is to use the LXe itself as shielding and leverag-

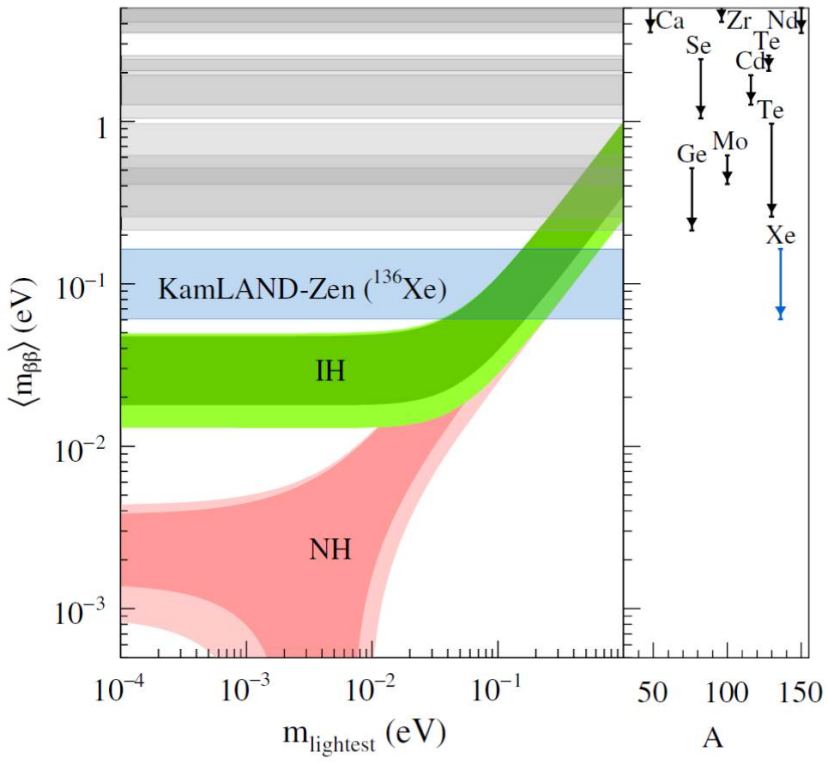


**Figure 1.5:** Plot of $\langle m_{\beta\beta} \rangle$ as a function of minimum neutrino mass ($m_{\text{lightest}}$). KZ has the strongest limit on $\langle m_{\beta\beta} \rangle$ regardless of isotope. Limits from other isotopes are shown in the right panel [12].

ing the position reconstruction capability of the TPC. Gamma rays at the Q-value only penetrate on average $\sim$9 cm into LXe [14]. This means $\gamma$-induced backgrounds will tend to occur near the edge of the detector more frequently, while $0\nu\beta\beta$ events will be uniformly distributed throughout the detector. This difference allows these backgrounds to be suppressed by taking event position as well as energy into account when analyzing detector data. Another way to reduce $\gamma$-induced backgrounds is to use materials that have low radioactivity. The EXO-200 detector was built from materials carefully selected for low radiation and that underwent thorough surface cleaning [14]. Passive shielding of external $\gamma$'s is achieved by the cryogenic fluid known as HFE surrounding the detector and by a lead shield outside of the cryostat. Muons originating from cosmic rays are shielded by the $1624^{+22}_{-21}$ meters water equivalent overburden at the WIPP underground facility where the detector is located. Active shielding is provided by a set of veto panels comprised of plastic scintillator and phototubes on both ends for light read out. These panels are used to reject

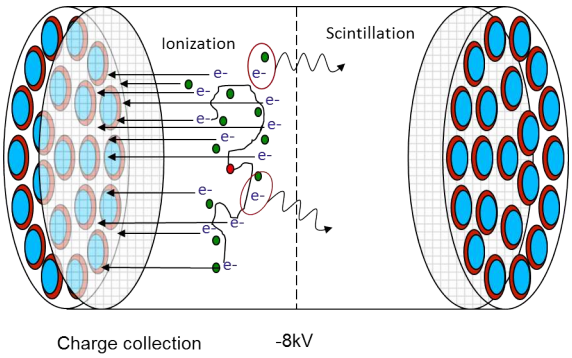


**Figure 1.6:** The EXO-200 detector schematically depicted. The endcaps of the cylindrical detector are instrumented for both light and charge readout.

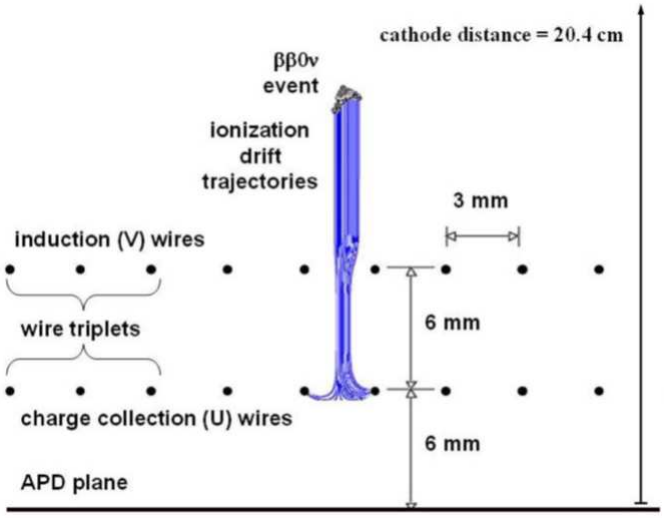


**Figure 1.7:** The anode schematically depicted. The anode planes are instrumented for both light and charge readout. The U and V-wires are shown collinear but they are in fact crossed at 60°. A simulation of electron drift is also shown [14].

96% of cosmic ray muons [14]. When a veto event occurs, 60 s of data is tagged as vetoed and is not included in the low background data.

A background which cannot be discriminated against easily is $2\nu\beta\beta$. Some of these decays will be at the upper edge of the $2\nu\beta\beta$ energy spectrum and thus be close to the energy of $0\nu\beta\beta$ decay. In order to distinguish between $2\nu\beta\beta$'s near the Q-value and actual $0\nu\beta\beta$ good energy resolution is required. Much effort has been made to maximize the resolution of the EXO-200 detector [15]. One key to good resolution is taking advantage of the anti-correlation between ionization energy and scintillation energy that has been observed in LXe [16]. The relative amounts

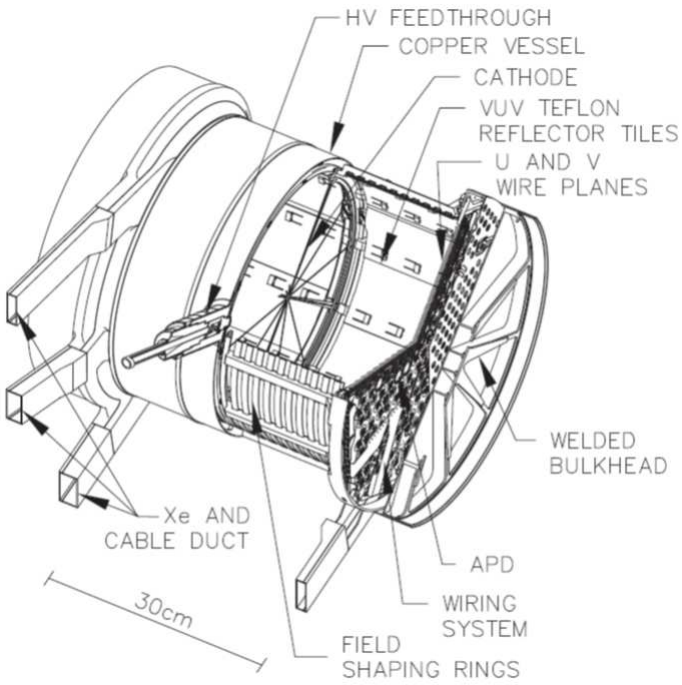


**Figure 1.8:** Cut away schematic of the TPC showing a number of components.

of ionization and scintillation energy depends on the amount of recombination. Recombination occurs when free electrons combine with xenon holes to form excited xenon dimers, which relax to produce scintillation photons. So for a particular event, greater scintillation is a result of more recombination, which means a decrease in the number of free electrons. Anti-correlation is thus a result of fluctuation of the recombination level between events with the same total energy. For the case of EXO-200 the anti-correlation is characterized by a rotation angle, $\theta^R$. This angle is measured using calibration $\gamma$ sources deployed at several positions near the TPC. Fig. 1.9 shows the relationship between the charge and light channels for $^{228}$Th calibration source events. The anti-correlation is measured from this data and the rotated energy spectrum is determined according to Eq. 1.10 where $E_R$ is the rotated energy of an event, $E_S$ is the light channel energy of the event and $E_I$ is the charge energy of the event. When taking advantage of the anti-correlation using this rotation angle scheme, the energy resolution defined as $\sigma/E$ improves to 1.2% from either 3% using ionization only or 5% using scintillation only [15].

$$E_R = E_S sin(\theta^R) + E_I cos(\theta^R) \tag{1.10}$$

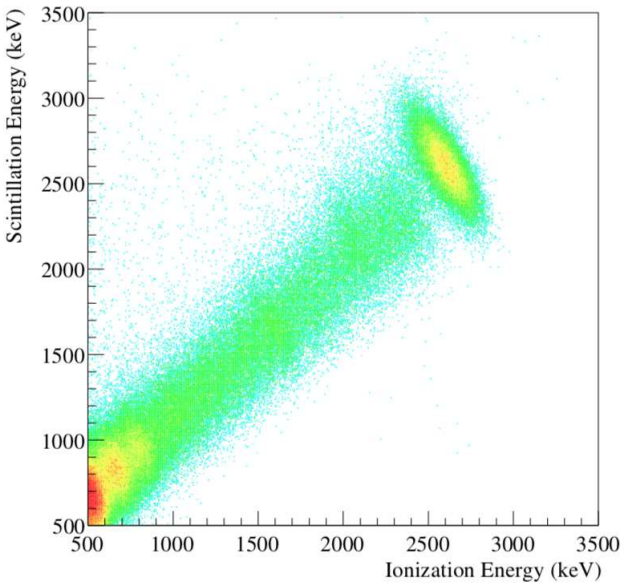


**Figure 1.9:** Anti-correlation between ionization and scintillation for single-site events from a $^{228}$Th source. The cluster of data points at top right is a sharp peak in the decay spectrum. The downward angle of the upper right cluster is measured to give the rotation angle $\theta^R$ [15].

The ratio between the scintillation and ionization energies of an event provides another way to reject certain backgrounds in the experiment. Alpha ($\alpha$) particles moving through LXe create tracks of relatively higher ionization density than $\beta$'s or $\gamma$'s. This higher density causes a greater rate of recombination and thus a higher light-to-charge ratio [17]. This can be used to eliminate $\alpha$ backgrounds by requiring the light-to-charge ratio to be below a certain threshold. Additionally, identification of $\alpha$'s was used in [17] to investigate neutralization of ions in the detector.

The EXO-200 experiment ran from 2011 to 2014 (Phase I) and again from 2016 to 2018 (Phase II). Phase I data has been used to measure the half-life of $2\nu\beta\beta$ to be $T_{1/2}^{2\nu\beta\beta} = 2.165 \pm 0.016(\text{stat}) \pm 0.059(\text{sys}) \times 10^{21}$yr [11]. Both phases have been used to set a limit on the $0\nu\beta\beta$ half-life of $T_{1/2}^{0\nu\beta\beta} > 1.8 \times 10^{25}$yr [15]. A plot of the best fit to the energy spectrum of single-site events is shown in Fig. 1.10. Many additional physics results have been generated using data from the

EXO-200 experiment including a search for triple-nucleon decay of nucleons in the xenon [18]. This search is discussed in detail in this work.

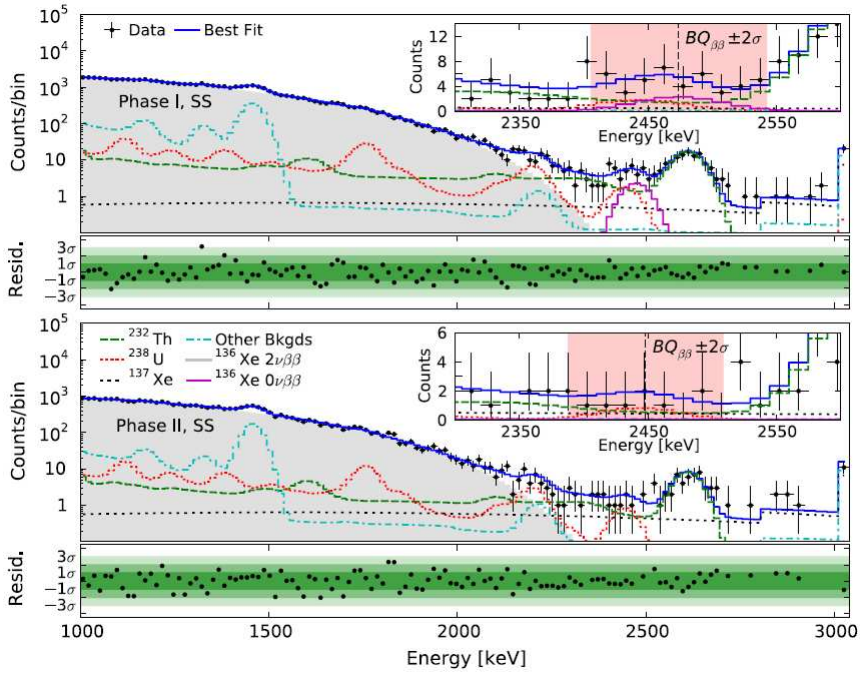


**Figure 1.10:** A fit to an energy spectrum for the most recent EXO-200 $0\nu\beta\beta$ search is shown. A boosted decision tree discriminator variable that reflects the positional sensitivity of the experiment is fit concurrently, and is not shown. [15]

## 1.4 Nucleon Decay

Current experimental data is consistent with baryon number (B) and lepton number (L) conservation. Long running proton decay searches have shown no evidence of B non-conservation [19, 20]. However, proton stability is not guaranteed by a fundamental symmetry. Discovering that baryon number is not conserved under all circumstances would have important implications regarding the understanding of the evolution of the Universe, in particular on the origin of the matter-antimatter asymmetry. As discussed earlier in this chapter, $0\nu\beta\beta$ would violate L conservation by two ($\Delta$L = 2). Since EXO-200 has been searching for this process in LXe, it is appropriate that B non-conservation in LXe be explored with EXO-200 data as well. In Ch. 2, the details of

a search for two $\Delta$B = 3 processes using EXO-200 data is discussed. These processes are triple nucleon decays of $^{136}$Xe to $^{133}$Sb and to $^{133}$Te.

In order to perform this search, a model of the signal in the EXO-200 data produced by triple nucleon decays needed to be generated. The search relies on signal from nuclear decays of the decay daughters, $^{133}$Sb and to $^{133}$Te. The detected energy distributions of these decays depends on whether they are neutral or ionized. Thus, a study of the likely charge state of the daughters was performed, and is discussed in Ch. 2. Once the probability that a daughter is ionized was discerned, it was used to weight Monte Carlo models of the signal decays in a manner discussed in Sec. 2.4.3. With the signal model generated, an analysis of the data was carried out as described in Sec. 2.5. The results of this search are then discussed in Sec. 2.6. There was found to be no significant evidence of triple nucleon decay to either $^{133}$Sb or $^{133}$Te in the EXO-200 data. Limits on the lifetimes of these decays were determined and published in [18]. At the time of publication, the limits set were the strongest yet established on triple-nucleon decays.

## 1.5 The nEXO Experiment

A proposed next generation experiment using the LXe TPC technology to search for $0\nu\beta\beta$ is known as nEXO. A schematic drawing of the nEXO TPC is shown in Fig. 1.11. It will incorporate 5000 kg of liquid xenon enriched in the $^{136}$Xe isotope. The nEXO detector will be a monolithic detector rather than a pair of TPCs as in the case of EXO-200. It will have charge tiles on one end of a cylinder, a cathode on the other, and silicon photo-multipliers on the walls. The increased size of the detector provides additional self-shielding of external $\gamma$-ray backgrounds. Much has been learned from measuring backgrounds of different components of the EXO-200 detector [21]. As a result, very detailed estimates of background rates for nEXO have been calculated [22]. The values shown in Fig. 1.12 are the number of SS background events per kilogram year within a FWHM/2 of the $Q_{\beta\beta}$. The projected sensitivity of nEXO is shown in Fig. 1.13. It shows that with the standard backgrounds nEXO can expect to achieve a sensitivity of $9.2\times10^{27}$yr. This is enough to exclude almost all of the inverted hierarchy region in Fig. 1.14.

In order to improve the sensitivity of future $0\nu\beta\beta$ searches, a method to eliminate all non-$2\nu\beta\beta$ backgrounds, known as barium tagging, is being investigated. If this is implemented perfectly, it would lead to a sensitivity as shown in Fig. 1.15.

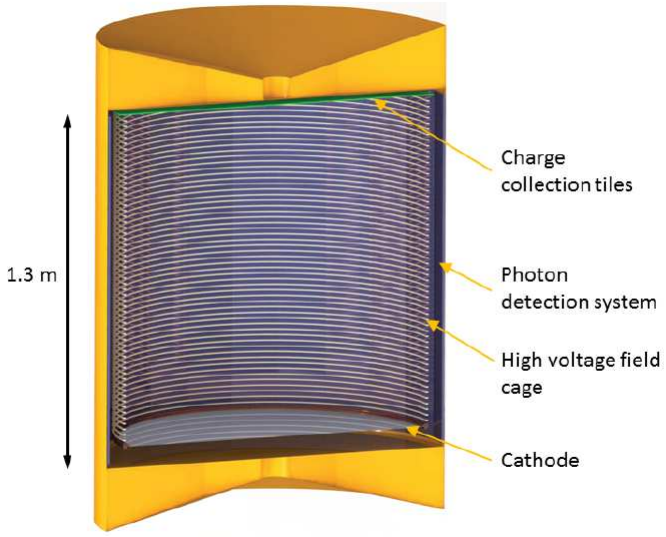


**Figure 1.11:** Sketch of the nEXO TPC with copper vessel, cathode, charge collection anode and photodetectors shown [22].

## 1.6 Barium Tagging

The method being pursued to eliminate non-$2\nu\beta\beta$ backgrounds in a $^{136}$Xe $0\nu\beta\beta$ experiment is barium tagging. When $^{136}$Xe undergoes $0\nu\beta\beta$ decay the daughter nucleus will be $^{136}$Ba. The nuclear decay formula is:

$$^{136}Xe \rightarrow ^{136} Ba^{++} + 2e^{-} \tag{1.11}$$

Currently $0\nu\beta\beta$ decay searches measure energy deposited in a detection by the two electrons. The ionization and scintillation detected in LXe arises from these two electrons. The idea behind barium tagging is to positively identify the barium daughter as well as to measure the energy of the electrons. This allows for rejection of any event that may have the proper energy but does not produce a barium daughter. Thus all non-$2\nu\beta\beta$ background events may be rejected when searching for $0\nu\beta\beta$ decay.

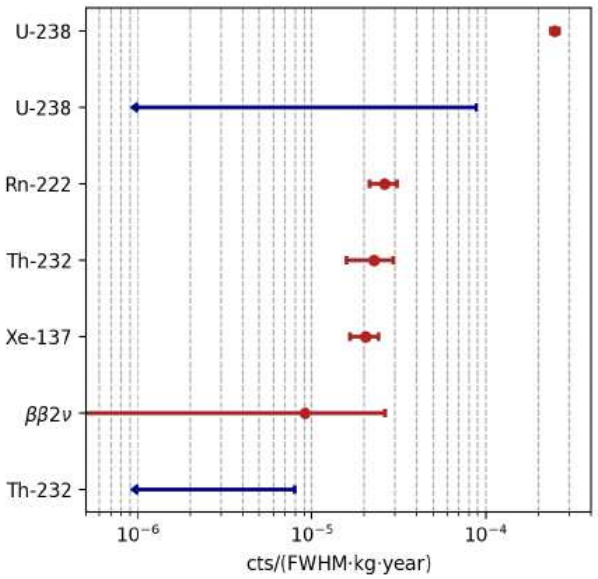


**Figure 1.12:** SS background contributions by source for nEXO for range within FWHM/2 of $Q_{\beta\beta}$. Blue arrows are 90% C.L. upper limits while the red circles are measured values with $1\sigma$ error bars [22].

There are several proposed tagging methods for the nEXO experiment [24–26]. In this work, barium tagging in solid xenon (SXe) will be discussed. This method involves dipping a cryoprobe into LXe to freeze and capture the daughter barium in a SXe matrix on the probe. Once this has been done, the probe can be removed from the LXe and the daughter barium can be detected using the imaging techniques discussed in [24, 27]. This technique involves shining laser light to excite fluorescence in the daughter barium and using the detected fluorescence to positively identify the daughter. A schematic of a possible probe concept is shown in 1.16.

Work done in [27] showed that single barium atoms in a SXe matrix can be detected by imaging barium fluorescence. This was done by depositing a SXe matrix by flowing gaseous xenon onto a window while simultaneously depositing into the growing SXe matrix $Ba^+$ ions with 2 keV of energy from a mass selected ion beam. Some ions are neutralized in the matrix and are excited by a focused laser beam at 570 nm wavelength after the matrix has been cooled to 10K. This excites fluorescence at several wavelengths that depend on the matrix site the atom occupies. Fluorescence from these sites tends to decay over time as the barium atom is repeatedly excited. This bleaching phenomenon occurs at different rates for the different matrix sites. Barium atoms in a single-

vacancy matrix site bleach at the slowest rate and emit 619 nm light. This was the emission used to image single barium in [27]. The signal is collected on a CCD camera resulting in an image of the laser spot and fluorescence. The number of ions deposited in the excitation spot can be calculated by integrating the ion beam current density over the deposition time and multiplying the result by the area of the excitation spot. The ion deposition time can be varied to change the number of ions in the excitation spot. In this way, it was demonstrated that the emission signal is linear with the number of ions deposited in the excitation region. This linearity is what is expected for fluorescence from Ba atoms. Fluorescence due to a barium dimer would scale quadratically with the number of ions deposited.

Single atom detection was done by scanning the excitation laser across a region sparsely populated with barium atoms. An image of the fluorescence is taken at each position. In this way, an image of a two dimensional region is built up. When the laser spot is positioned over an atom it will fluoresce. This procedure gave sharp peaks in signal as shown in Fig. 1.17. Additionally, the laser was left to sit on peaks identified in the scan. When this was done a very clear turn off of the fluorescence was seen. The time at which this turn off occurred was different for each different peak. This behavior is consistent with what is expected for a single barium atom that is being excited a variable number of times before ending in a dark state. Finally, it has been shown that once the SXe sample is melted and a new one is deposited, there is no effect of prior deposits on the signal level. In other words, the barium signal can be erased between samples [27]. This behavior is very advantageous for an eventual implementation in a xenon $0\nu\beta\beta$ detector.

Now that fluorescence imaging in SXe has been used to detect single barium atoms, demonstrating that barium ions can be captured out of LXe in a SXe matrix, extracted from the LXe, and imaged with similar selectivity is the next main step towards barium tagging. To this end, a Joule-Thompson (JT) cryoprobe has been tested in a copper cell that contains LXe. It has been attached to a bellows to allow extraction. This work will be discussed in more detail in chapters 3 and 4. The single Ba atom fluorescence imaging described above has been achieved at low temperatures using an ion beam source. Initial cryoprobe experiments test whether large numbers of $Ba^+$ can

be captured from LXe and detected in a SXe matrix at higher temperature. It will be of interest to measure how efficient this process is and at what rate ions captured out of LXe in this manner neutralize to Ba atoms.

Measurements were also carried out of the fluorescence lifetime of barium deposited in solid xenon using the ion beam. Particularly, large deposits of barium ions were deposited in the same manner as for the barium imaging experiments described above. The resultant barium atoms in SXe were excited with a pulsed laser, and their fluorescence was collected using a time-correlated single photon counting apparatus provided as demonstration equipment from PicoQuant Inc. The lifetime of a barium transition and the lifetime of the background fluorescence were both measured. This work is described in Sec. 3.8.

## Summary and Goals

This work is a description of efforts to achieve two primary goals. The first is to observe or constrain the lifetime of nucleon decay of $^{136}$Xe to $^{133}$Sb or $^{133}$Te. This tests the hypothesis that baryon number is conserved in our universe. This work describes a search for such decays using data from EXO-200.

The other impetus behind the research described here is the development of barium tagging. It is hoped that barium tagging will be used in future $0\nu\beta\beta$ experiments to reduce backgrounds. In particular, this work focuses on development of a system to test dipping a cold probe into LXe to extract barium ions or atoms in a SXe sample and then to observe them. This work is done in association with the nEXO experiment.

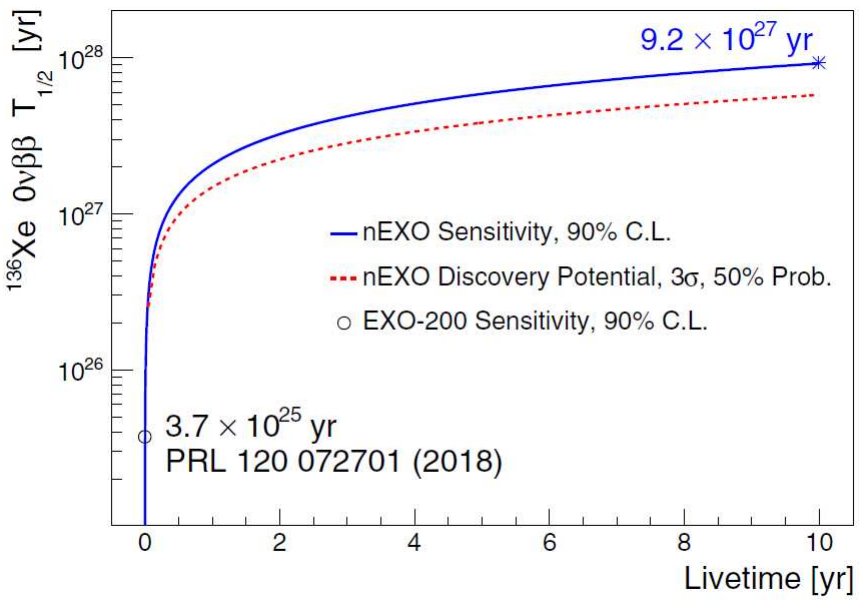


**Figure 1.13:** $0\nu\beta\beta$ half-life sensitivity at 90% C.L. and $3\sigma$ discovery potential versus livetime simulated for the nEXO experiment assuming standard backgrounds from Fig. 1.12 [23].

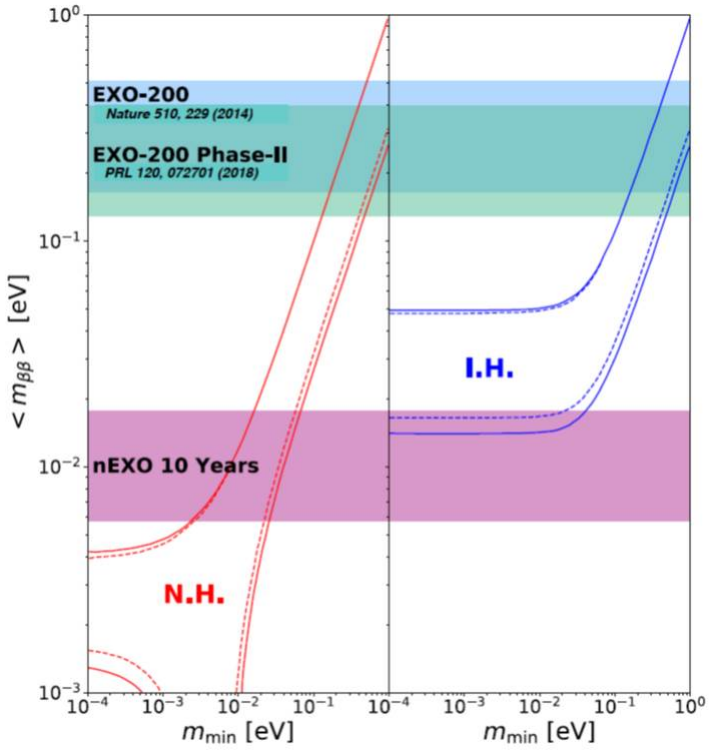


**Figure 1.14:** Projected exclusion sensitivity of neutrino mass phase space. The nEXO experiment projects to exclude the normal hierarchy in ten years of running.

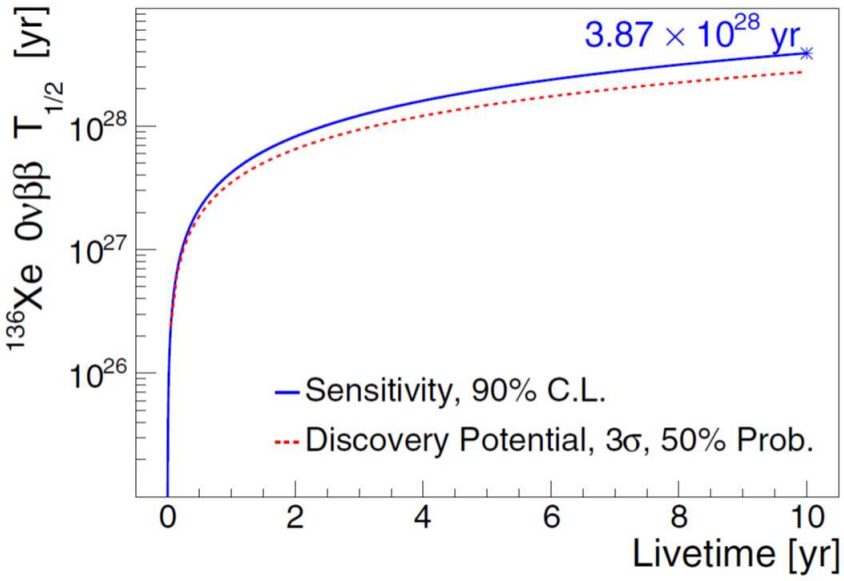


**Figure 1.15:** Sensitivity and discovery potential for nEXO for the case in which all non-$2\nu\beta\beta$ are eliminated [23].

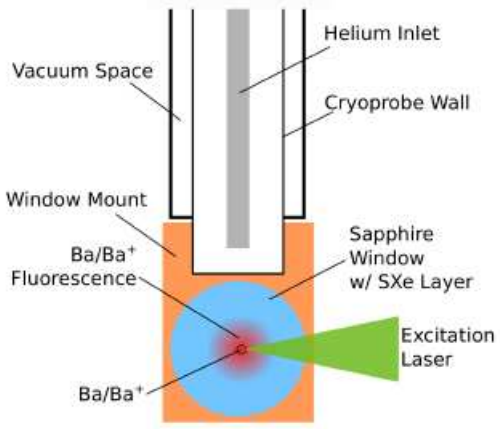


**Figure 1.16:** Concept for tagging barium on a cryoprobe after capturing in SXe. Barium is frozen in a SXe matrix on a sapphire window at the end of the cold probe. Laser light induces fluorescence that is collected and used for identification of barium. [28].

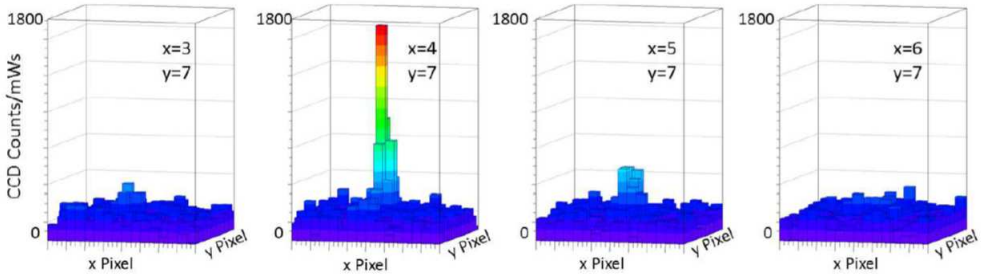


**Figure 1.17:** Images of different excitation spot positions during a scan. When the laser passes over an atom fluorescence signal stands out clearly above the background. Signal dies as the spot moves off the atom.

# Chapter 2

# Nucleon Decay

Using the phase I low-background dataset from EXO-200, a search was performed for decays of $^{133}$Sb and $^{133}$Te resulting from triple nucleon decay in $^{136}$Xe. The details of this nucleon decay (ND) search will be discussed in this chapter along with further details regarding the EXO-200 detector as they pertain to this search.

## 2.1 Search Motivation

The Standard Model (SM) successfully explains most experimental data at energies below a few hundred GeV, yet it is generally regarded as an effective field theory valid only up to some cut-off scale $\Lambda$. In many extensions of the SM, baryon and lepton numbers are no longer conserved.

An example of a process violating only lepton number conservation (by two units) is neutrinoless double-beta decay ($0\nu\beta\beta$), which may occur in several even-even nuclei, but has not been observed yet. Violation of total lepton number by two units could be related to the dimension 5 operator, the so-called Weinberg operator, $\frac{llHH}{\Lambda_L}$ (where $l$ is the left-handed lepton doublet, $H$ is the Higgs doublet, and $\Lambda_L$ is the cut-off scale associated with lepton number violation). This is the lowest dimension operator that can produce neutrinoless double-beta decay. The EXO-200 experiment has searched for the signatures of this process in $^{136}$Xe for the two most commonly considered mechanisms - decays with the emission of two electrons only [29] and decays with the additional emission of one or two massive bosons, called Majorons [30]. With the "natural" assignments of parameters, the current limits on the $0\nu\beta\beta$ decay rate [12, 29, 31] test $\Lambda_L$ up to scales of $10^{14}$ to $10^{15}$ GeV. Analogously, the dimension 6 operator $\frac{QQQl}{\Lambda_B^2}$ (where $Q$ is quark doublet and $\Lambda_B$ is the cut-off scale associated with baryon number violation) would cause both B and L violation. The current limits [19, 20, 32] on protons decaying into $\pi^0 e^+$ and $K^+\bar{\nu}$ provide limits on $\Lambda_B$ in the range of $10^{15}$ to $10^{16}$ GeV, similar to the ones obtained for $\Lambda_L$.

## 2.2 Search Strategy

For nuclei with mass number A $\gg$ 3 four triple nucleon combinations (ppp, npp, nnp, or nnn) could undergo the $\Delta$B = 3 decay. As a result of this decay, nuclei with A-3 nucleons will remain, unless additional baryons are emitted by an excited daughter nucleus. Energy deposits from $\beta$ and $\gamma$ particles emitted by the ND daughter nuclei and subsequent daughters are the experimental signature of ND in this work. A diagram of the decay chains of $^{133}$Sb and $^{133}$Te is shown in Fig. 2.1. Each of the $\beta$ decays shown there will create, with some efficiency, an observable event. Observing these chains is the strategy already used in the DAMA experiment to search for ND in $^{136}$Xe. This search yielded lifetime limits on ppp and npp of $3.6\times10^{22}$ yr and $2.7\times10^{22}$ yr respectively [33]. A similar strategy has also been used to search for $\Delta$B =1 and $\Delta$B = 2 decays in $^{12}$C, $^{13}$C, $^{16}$O, and $^{136}$Xe [34, 35]. The focus of this work is a search for the decays of daughter nuclei $^{133}$Sb and $^{133}$Te, which may result from ppp and npp nucleon decays. The Q-values and lifetimes are given in table 2.1 for the $\beta$ decays shown in Fig. 2.1. These are the decays used to

**Table 2.1:** Q-values and half-lives of the daughters of NDs [36].

| Daughter Isotope | Q-Value [keV] | Halflife |
|---|---|---|
| $^{133}$Sb | 4010 | 2.51 min |
| $^{133}$Te | 2955 | 12.5 min |
| $^{133m}$Te | 3289 | 55.4 min |
| $^{133}$I | 1757 | 20.8 h |
| $^{133}$Xe | 427.4 | 5.25 d |

search for ND in $^{136}$Xe. Nucleon decay to $^{133}$I could also produce signal in the EXO-200 detector. However, this decay path is not studied because it produces fewer daughter decays in the xenon. The final decay, of $^{133}$Xe, is below the analysis energy threshold of 980 keV and is therefore not detectable in this experiment.

Nucleon decays in general are very energetic. Thus it is possible that daughter nuclei will be in a sufficiently excited state to emit further nucleons. For example, pp decay could result in a $^{133}$Te.

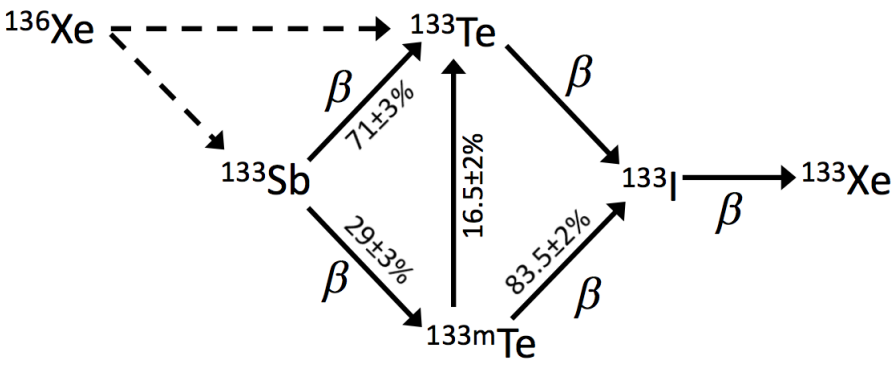


**Figure 2.1:** Decay chains for daughter nuclei resulting from nucleon decay of $^{136}$Xe. The branching ratios are from [36]. Decay of $^{136}$Xe may result in $^{133}$Sb or $^{133}$Te. These daughters will undergo subsequent beta decays that are detectable in the EXO-200 detector.

So it is not possible to directly associate a specific daughter with a given decay mode. The partial lifetime for all nucleon decays to daughter $i$ = ($^{133}$Sb or $^{133}$Te) is:

$$\tau_i = \frac{N_{nucl} T \epsilon}{S_i}, \tag{2.1}$$

where $S_i$ is the number of the observed daughter nuclei of type $i$, $T$ is the experiment livetime, $N_{\rm nucl}$ is the number of initial parent nuclei, and $\epsilon$ is the detection efficiency. The lifetime $t_j$ for a particular nucleon decay mode $j$ (e.g. ppp or npp) is given by:

$$\frac{1}{t_j} = Br_j \sum_i \frac{1}{\tau_i} \tag{2.2}$$

where $Br_j$ is the total branching ratio of nucleon decay via mode $j$.

In addition to $^{136}$Xe, EXO-200 contains a non-negligible amount of $^{134}$Xe($\sim$19% [14]), which can also be utilized to search for nucleon decays using the same strategy. However, given the $\sim$4 times smaller exposure and lower Q-Values of the corresponding daughter isotopes, the resulting lifetime limits are not expected to be competitive with the ones obtained using $^{136}$Xe analysis. Hence this work focuses solely on the $^{136}$Xe analysis.

## 2.3 Detector and Data Processing

The EXO-200 TPC is discussed in Sec. 1.3. As described, the TPC technology allows the position of an event to be reconstructed. Position reconstruction can be used to reduce backgrounds since background events caused by $\gamma$ rays originating from outside the detector occur at higher rates near the edges of the detector. For this reason, a fiducial volume (FV) is chosen to exclude as many background events as possible without excluding signal events. If an event's position is reconstructed outside of this volume, it is likely a background event and is removed from the dataset. The FV is defined, in the case of [15], as a hexagonal prism within each TPC with an apothem of 162 mm. It extends in the z dimension with $10 < |z| < 182$ mm. The cathode is defined as $z = 0$ mm. The anodes are located at approximately $z = \pm 206$ mm. Each nucleus in the $^{133}$Sb or $^{133}$Te decay chains can emit $\gamma$ rays that can produce energy deposits some distance from the original nucleus via Compton scattering. As a result, it is possible for ND daughters anywhere in the detector to produce signal events in the FV. It is particularly likely, for reasons that will be discussed in Sec. 2.4.3, that a ND daughter will cause $\gamma$ events originating from the cathode that make it into the FV before scattering. For this reason, the FV was expanded in the direction of the cathode by 9 mm. Thus the FV for this analysis included events with z-dimension within $1 < |z| < 182$ mm. The total $^{136}$Xe mass in the active and inactive volumes is 136.5 kg, or $6.05 \times 10^{26}$ atoms of $^{136}$Xe.

When an event occurs, the signal is recorded as a waveform in one or more detector channels. There are a total of 226 channels, which include 76 U-wire channels, 76 V-wire channels, 74 APD channels, a muon veto channel, and a high-voltage glitch detector channel. Waveforms from each channel are passed through front-end electronics where they are shaped and converted to a digital signal. At this point the data is passed to a trigger module that synchronizes data from all channels and determines whether the data acquisition will be triggered. If a trigger condition is met, data is written from the trigger module to a control computer and subsequently a hard-disk [11].

There are four types of TPC triggers [11]: a U-Wire trigger for events in the LXe over $\sim$100 keV, an individual APD event above $\sim$3-4 keV, a summed APD event over 25,000 photons, and a so-

licited trigger occurring every 10 seconds. The U-wire trigger is designed to be triggered by $\gamma$ and $\beta$ events in the LXe. The single APD trigger is intended to capture radioactivity inside of the APDs. The summed APD trigger selects for $\alpha$ events in the LXe. One purpose of the solicited trigger is to measure the livetime of the detector. This is done by simply counting the number of solicited triggers that occurred during physics runs and met all other timing criteria to be part of the dataset [11]. The number of solicited triggers is then divided by their frequency (.1 Hz) to give the livetime in seconds. A total of $596.70$ live days of data were accumulated for this dataset, resulting in an exposure of 223 kg·yr.

Once the data has been recorded, it goes through several processing steps [11]. First it is "rootified" when it is changed from binary data files to ROOT files [37]. Next is the reconstruction phase, during which signals are found, quantified, and checked against muon and noise events. Third is the processing phase, when signals are clustered and data corrections are applied.

ROOT is an object oriented data analysis framework commonly used in the field of particle physics. It allows data to be stored such that it can be efficiently analyzed, manipulated, and visualized. Most of the ND analysis was done using ROOT files and functions called via the PyROOT library within the Python programming language [38]. ROOT embeds the MINUIT minimization software [39], which is used to do the fitting necessary for the ND analysis.

The reconstruction of the signal starts with a signal-finding step. This is done by convolving the digitized waveform with a matched filter. If the result of this convolution exceeds a threshold level above the baseline of the waveform, then a signal is identified. A second algorithm is used to find additional signals within the same waveform, since the matched filter is only useful in identifying single pulses. Once all the signals are found in the waveforms, a waveform model is fit to the signal giving an amplitude and a time for each waveform. At this point the signals are corrected for channel gain, which varies between the hardware channels and is calibrated for the wires using a charge injection circuit and for the APD channels using an external laser pulser. The final stage of reconstruction is the clustering process that groups signals from different channels into clusters in space and time [11].

Some other corrections described below are applied to the waveforms. Electro-negative impurities in the LXe can capture electrons as they travel to the anodes. This will attenuate the charge signals in z-dependent manner. This is corrected for by measuring the electron lifetime $\tau_e$ periodically and applying a factor of $\exp(t/\tau_e)$ to the all ionization signals. Another small correction ($<<1\%$) is applied to the U-wire amplitudes to account for small induction signals caused by imperfect shielding provided by the V-wires. Finally a light map, which is created using $^{228}$Th calibration data, is used to correct the APD signal amplitudes in a position dependent manner. This light map has an average correction factor of 1 and has a range of $\sim$.5 [11].

Once an event has been reconstructed, it must pass a series of cuts before it is finally added to the low-background dataset used in this analysis. It must not be coincident with a solicited trigger or a noise event. It must not occur within 1 s of another TPC event or 120 $\mu$s of the end of the waveform trace. It must not contain more than one reconstructed scintillation signal. It must be fully 3D-reconstructed; i.e. not missing a U, V, or z-dimension [11]. It must be reconstructed within the fiducial volume. The scintillation energy to ionization energy ratio must be within limits. This cut removes events associated with $\alpha$ decays in the LXe since this ratio tends to be very high for these events. Finally, the total energy must be greater than 980 keV.

The low background dataset used for this analysis consists of events that pass all of these cuts. It is binned in energy with a bin width of 14 keV and divided between SS and MS events. The energy spectrum extends to 9800 keV, though the vast majority of events relevant to this analysis are below 4000 keV. The dataset is composed of data from all of EXO-200's run 2. This run was taken before two events at WIPP in 2014 caused the detector to be out of operation for two years.

Calibration of the detector using $\gamma$ sources was performed throughout this data collection period. As discussed in Sec. 1.3, an important use of the calibration data is to establish the rotation angle $\theta_R$. It is also used to refine the simulated PDFs in a continuous effort within the collaboration and to generate the light map used to correct the scintillation energy of each event. Finally, it was used as a bench mark to determine systematic uncertainties in this analysis. This process is discussed more in Sec. 2.5.2. The calibration is performed by moving one of several sources from

a shielded position away from the detector to a position near the detector. The different sources used to estimate errors in Sec. 2.5.2 are $^{228}$Th, $^{60}$Co, and $^{226}$Ra. The rotation angle is calculated based on almost daily $^{228}$Th calibration runs lasting about an hour each. The standard procedure was to accumulate 100,000 events per calibration run. The position of the source for these runs was directly outside the TPC near z = 0 (cathode position) inside of a copper source guide tube. This position is called source position S5. There were a number of calibration campaigns during which the different sources were placed at this position and at other positions around the detector.

## 2.4 Signal and Background Modeling

This analysis relies on fitting a model to the dataset selected by the procedure described above. This model consists of probability distribution functions (PDFs). Each PDF describes the probability that a specific decay will result in an event at a given energy in the detector. They have been created for both background decays and for signal decays. A high level discussion of the modeling of these decays is included below. The signal decays are those associated with the $^{133}$Sb and $^{133}$Te ND daughter nuclei. A calculation of the spatial distribution of these decays and a derivation of neutral fractions required for it is discussed below. It was also necessary to simulate the signal decays in a slightly different way so that the decay chains are split into components rather than simulated all together. The spatial distribution and the simulated decays were then combined to generate the signal model. This process is outlined in more detail below.

### 2.4.1 Daughter Ion Fractions

One of the parameters necessary to generate the spatial distribution of the decays is the daughter ion fraction for each decay shown in Fig. 2.1, including the initial nucleon decay. If the daughter of a decay is ionized it will drift toward the cathode before it decays again. This needs to be accounted for to get the proper signal PDF. For this reason, daughter ion fractions were estimated in the manner described below.

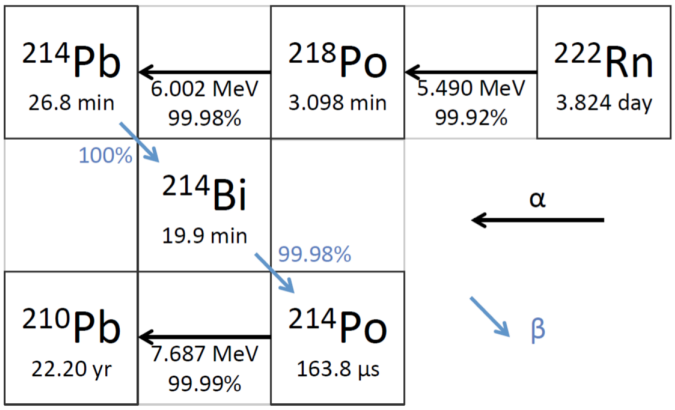


**Figure 2.2:** The decay chain of $^{222}$Rn that is present in the TPC.

Daughter ion fractions for radioactive decays in LXe were measured for the first time recently in EXO-200 [17]. The existence of $^{222}$Rn in the LXe produces a chain of radioactive decays shown in Fig. 2.2. It is possible to tag this chain using the time coincidence between the $^{222}$Rn and the $^{218}$Po decays. This allowed an analysis of the charge state of the $^{218}$Po atoms by checking if they drift towards the cathode between the decays. Using this method a velocity histogram of the $^{218}$Po daughters was produced as shown in Fig. 2.3. The high velocity peak shaded blue was integrated to give the fraction of $^{218}$Po that were ionized. The resulting ion fraction is $f_\alpha = 50.3 \pm 3.0\%$ [17]. Also discussed in [17], the ion fraction associated with $\beta$ decay was measured at 76.4% by comparing relative rates of $^{218}$Po and $^{214}$Po $\alpha$ decays in the bulk. The rate of $^{214}$Po decays in the bulk is influenced by the number of $^{214}$Bi that are ionized after $\beta$ decay from $^{214}$Pb and swept toward the cathode. As the daughter ion fractions for triple-nucleon decay to $^{133}$Sb or $^{133}$Te are not known, the above measurements have been used in a simple model as a guideline for an estimate.

A dominant process determining the final daughter ion fraction is recombination of the daughter ion with the local electron density in the electron cloud from the decay. The rate of this process competes with the rate at which the electron cloud is drawn away from the daughter ion by the electric field. Charge transfer collisions with positively charged holes that re-ionize neutralized atoms may also occur in the $\sim 10^5$ longer time frame during which the cloud of holes is drawn away. At the electric field of the detector, the local ionization density at the daughter location should be the critical parameter that determines the final daughter ion fraction.

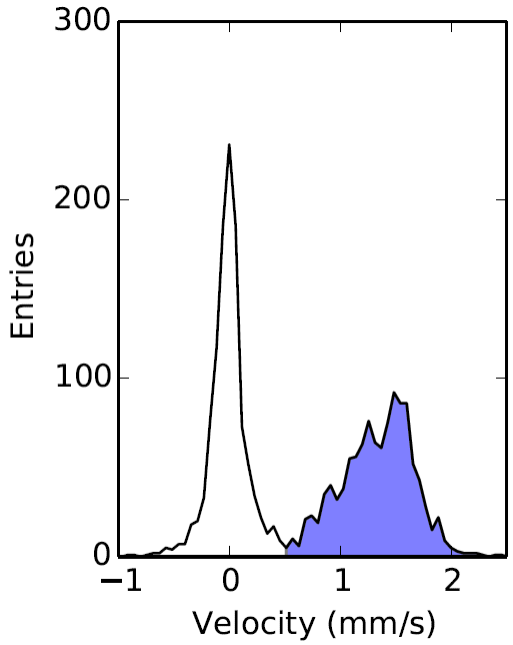


**Figure 2.3:** Velocity histogram of $^{218}$Po. The shaded region represents ions and the zero velocity peak is atomic $^{218}$Po [17].

In $\beta$ decay, there is negligible daughter recoil energy, and the electron cloud is of large radius and low density. In contrast, in $^{222}$Rn $\alpha$ decay, the $^{218}$Po daughter recoils with 101 keV of energy [17]. The local electron cloud due to ionization both from the $\alpha$ particle and the nuclear recoil is of much smaller radius and much higher density at the final stopping place of the daughter. The greater recombination that follows between daughter ions and the higher electron density qualitatively explains the smaller observed daughter ion fraction in $\alpha$ decay compared to $\beta$ decay.

For ppp and npp decay the dominant processes are [40]:

$$\begin{aligned} ppp &\rightarrow e^+ + \pi^+ + \pi^+ \\ npp &\rightarrow e^+ + \pi^+ \end{aligned} \tag{2.3}$$

The highly energetic charged particles emitted, $e^+$ and $\pi^+$, leave low ionization density tracks near the daughter location. The recoil energy of the daughter is large, e.g. 15 MeV average for $^{133}$Sb from ppp decay in reaction 2.3. SRIM simulations of the 3-D ionization density in the neighborhood of the daughter ion from $^{136}$Xe ppp and npp decay indicate a similar shape and

density to the electron cloud from $^{222}$Rn $\alpha$ decay [41]. The results of this simulation are shown in Fig. 2.4. Thus, a similar daughter ion fraction is expected for ppp and npp decay as for $^{222}$Rn $\alpha$ decays, i.e., $\sim$ 50%.

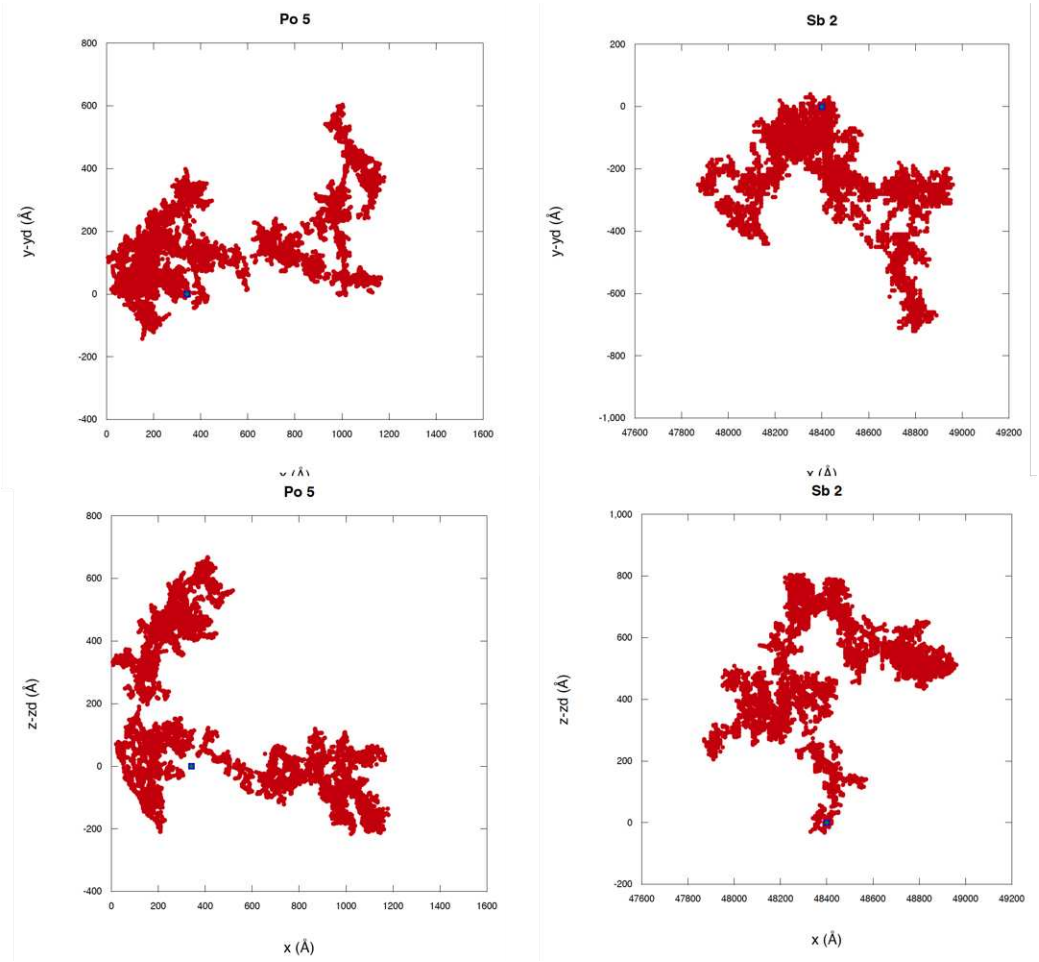


**Figure 2.4:** The right plots are collision locations for a $^{133}$Sb recoiling from reaction 2.3 in LXe. The left plots are collisions on a $^{218}$Po nucleus that recoils from an $\alpha$-decay with 101 keV of energy. It can be seen that the two particles have qualitatively similar tracks.

To confirm this more quantitatively, a simple model of charge drift in the detector field with varying recombination and charge transfer rate coefficients was applied to the initial electron and hole distributions simulated for individual ppp daughter recoil events and $^{222}$Rn $\alpha$ decay events. For a given recombination rate coefficient, the charge transfer rate coefficient was adjusted to yield a 50.3% daughter ion fraction on the average in $\alpha$ decay events as measured in EXO-200. With

the same pair of parameters, the average daughter ion fraction for ppp events was within 4.3% of 50% for a wide range of physically reasonable assumed recombination rates. Conservatively doubling this range to $\pm$9% for model uncertainty and adding the 3% experimental uncertainty in quadrature, a daughter ion fraction of 50$\pm$10% was used in this analysis for the ppp and npp decay. The observed daughter ion fraction of 76$\pm$6% for $^{214}$Pb $\beta$ decay was used for the subsequent $\beta$ decays. Extreme values of these two daughter ion fractions are used to generate the detection probability uncertainties described in Sec. 2.4.3, that are used in this analysis.

### 2.4.2 Monte Carlo Simulations

The PDFs are generated via a Monte Carlo (MC) simulation, which happens in two stages. First, the simulation package GEANT4 [42] uses a detailed parameterization of the detector materials and geometry to generate energy deposits within the detector. The output of this stage is fed to the second stage, which generates signals on hardware channels. These simulated signals go through the same processing steps as actual hardware signals, resulting in a simulated energy spectrum of events associated with a specific decay. For example, the decay of $^{60}$Co was simulated 173,912,023 times at various locations within the copper LXe vessel. This resulted in 7,658,649 SS events that passed all analysis cuts and are distributed in energy as indicated by the PDF shown in Fig. 2.5. The ratio of the number of events passing all cuts to the number of simulated decays is called the efficiency of the PDF. The spectral shape and efficiency of each PDF is unique to the species decaying and the detector component from which the decays originate. A number of decays are simulated in various components of the detector including backgrounds like $^{60}$Co in the vessel, standard signals like $2\nu\beta\beta$ in the LXe, and the $^{133}$Sb and $^{133}$Te decays chains that are the signal PDFs in this analysis. These background and signal models are combined to create an overall model, which is parameterized and fit to the data. This process is described in more detail in Sec. 2.5.1.

Typically, the PDFs are generated in complete chains in GEANT4. This means decay daughters can themselves decay and contribute to the final PDF. This is a problem for this analysis for the

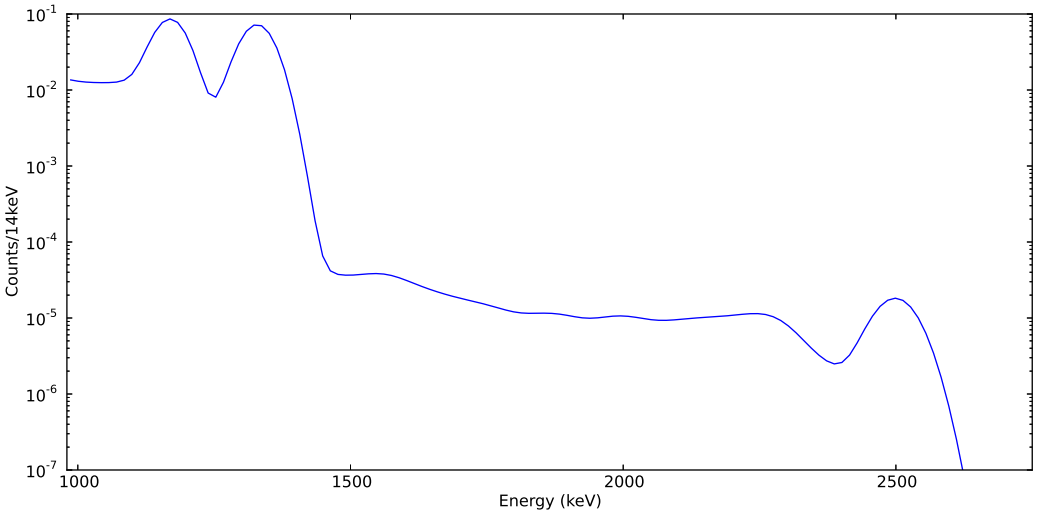


**Figure 2.5:** SS PDF of $^{60}$Co in copper vessel generated by MC simulation serves as an example of a background PDF used in the analysis.

reasons of daughter drift discussed in Sec. 2.4.3. This feature can be explicitly turned off. Thus PDFs were generated not of the entire $^{133}$Sb decay chain, which would include decays of $^{133}$Te and $^{133}$I. Rather, individual PDFs for each nucleus in the chain are simulated. The signal PDFs are simulated in three different detector regions: active LXe, inactive LXe, and cathode. The active LXe is that between the two anodes and inside the field shaping rings. The inactive LXe is all the xenon outside of the active volume. The cathode PDF is associated with decays occuring on the cathode. There are a total of 12 signal PDFs generated. They are shown in figures 2.6, 2.7, and 2.8.

### 2.4.3 Decay Distribution

As mention above, if the daughters of the initial nucleon decay are ionized, they will drift toward the cathode. This means that some of the daughter decays will occur in locations other than where nucleon decay occurred. In particular, decay daughters in the active liquid xenon may drift to the cathode before they decay further. Decays on the cathode have a different spectrum from those in the active. So it becomes necessary to know how likely a decay is to occur in the active as opposed to on the cathode in order to properly model the energy spectrum of the daughter decays.

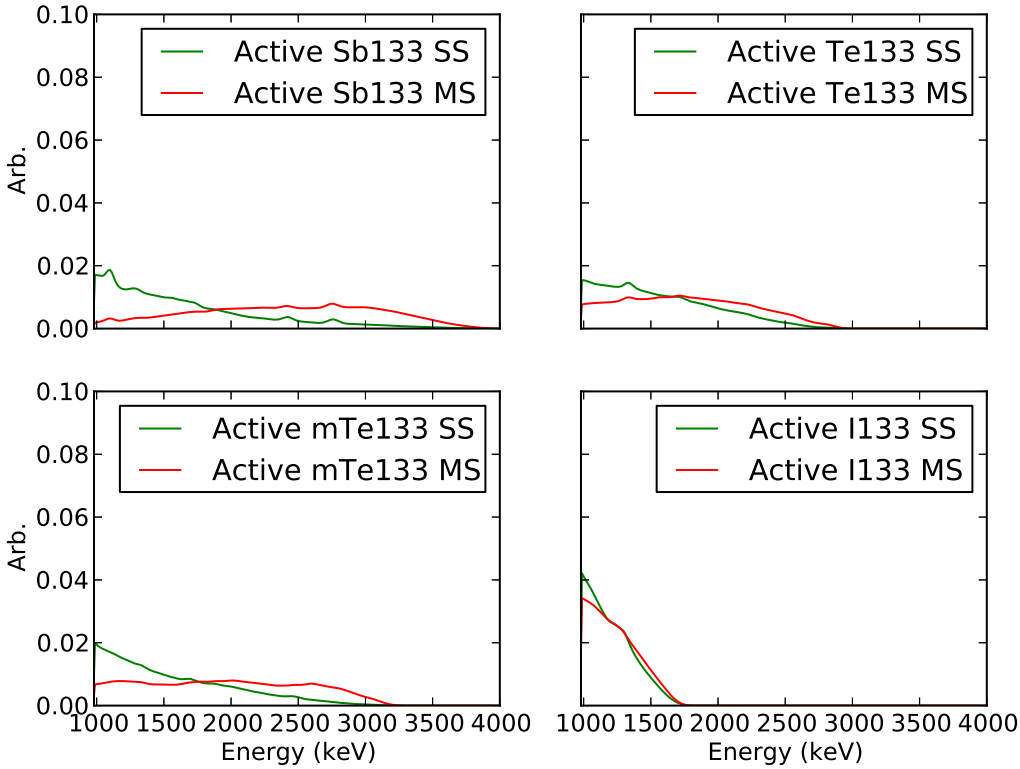


**Figure 2.6:** Both SS and MS PDFs of signal components in the active volume. They are each normalized such that their integral is one. Decays in the active volume are more likely to be $\beta$'s resulting in a broad energy spectrum.

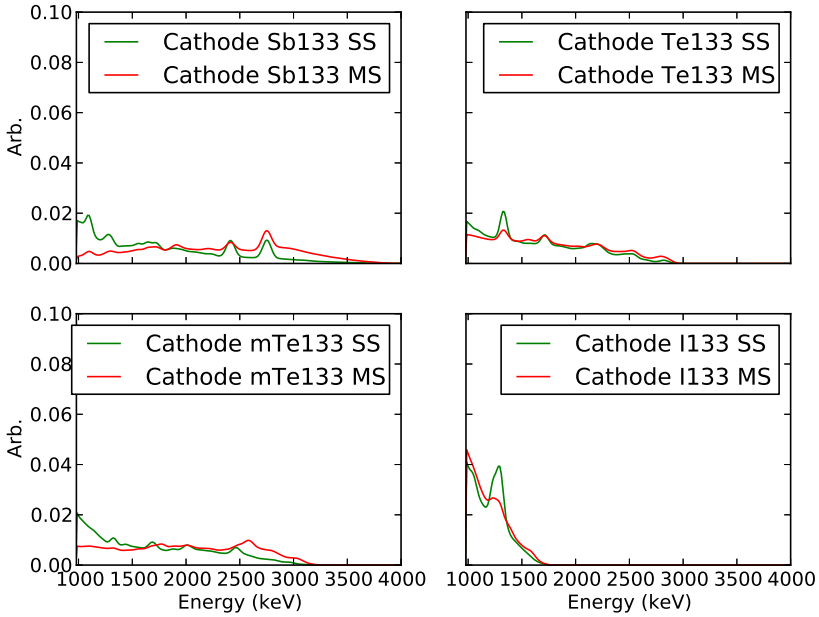


**Figure 2.7:** SS and MS PDFs of signal components simulated on the cathode normalized to unity. The spectral difference from the active PDFs arises from the fact that events originating on the cathode are more likely to be due to $\gamma$'s, which cause more sharp peaks in the spectrum.

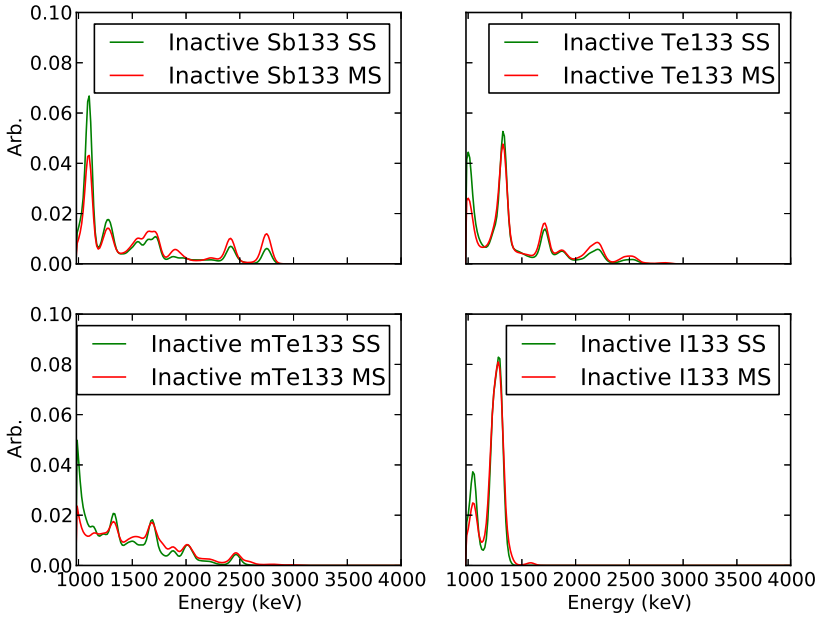


**Figure 2.8:** SS and MS PDFs of signal components simulated in the inactive LXe normalized to unity. Events originating in the inactive LXe are more likely to be the result of $\gamma$'s and also to be on average higher in energy than those simulated elsewhere due to attenuation of lower energy components.

To illustrate this an in depth calculation of the decay distribution of each daughter in the $^{133}$Sb chain is given here.

Necessary inputs to the model are the drift velocity, the decay lifetimes, and the ion fractions of the nucleon decay daughters and their subsequent decays. An average ion drift velocity (v) of roughly 1 mm/s was derived from [17].The distribution of daughter ions in different regions of the detector also depends on the decay chain in question, because it depends on the half-lives and the ion fractions of each daughter in the decay chain. As discussed in Sec. 2.4.1, the neutral fraction of the nucleon decays is determined to be $\alpha = 0.5$. The $\beta$ decay lifetimes are listed in 2.1. The initial nucleus, $^{133}$Sb, decay has a 29% branching fraction to metastable $^{133}$Te. The remainder of $^{133}$Sb decays are to the $^{133}$Te ground state. Nucleon decays may look very much like energetic muons moving through the detector. Thus it is assumed that every ND will cause a muon veto event by either triggering the veto panels or depositing large amounts of energy in the detector. Due to the veto cut, daughter decay events occurring $<$1 min after each nucleon decay will be cut. With all these inputs, the calculation of the spatial distribution can be carried out. The probability of a $^{133}$Sb decay occurring at a position z within the detector at time t can be written:

$$P(z,t) = \Theta(t-t_d)[\frac{\alpha}{d}\Theta(z)\Theta(d-z) + \frac{1-\alpha}{d}\Theta(d-z-vt)\Theta(z+vt)]\frac{1}{\tau}e^{-t/\tau} \tag{2.4}$$

The first term in brackets represents the neutral daughters, the second term in brackets represents the ionized daughters; the theta function in front of the brackets encodes the veto dead time, and the exponential at the end describes the time dependence of the $\beta$ decays. This is a uniform distribution in z confined to the active volume and an exponential distribution in time where $t_d = 1$ min is the veto dead time, $d = 204.41$ mm is the distance between the anode and cathode, and $\tau = 217.27$ s is the lifetime of $^{133}$Sb beta decay. Integrating over time gives:

$$
\begin{aligned}
P(z) = & \int_0^\infty \Theta(t - t_d) \times \\
& [\frac{\alpha}{d}\Theta(z)\Theta(d-z) + \frac{1-\alpha}{d}\Theta(d-z-vt)\Theta(z+vt)] \times \\
& \frac{1}{\tau}e^{-t/\tau}dt \\
= & \frac{\alpha}{d}\Theta(z)\Theta(z-d)e^{-t_d/\tau} + \frac{1-\alpha}{d}\Theta(d-z-vt_d)[\Theta(z+vt_d)e^{-t_d/\tau} - e^{-\frac{d-z}{v\tau}}] \\
= & N(z) + I(z)
\end{aligned}
\tag{2.5}
$$

where $N(z) = \frac{\alpha}{d}\Theta(z)\Theta(z-d)e^{-t_d/\tau}$ is uniform the distribution of neutral $^{133}$Sb decays in z and the distribution of $^{133}$Sb ions is given by $I(z) = \frac{1-\alpha}{d}\Theta(d-z-vt_d)[\Theta(z+vt_d)e^{-t_d/\tau} - e^{-\frac{d-z}{v\tau}}]$.

Integrating these over z gives probabilities for $^{133}$Sb neutrals and ions to decay in the active LXe. These probabilities are .3793 and 0.0722 respectively. So the total probability for an $^{133}$Sb decay to occur in the active volume after veto dead time is 0.452. The integration $\int_0^{t_d} \frac{1}{\tau}e^{-t/\tau}dt = 0.241$ is the probability that a decay will be missed due to veto dead time. This means that the probability of an $^{133}$Sb decay occurring on the cathode after 1 min is $1 - 0.241 - 0.452 = 0.307$.

To calculate the decay probabilities for $^{133}$Te in the $^{133}$Sb decay chain it is necessary to start with the initial distribution in z of $^{133}$Te nuclei. This is given by the time integral of the distribution in Eq. 2.5 ignoring the dead time constraint $\Theta(t - t_d)$. This results in an initial z distribution for $^{133}$Te nuclei of $P_i(z) = \frac{1}{d}[\alpha + (1-\alpha)(1 - e^{-\frac{d-z}{v\tau}})]$. To simplify the calculation, the conservative assumption is made that $^{133}$Te decays occurring before the dead time cutoff all occur in the active volume. This is conservative, since active volume decays contribute most efficiently to the signal. The probability that a given $^{133}$Te decay occurs before the 1 min dead time is over is $\int_0^{t_d} dt_1 \int_0^{t_d - t_1} dt_2 \frac{1}{\tau}e^{-t_1/\tau}\frac{1}{\tau'}e^{-t_2/\tau'} = 0.0068$, where $\tau'$ is the lifetime of $^{133}$Te decay. It is even smaller for $^{133\text{m}}$Te and will be ignored in that case. Therefore, the total probability of an un-vetoed $^{133}$Te decay from ground state only to $^{133}$I is $(1 - 0.29) \times (1 - 0.0068) = 0.705$. The calculation will proceed from this point similarly to that of $^{133}$Sb. So if a ND occurs, the probabilities of a ground state only $^{133}$Te decay occurring in the active volume and on the cathode are:

$$
\begin{aligned}
P^{Te}_{active} &= 0.705 \int_0^\infty P_i(z) \times [1 - (1-\alpha')e^{-\frac{d-z}{v\tau'}}]dz \\
&= 0.149 \\
P^{Te}_{cathode} &= 0.705 - P^{Te}_{active} \\
&= 0.556
\end{aligned}
\tag{2.6}
$$

In the above equations $\alpha' = 0.24$ is the $\beta$ decay neutral fraction. If the $^{133}$Sb decays to $^{133\text{m}}$Te, there is a 17% chance this will dexcite to the ground state before decaying to $^{133}$I. This possibility is included in the MC simulation of the metastable PDF. The calculation of the volume specific decay probabilities for $^{133\text{m}}$Te is similar to that of the ground state. It gives $P^{mTe}_{active} = 0.050$ and $P^{mTe}_{cathode} = 0.240$.

The calculation continues recursively for the case of $^{133}$I. The initial distribution in the active volume of $^{133}$I nuclei resultant from an initial nucleon decay and subsequent daughter decays is:

$$
P'_i(z) = P_i(z) \times [\alpha' + (1-\alpha')(1 - e^{-\frac{d-z}{v\tau^*}})] \tag{2.7}
$$

where $\tau^* = 2015.16$s is the weighted average of the lifetimes for $^{133\text{m}}$Te and $^{133}$Te. Multiplying in the decay distribution term and integrating over z gives:

$$
\begin{aligned}
P^{I}_{active} &= \int_0^\infty P'_i(z) \times [1 - (1-\alpha')e^{-\frac{d-z}{v\tau''}}]dz \\
&= 0.046 \\
P^{I}_{cathode} &= 1 - P^{I}_{active} \\
&= 0.954
\end{aligned}
\tag{2.8}
$$

where $\tau''$ is the lifetime of $^{133}$I. These values represent the probability that an $^{133}$I decay will occur in the corresponding detector component given that a nucleon decay to $^{133}$Sb has occured in the active volume.

For decays in the inactive volume, it is assumed that there is effectively no ion drift. The ionized daughter nuclei outside the Teflon may drift a short distance to the nearest ring, but this has little impact on the shape or efficiency of the spectra since the decays must make an energy deposit in the fiducial volume to be detected and are therefore likely $\gamma$ events. Probabilities can be written down for a given daughter decay to occur in the inactive volume after the 1 min veto given that the ND occurred in the inactive volume. For $^{133}$Sb this probability is just:

$$P^{Sb}_{inactive} = 1 - \int_0^{t_d} \frac{1}{\tau} e^{-t/\tau} dt = 0.7587 \tag{2.9}$$

For $^{133}$Te and $^{133\mathrm{m}}$Te:

$$\begin{aligned} P^{Te}_{inactive} &= 0.71(1 - 0.0068) = 0.705 \\ P^{mTe}_{inactive} &= 0.29 \end{aligned} \tag{2.10}$$

where, again, the effect of the veto dead time on $^{133\mathrm{m}}$Te is negligible. For the case of $^{133}$I, the veto dead time contribution is again negligible; and there is no division between metastable and ground state. Therefore, the probability is unity that an $^{133}$I decay occurs in the inactive LXe given that a nucleon decay to $^{133}$Sb occurs there.

The decay fractions calculated in this manner for each daughter and decay region are summarized in table 2.2:

**Table 2.2:** Analytically calculated decay fractions. These numbers are the probability that a specific daughter decay will occur in a detector region assuming a ND to $^{133}$Sb has occurred in the corresponding region. For the active volume and cathode values the corresponding region is the active volume. Thus it can be seen that the active and cathode values sum to the same value as the inactive.

| Daughter Isotope | Active LXe | Inactive LXe | Cathode Surface |
|---|---|---|---|
| $^{133}$Sb | 0.452 | 0.759 | 0.307 |
| $^{133}$Te | 0.149 | 0.705 | 0.556 |
| $^{133\mathrm{m}}$Te | 0.050 | 0.29 | 0.240 |
| $^{133}$I | 0.046 | 1 | 0.954 |

**Table 2.3:** Detection efficiencies of daughter decay PDFs determined by MC simulation.

| Daughter Isotope | Active LXe | Inactive LXe | Cathode Surface |
|---|---|---|---|
| $^{133}$Sb | 0.1268 | 0.0335 | 0.04925 |
| $^{133}$Te | 0.1419 | 0.0122 | 0.0616 |
| $^{133m}$Te | 0.2201 | 0.0289 | 0.08719 |
| $^{133}$I | 0.0963 | 0.0016 | 0.0354 |

### Signal Weights

For the purposes of the analysis, it is necessary to know the probability that a daughter decay will be detected in a specified region given that a ND occurred anywhere in the LXe. This means that it is necessary to multiply volume fractions and efficiencies into the probabilities calculated above. The active volume constitutes 129.86 kg of LXe and the inactive 39.35 kg. Therefore, the active volume fraction is 0.7674 and the inactive volume fraction is 0.2326. As previously discussed, the detection efficiency is defined as the number of MC events detected that are within the desired energy range divided by the total number of MC events simulated. So it represents the probability that a daughter decay in a specific detector region will be detected and pass all analysis cuts. The MC efficiencies are listed in table 2.3. The final weights associated with each daughter decay are the products of the decay probabilities, the mass fractions, and detection efficiencies associated with each daughter decay. They are summarized in table 2.4. These weights represent the probability that a given decay is detected in a specified region of the detector assuming a nucleon decay to $^{133}$Sb has occurred.

**Table 2.4:** Signal weights of daughter decay PDFs. These values are the product of the efficiencies, the volume ratios, and the decay fractions. They are the probability that a given daughter decay will occur in a specific detector region, assuming that a ND occurred anywhere in the detector.

| Daughter Isotope | Active LXe | Inactive LXe | Cathode Surface |
|---|---|---|---|
| $^{133}$Sb | 0.0439(59) | 0.0059 | 0.0116(23) |
| $^{133}$Te | 0.0154(42) | 0.0020 | 0.0267(18) |
| $^{133m}$Te | 0.0084(26) | 0.0019 | 0.0161(10) |
| $^{133}$I | 0.0035(16) | 0.0004 | 0.0259(6) |

It should be noted that these calculations assume that the initial daughter is $^{133}$Sb. For the case in which the initial daughter is $^{133}$Te, the calculation proceeds similarly. In the next section the final signal weights will be calculated. The $^{133}$Te chain results will be shown there.

**Monte Carlo Weight Validation**

A simple MC simulation of the decay fractions was implemented in Python. This MC tracked $10^7$ decay daughters. Each was given a random z position drawn from a uniform distribution. It is given a charge state with 50% probability of being ionized. Then a time to $\beta$ decay is generated from an exponential distribution with the correct time constant. If it is ionized it will be moved in z the appropriate distance. If the distance moved is greater than the distance to the cathode, then the decay is counted as having occurred on the cathode. If not, then it is counted as having occurred in the active volume. If the decay occurs before the 1 min veto dead time then it is not counted at all. Subsequently, another time to decay will be generated from a exponential distribution with the next time constant in the decay chain. The location of the decay at that time is then determined. This process continues until the end of the chain or until an ion reaches the cathode. After the first decay 71% of the ions are selected as ground state $^{133}$Te and 29% are treated as $^{133\mathrm{m}}$Te. Each ion will be given a charge state with 76% probability of being ionized. The fraction $f_c$ of NDs that occur in the active volume and result in a daughter decay on the cathode are calculated by dividing the number of ions at the cathode for each daughter in the chain by the total number of simulated nucleon decays. The fraction of decays occurring in the active volume is just $f_a = 1 - f_c$. The fraction of all NDs that occur in active or inactive volumes of the detector that result in a daughter decay in the active volume(cathode) is given by multiplying $f_a(f_c) \times 0.767$. Also, 23.3% of NDs in the whole detector will result in daughter decays in the inactive volume. The final weights are obtained by multiplying these results by the efficiencies associated with each individual daughter decay. The final weights represent the probability that a ND anywhere in the detector will result in a detected event passing all analysis cuts associated with the corresponding daughter in the given detector region.

The MC decay fractions for active and cathode are listed in table 2.5. The results of which match the analytical model above very well for $^{133}$Sb,$^{133m}$Te, and $^{133}$I with a small correction for $^{133}$Te. These are the most accurate decay fractions and the final weights, calculated in accordance with them, are tabulated in table 2.6 for $^{133}$Sb. The weights are used in the analysis to scale the corresponding PDFs along with a corresponding SS or MS fraction. The weighted sum gives the final signal model PDF, which is shown in Fig. 2.9.

Weights are calculated in exactly the same way for the chain starting with $^{133}$Te. The results obvioulsy differ for this chain but it is not necessary to describe each step in the calculations. The final MC calculated weights for the $^{133}$Te chain are shown in table 2.7.

**Table 2.5:** MC decay fractions of $^{133}$Sb chain daughters.

| Daughter Isotope | Active LXe | Cathode Surface |
|---|---|---|
| $^{133}$Sb | 0.452 | 0.307 |
| $^{133}$Te | 0.141 | 0.564 |
| $^{133m}$Te | 0.050 | 0.240 |
| $^{133}$I | 0.047 | 0.953 |

**Table 2.6:** MC based detection probabilities for triple nucleon decay to $^{133}$Sb. The largest weight is antimony decay in the active volume. This $\beta$ decay is thus the largest contributor to the overall signal PDF.

| Daughter Isotope | Active LXe | Inactive LXe | Cathode Surface |
|---|---|---|---|
| $^{133}$Sb | 0.0439 | 0.0059 | 0.0116 |
| $^{133}$Te | 0.0154 | 0.0020 | 0.0267 |
| $^{133m}$Te | 0.0084 | 0.0019 | 0.0161 |
| $^{133}$I | 0.0035 | 0.0004 | 0.0259 |

**Table 2.7:** MC based detection probabilities for triple nucleon decay to $^{133}$Te. Again the largest weight is associated with the first $\beta$ decay in the active.

| Daughter Isotope | Active LXe | Inactive LXe | Cathode Surface |
|---|---|---|---|
| $^{133}$Te | 0.0538 | 0.0027 | 0.0214 |
| $^{133}$I | 0.0097 | 0.0004 | 0.0236 |

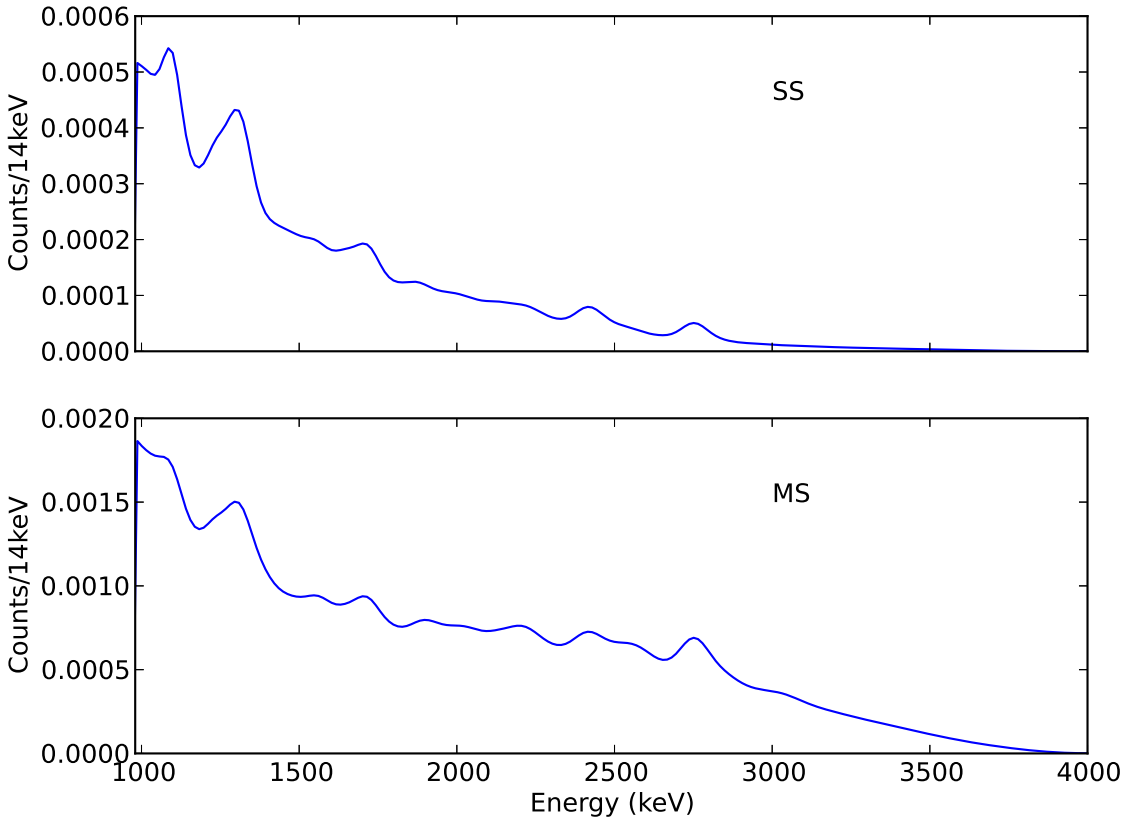


**Figure 2.9:** The weighted and summed signal PDFs for decay to $^{133}$Sb are shown. These are the final PDFs used in the fit. In the fit, they are scaled only by the number of nucleon decays to $^{133}$Sb and a normalization factor.

## 2.5 Experimental data and analysis

### 2.5.1 Fitting Procedure

The number of signal events in the data set is determined by simultaneously fitting both SS and MS models to the low background energy spectrum. The fit is performed by minimizing a negative log likelihood (NLL) function that can be written as:

$$-\ln L = \sum_i [(\mu_i^{SS} + \mu_i^{MS}) - (k_{obs,i}^{SS} \ln \mu_i^{SS} + k_{obs,i}^{MS} \ln \mu_i^{MS})] + G_{const} \tag{2.11}$$

where $k_{obs,i}^{SS(MS)}$ is the number of events observed in the $i^{th}$ bin of the SS(MS) energy spectrum, $\mu_i^{SS(MS)}$ is the number of events predicted by the model in the $i^{th}$ bin of the SS(MS) energy spectrum, and $G_{const}$ is a set of Gaussian constraints applied to the fit to constrain nuisance parameters that reflect systematic uncertainties in the fit [11]. The uncertainties will be discussed in more detail in Sec. 2.5.2.

The expected number of events in the $i^{th}$ bin, $\mu_i^{SS(MS)}$ is calculated as:

$$\mu_i^{SS(MS)}(\mathbf{s}, \mathbf{n}, N) = \int_i F^{SS(MS)}(\mathbf{s}, \mathbf{n}, N, E) dE \tag{2.12}$$

where $F^{SS(MS)}(\mathbf{s}, \mathbf{n}, N, E)$ represents the MC generated PDFs of the model. It is defined as:

$$\begin{aligned} F^{SS}(\mathbf{s}, \mathbf{n}, N, E) &= N \sum_j n_j s_j f_j^{SS}(E) \\ F^{MS}(\mathbf{s}, \mathbf{n}, N, E) &= N \sum_j n_j (1 - s_j) f_j^{MS}(E) \end{aligned} \tag{2.13}$$

where N is an overall normalization parameter, $s_j$ is the fraction of simulated events that were single-site events for the $j^{th}$ PDF, $n_j$ is the total number of events in the $j^{th}$ PDF, and $f_j^{SS(MS)}(E)$ is the $j^{th}$ PDF as a function of energy.

The Gaussian constraint terms in $G_{const}$ are used to constrain nuisance parameters in the fit and also reflect systematic uncertainties in the fit. The parameters constrained are the overall

normalization N, the set of all single-site fractions $s_j$, a signal normalization parameter that scales only the signal PDF, a Radon decay rate parameter, and a neutron capture rate parameter. The constraints adjusted specifically for this analysis were all of the form:

$$0.5\left(\frac{\rho-\rho_0}{\sigma}\right)^2 \tag{2.14}$$

where $\rho$ is the constrained parameter, $\rho_0$ is its expected value, and $\sigma$ is the uncertainty associated with that parameter. The nuisance parameters and the errors associated with each will be discussed in more detail in Sec. 2.5.2.

The fit is carried out by varying the $n_j$'s and all the constrained parameters listed above to minimize Eq. 2.11 using the MINUIT minimization package. Once this is done, the parameter of interest in this analysis, $n_{signal}$ is varied around its best fit value in what is known as a profile likelihood scan. At each point in the profile the number of signal decays is fixed and all other parameters are varied to minimize Eq. 2.11. The resulting change in the NLL from the overall best fit is calculated. The points at which the $\Delta$NLL = 0.5 represent the $1\sigma$ confidence level (CL) and the points at which $\Delta$NLL = 1.4 represents the 90% CL. In the case where the best fit is consistent with zero signal, the 90% CL is used to set a lower limit on the lifetime of the signal decay. This procedure is followed for both $^{133}$Sb and $^{133}$Te separately.

### 2.5.2 Systematic Uncertainties

Systematic uncertainties are accounted for in this analysis in the same way as in [29, 30]. The systematic uncertainties associated with overall normalization N, signal normalization, and single-site fractions $s_j$ are discussed in this section. These parameters are constrained by the $G_{const}$ terms described in Sec. 2.5.1. Uncertainties are represented by $\sigma$ in the denominator of Eq. 2.14. Larger uncertainties decrease the effect on the NLL of widely varying the nuisance parameters from their expected values. This makes the fit less sensitive to changes in the other parameters which, in turn, flattens the $\Delta$NLL profile, which effectively widens the confidence intervals of the fits.

### Single-site Fraction Uncertainty

The SS fraction uncertainty was calculated in a similar way as in [11]. The SS fractions for $^{228}$Th and $^{60}$Co calibration data are compared to the SS fractions of MC events. The discrepancies as a function of energy are shown in Fig. 2.10. The weighted average of these points gives a 4% discrepancy between data and MC. This number is used for the SS fraction uncertainty in the Gaussian constraint terms that corresponded to the SS fraction parameters as follows:

$$G_{s_j} = 0.5(\frac{s_j - s_{j0}}{0.04 s_{j0}})^2 \tag{2.15}$$

where $s_j$ is the SS fraction fit parameter for the the jth PDF and $s_{j0}$ is the expected SS fraction derived from the MC of the jth PDF.

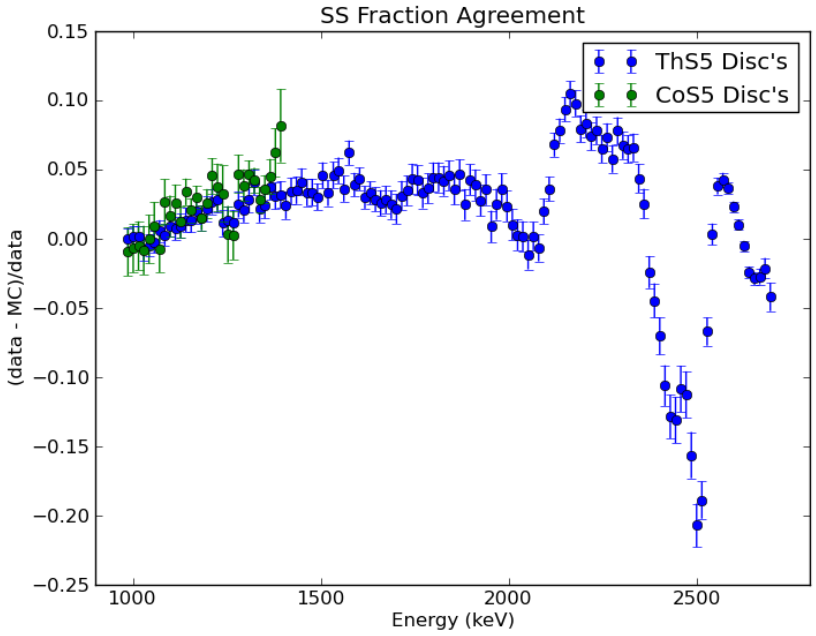


**Figure 2.10:** SS fraction agreement. The fractional discrepancy between data and MC is plotted as a function of energy for both $^{228}$Th and $^{60}$Co calibration sources. Widely discrepant points at higher energies are associated with the Compton shoulder of large $\gamma$ peaks large peaks in the calibration spectrum.

**Overall Normalization Uncertainty**

The uncertainty associated with the overall normalization is due to error associated with the rate at which events occur in the detector. The event rates predicted by the MC are not perfectly consistent with the rate at which events occur in the detector during calibration runs. For a similar analysis used in [30], this uncertainty is reflected by the overall normalization uncertainty and was set at 8.6%. A major difference between these two analyses is the extension of the fiducial volume toward the cathode by 9 mm in this analysis. This could affect the agreement between data and MC regarding the rate of events in the detector. To incorporate this additional uncertainty regarding the event rate, a rate agreement study was done using over 150 $^{228}$Th source calibration runs taken throughout the dataset used in this analysis. This study involved measuring the discrepancy between the efficiency of the calibration source data runs with the efficiency predicted by the MC. The efficiency of the calibration data runs is calculated by dividing the number of events passing all cuts by the total number of source decays derived from the known activity of the source. For each calibration run the discrepancies between data and MC efficiencies for the standard and extended fiducial volume are shown in Fig. 2.12 and the efficiencies for each fiducial volume in data and MC are shown in Fig. 2.11. On average the discrepancy between data and MC increased by 0.2%. A standard procedure of adding these two uncertainties in quadrature would not change the To account for this conservatively in the final fit, the 8.6% overall normalization error was increased to 9%.

The actual discrepancies in Fig. 2.12 are slightly higher than 9%. This is because the rate agreement analysis described above is somewhat naive compared to what was done in [30]. The pile up of events in time is not taken into account as accurately. The data in Fig. 2.11 does, however, show that the effect on the discrepancy of increasing the fiducial volume is small. Thus a small increase to 9% from the 8.6% accounting for the rate uncertainty in [30] was appropriate.

**Signal Normalization Uncertainty**

The signal normalization parameter scales the signal in the final fit. Its corresponding uncertainties is used to reflect uncertainties regarding the shape differences between the data and MC

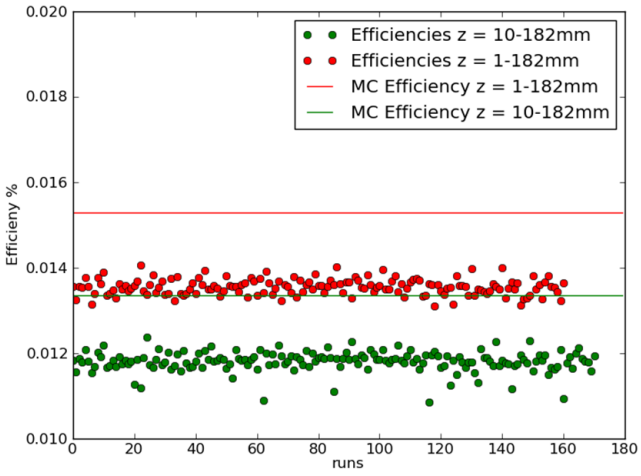


**Figure 2.11:** Source efficiencies in data and MC are compared for both Z cuts. Lengthening the fiducial volume has the effect of increasing the efficiency since it increases the solid angle of fiducial volume relative to the calibration source, which is emitting $\gamma$'s in all directions. This and other factors are adequately captured in the MC, thus the gap between data and MC efficiencies is largely unchanged between the two cuts.

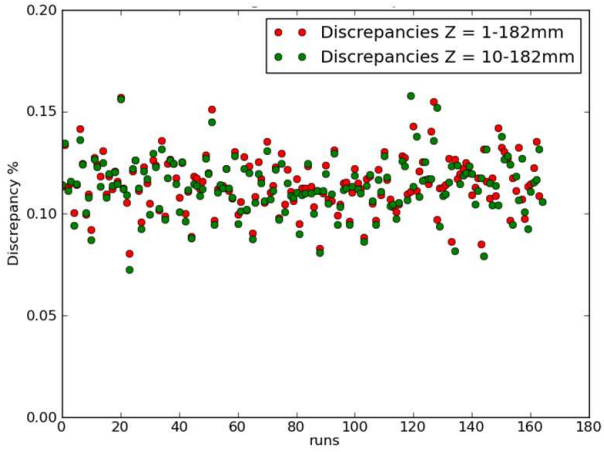


**Figure 2.12:** Source rate agreement studies indicate to what extent the uncertainty regarding the rate of events in detector depends on the z-dimension of the fiducial volume cut. The discrepancy in rate between data and MC is shown for each run for both the extended and shorter fiducial volumes.

energy spectra, backgrounds that are potentially missing from the model, and the uncertainty in the ion fractions used to weight the different signal components.

The shape difference between data and MC was studied in the following way. First, the source calibration data runs with all three ($^{226}$Ra, $^{60}$Co, $^{228}$Th) sources were compared to MC and the differences between the normalized shapes at energies between 1.0 and 2.7 MeV are shown in Fig. 2.13 for the $^{228}$Th source for SS and MS events. A linear function is fit to the ratio of data/MC for each source and for MS and SS separately. This function is then used to re-weight the MC spectra by multiplying each bin of each PDF by a corresponding function evaluated at the bin energy. Three functions were generated: one from $^{228}$Th calibration data, one from $^{226}$Ra calibration data, and one from $^{60}$Co calibration data. The function generated from $^{228}$Th data is used to scale most of the background components. The function generated from $^{226}$Ra is used to scale the radon originated background PDFs. The $^{60}$Co derived function is used to scale the cobalt background.

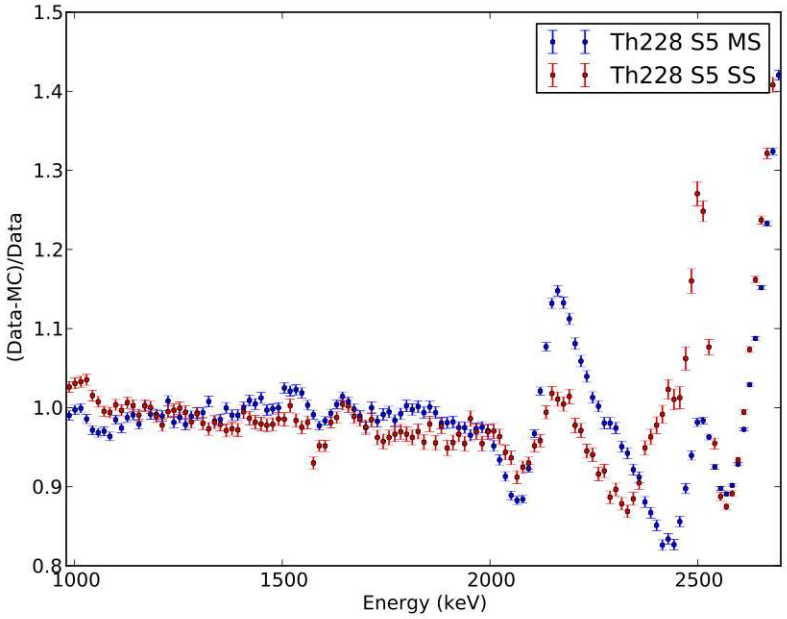


**Figure 2.13:** The source agreement ratio MC/data. The discrepancy between data and MC is most significant in this energy region.

Once the dataset is un-skewed in this manner, it is then used as a distribution to generate toy MC datasets. These toys are injected with a variable number of signal events and then refit with the standard background and signal models. The shape uncertainty is then derived from the discrepancy between the injected and fit number of events. For the case of nucleon decay to $^{133}$Sb, the difference between fit and injected number of events was close to constant around 7% for different number of injected events. In the case of nucleon decay to $^{133}$Te, the difference was linear below 5000 injected events and approached a constant difference of 5000 discrepant events above that. The fractional discrepancy for a given number of injected events is shown in Fig. 2.14. This data is interpolated to get a value for the shape uncertainty at each corresponding point in the NLL profile for the $^{133}$Te fit. Thus a different uncertainty ($\sigma$ in Eq. 2.14) associated with signal normalization is used for different numbers of injected events when the NLL profile was performed for nucleon decay to $^{133}$Te.

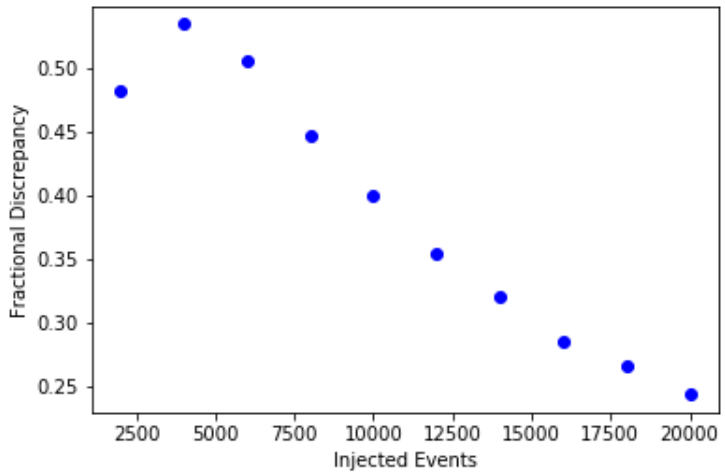


**Figure 2.14:** Fractional fit event discrepancies for different numbers of injected events in the $^{133}$Te fit. The shape uncertainty used in the $^{133}$Te NLL profile is derived from this data.

The signal normalization uncertainty is also used to reflect uncertainty regarding the completeness of the background model. It is possible that the set of PDFs included in the background model do not accurately represent every background source in or near the detector. In order to account

for this possibility various sources were simulated in non-standard locations. The PDF generated at this non-standard location was then substituted into the background model for the PDF from the standard location. The adapted model wass then fit to the data and the discrepancy from a standard result was calculated. For example, $^{238}$U is normally simulated as decaying in the copper of the LXe vessel. However, the inner cryostat is made out of copper as well and may contain some $^{238}$U. Thus it is possible that there are significantly background events coming from the uranium in the inner cryostat as well as from the vessel. To account for this possibility conservatively, a PDF of $^{238}$U was simulated in the cryostat and substituted into the fit for the PDF that represents uranium decays in the vessel. The change in the fit was then used to reflect the uncertainty regarding the location of this background source. This was done for a number of potential background sources locations. The results are summarized in table 2.8. These values are summed in quadrature resulting in a 17% shape uncertainty component due to background model uncertainty.

**Table 2.8:** Background substitution results are summarized. These values are the change to the fit number of $^{133}$Sb(Te). They are summed in quadrature with the other components of the signal normalization uncertainty.

| Isotope | New Location | Discrepancy |
|---|---|---|
| $^{232}$Th | HFE | 15% |
| $^{232}$Th | Outer Cryostat | 8% |
| $^{238}$U | HFE | 2% |
| $^{238}$U | Outer Cryostat | 2% |
| $^{328}$U | Inner Cryostat | 2% |

The background substitution procedure was applied to $^{60}$Co as well by substituting a PDF for $^{60}$Co decays originating in the calibration source tube just outside the copper vessel for $^{60}$Co decays originating from the vessel itself. This caused a 33% change in the fit result, which indicates that the fit is particularly sensitive to differences between the two PDFs. To investigate this more rigorously a two-dimensional NLL profile scan was done with the numbers of source tube and vessel $^{60}$Co decays as the scan parameters. The result of this scan is shown in Fig. 2.15. This scan indicates that the scenario in which no $^{60}$Co decays are coming from the vessel is excluded to $6\sigma$.

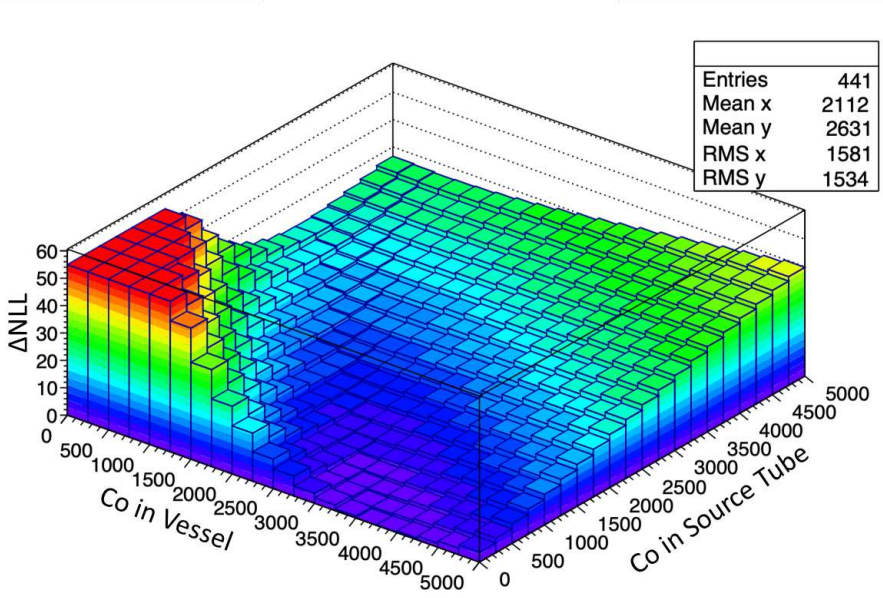


**Figure 2.15:** To understand the relevance of $^{60}$Co in the source tube to the background model, a $\Delta$NLL surface was created. The scenario in which there is no $^{60}$Co in the vessel is excluded to $6\sigma$. The best fit lies along the axis with no source tube $^{60}$Co, but the scan does show $\sim$1000 source tube events within $2\sigma$.

The scan does not however exclude the possibility that some $^{60}$Co decays originating in the source tube are present in the dataset. In order to account for these findings, PDFs from $^{60}$Co both in the vessel and in the source tube were incorporated into the background model.

## 2.6 Results

The experimental SS and MS energy spectra were fit simultaneously with an overall model composed of background and signal PDFs. The fit was performed separately for both $^{133}$Sb and $^{133}$Te chains. The resulting fit for the $^{133}$Sb chain is shown in Fig. 2.16. For the $^{133}$Te chain, the best fit was to zero signal events. Thus the plot of the energy spectrum fit is not shown. In order to determine whether or not a significant level of signal is observed or to set a limit on the lifetimes, a profile likelihood scan was performed for both chains. The scans are shown in Fig. 2.17. The fact that the NLL is less than $3\sigma$ at 0 events for both profiles indicates that the data is consistent with zero signal events in either case. The number of events at the upper 90% confidence level is used to calculate a lower limit on the lifetime of the decay. For decay to $^{133}$Sb the limit is 2800 events

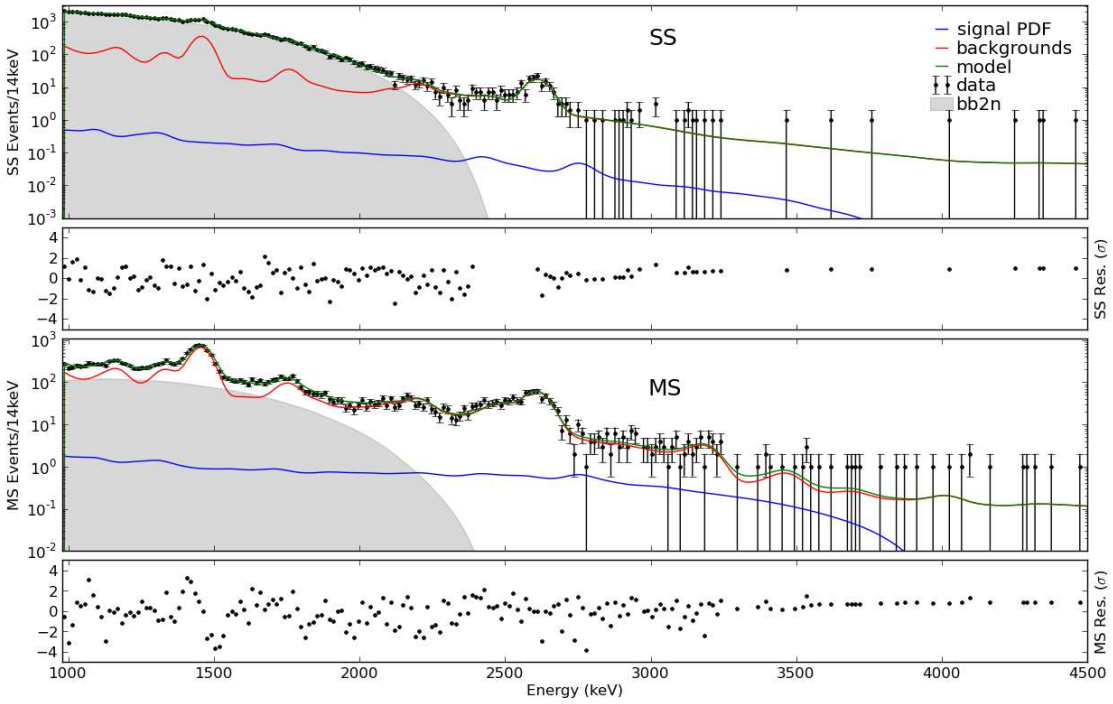


**Figure 2.16:** SS and MS energy spectra fits with an overall model composed of the background model and the signal model. The best fit for the $^{133}$Sb chain had 965 signal events. The best fit for $^{133}$Te was to zero signal events. The residuals for both spectra are shown as well.

corresponding to a lifetime limit of $3.3\times10^{23}$ yrs, and for decay to $^{133}$Te it is 4900 events and a liftime limit of $1.9\times10^{23}$ yrs.

In conclusion, results are reported here from a search for baryon number violating decays in $^{136}$Xe using two years of data from the EXO-200 LXe TPC. The results show no statistically significant evidence for nucleon decay to either $^{133}$Sb or $^{133}$Te. The lifetime limits obtained are the most stringent to-date surpassing previous results [33] by a factor of 9 and 7 for $^{133}$Sb and $^{133}$Te respectively.

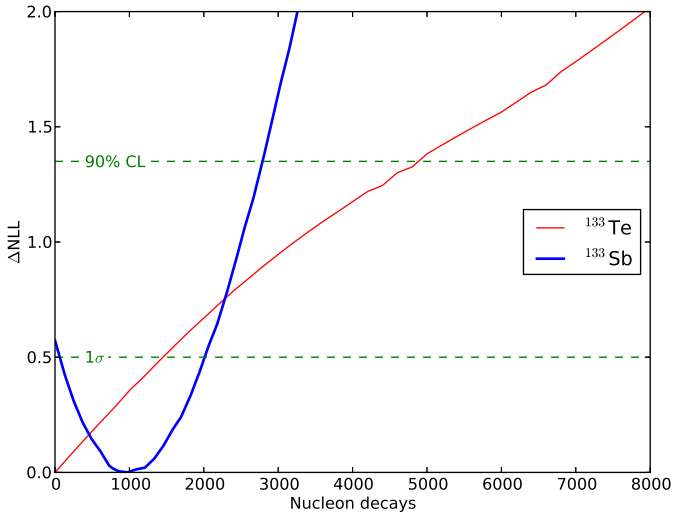


**Figure 2.17:** NLL profiles for $^{133}$Sb and $^{133}$Te decay chains. The dashed lines represent the $1\sigma$ and 90% confidence limits (C.L.).

# Chapter 3

# Liquid Xenon Apparatus

A LXe experimental apparatus has been designed and constructed to test the concept of freezing barium in a SXe matrix. Xenon freezing is achieved via a Joule-Thomson (JT) cryoprobe, which is described in Sec. 3.1. The probe can dip in and out of a copper cell that can be filled with liquid or gaseous xenon. The cell and xenon system will be discussed in Sec. 3.2. The system used to raise and lower the probe is described in Sec. 3.3. Inside of the cell are suspended electrode plates and a barium metal sample that can be ablated to deposit $Ba^+$ ions onto a SXe sample. The electrodes and ablation system is described in detail in Sec. 3.4. Once the barium is deposited into a SXe matrix on the probe it is lifted to an observation region that allows for excitation and detection of fluorescence. Discussion of this optical apparatus can be found in Sec. 3.7. Measurement of the barium fluorescence lifetime was carried out on a separate apparatus, which is discussed in Sec. 3.8.

## 3.1 Joule-Thomson Cryoprobe

A Joule-Thomson (JT) cryoprobe is used to capture barium in a SXe matrix and extract it from the LXe cell. A commercial JT probe designed for medical applications was obtained from Galil Medical [43]. A diagram of the probe is shown in Fig. 3.1. It has a JT nozzle at the end of a small flexible metal tube that carries high pressure argon down to the nozzle. The nozzle and tube is surrounded by an outer stainless steel (SS) tube sealed at the end below the nozzle with a cap. Originally the cap was sharp for medical purposes but has been ground down to a rounded shape for this work. The diameter of the probe is 0.06". The high pressure argon gas expands as it exits the nozzle and cools by the JT effect. This cold gas flows by the end and walls of the steel tube cooling them. It then flows back up the steel tube and is vented through a plastic hose that also surrounds the flexible argon tube. As cool gas flows back up the steel tube it is in thermal contact with a coil of the argon input tube. This pre-cools the input gas and allows the probe to cool more

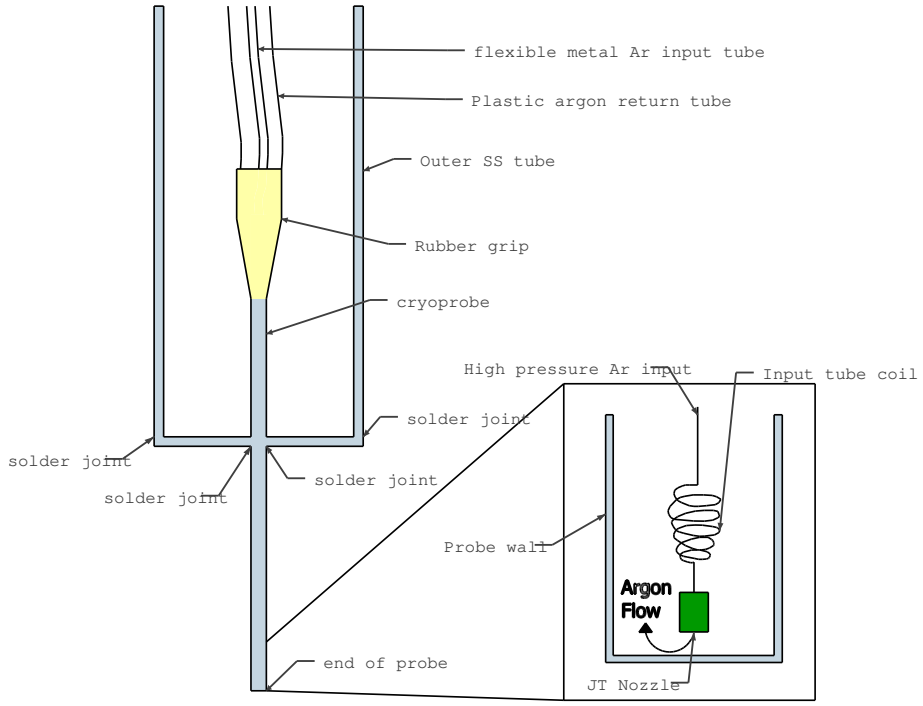


**Figure 3.1:** Diagram of the probe without window attached. The probe was soldered to a stainless steel tube to isolate the rubber and plastic components from the clean xenon. Inset shows detail of the internal parts of the probe tip.

effectively. The argon is fed in from a ultra-high purity 6000 psi bottle and a high purity, high pressure regulator. Typically the input gas is pushed through the probe at between 1000-2000 psi. A photo of a SXe sample frozen with a JT probe in the LXe cell is shown in Fig. 3.2. Control of the cooling power of the probe is achieved by adjusting this pressure. The probe is soldered to a larger diameter tube via a steel washer. This tube keeps the plastic components out of contact with the high purity xenon gas. Solder connections were chosen because welding might have melted the thin argon tube or damaged the JT nozzle. The larger tube was welded to a conflat flange that is in turn mounted to a long bellows. This bellows will be described in greater detail in Sec. 3.3.

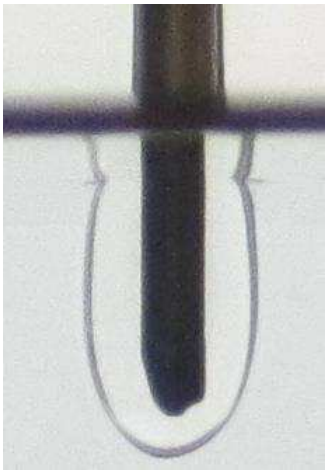

**Figure 3.2:** A photo of a SXe ball frozen from LXe is shown. This was done using the JT probe described here.

Another probe from Galil was used for a number of tests that had an evacuated jacket soldered around it. A diagram of this probe is shown in Fig. 3.3. The vacuum jacket served to insulate the sides of the probe and keep it from developing thick layers of SXe or condensing LXe out of the gas. This makes it possible to freeze xenon and maintain a sample at a wider range of LXe temperatures due to the fact that condensation onto the probe is decreased because the cooling is focused near the bottom of the probe. A photo of this probe with SXe successfully extracted to upper cell is shown in Fig. 3.4.

The barium fluorescence tests discussed in Ch. 4 were done with a sapphire window from Meller Optics [44] attached to the end of the original probe (Fig. 3.1) with a copper holder. A diagram of this holder and its connection to the probe is shown in Fig. 3.5. The copper piece makes thermal contact with the probe via a set screw. To improve the contact, a piece of soft indium metal was compressed between the copper and probe. A 1/4" diameter sapphire window was attached to the copper holder via press fit with a compressed indium layer between the window and the copper. A photo of the probe with the copper window holder and window attached is shown in Fig. 3.6. The vacuum jacketed probe was not used to mount the window and holder primarily because the vacuum jacket developed a leak and a replacement was more difficult to fabricate. Also, the improved cooling was not necessary for the fluorescent experiments carried out.

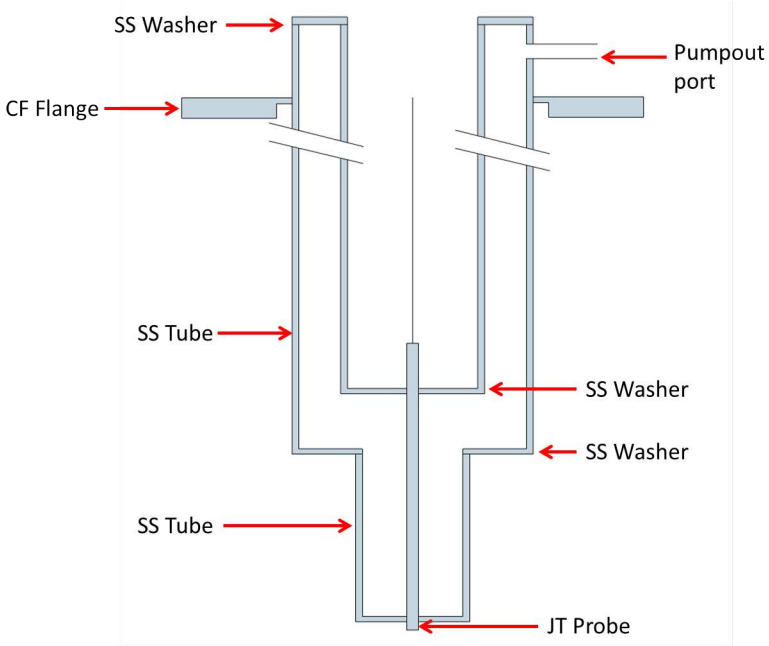


**Figure 3.3:** A diagram of the design of the vacuum jacketed JT cryoprobe is shown.

**Figure 3.4:** A photo of the vacuum jacketed JT cryoprobe is shown with SXe sample extracted to upper cell.

Often, the probe is in a cold xenon environment below 165 K. When the probe is not pressurized with Ar gas, atmospheric gases can back flow into the venting region and thereby come into contact with the JT nozzle itself. As a result, it is possible that water vapor can condense and freeze on and around the nozzle, causing the cooling to fail. This is a possible explanation for instances of cooling failure when the probe was left in a cold environment. To eliminate these failures, the Ar gas flow is initiated in a warmer area (the raised position) where any water can be flushed out prior to significant cooling. The probe is then lowered into the cold xenon environment as cooling continues.

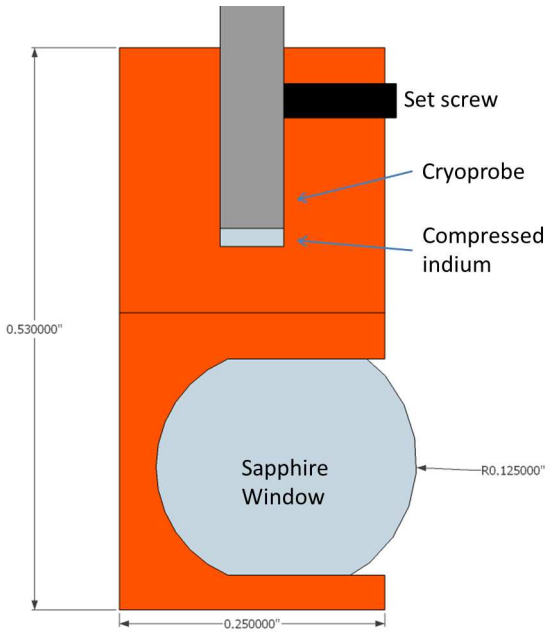


**Figure 3.5:** A diagram of the copper window holder attached to the cryoprobe is shown.

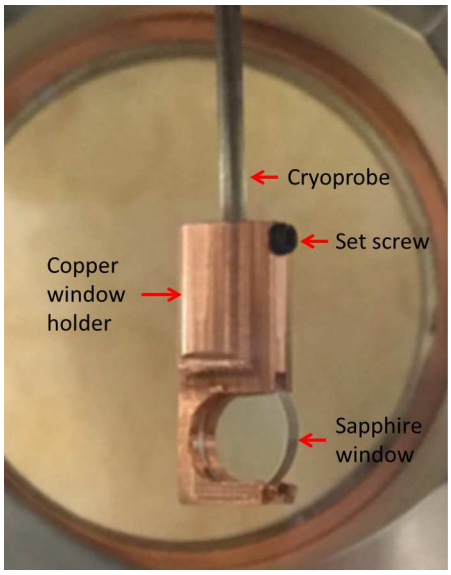


**Figure 3.6:** The copper window holder attached to the unjacketed cryoprobe is shown. The sapphire window used for fluorescence measurements on cryoprobe is also visible.

## 3.2 Xenon System

Liquid xenon is condensed and held in a copper cell, which is cooled by liquid nitrogen [45–47]. The LXe cell has fused silica windows on four sides that are broad-band anti-reflective coated.

The cell is surrounded by an outer vacuum chamber to provide thermal insulation. It also allows the cell to be cooled without condensing atmospheric gas.

The cell is thermally connected to a liquid nitrogen cold trap via approximately 30 copper grounding straps. They are clamped firmly to the cold trap and to a large copper pedestal, which is bolted to the cell and indium sealed. The temperature of the cell is controlled by a resistive heater, which is clamped to the pedestal [46]. The current through the heater is controlled by a Lakeshore 330 temperature controller [48]. It is able to maintain a constant temperature to within 0.1 K between 160 K and 170 K, which is the temperature range primarily used for liquid xenon experiments. In order to keep the cell cold, the cold trap is filled with liquid nitrogen every 1.25 hours. During each fill the nitrogen is pushed into the cold trap at approximately 55 psi for 1 min. It takes roughly 12 hours to cool from room temperature to the set point in the LXe temperature range. The cell can reach approximately 153 K when cooled overnight if no heating is applied.

The cell windows are sealed against the side of the cell using an indium seal. The design of the seal and procedure for installing the windows was changed from what was described in previous theses [45–47]. A basic drawing of the new seal design used is shown in Fig. 3.7. The seal is

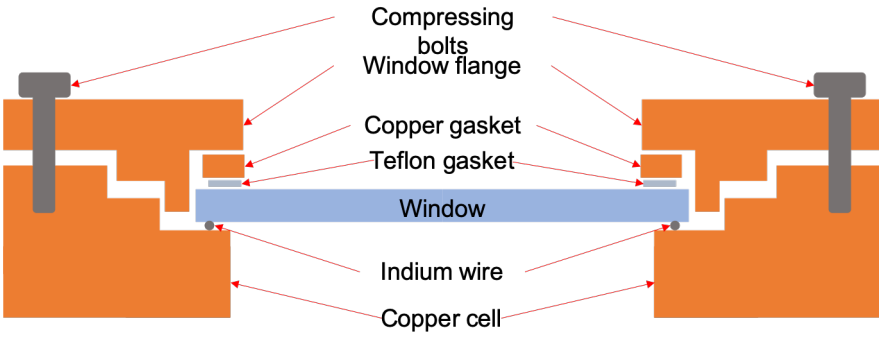


**Figure 3.7:** A simple diagram of the updated sealing method. The downward direction in the diagram is the inside of the cell and the upward is outside.

made by compressing indium wire between the window and the cell. The window flange is used to press the window onto the indium. The Teflon gasket is used to avoid cracking the window when applying the small pressure necessary to make the seal. Prior methods relied on a tongue

and groove seal with indium in the groove created by the outside edge of the window and the cell. The indium was compressed in the prior method by the tongue on the flange. The new method is more reliable and easier to implement. To make the seal both the window and copper surfaces are cleaned thoroughly with acetone then methanol; the wire is then placed on the copper ensuring that the ends overlap. When compressed together this creates an indium O-ring seal. The Teflon and copper gaskets are placed between the flange the window in a manner such that the copper is not touching the window. Finally, the flange is placed over the window and tightened applying force on the gaskets and window. The bolts need only be tightened slightly beyond hand-tight. The maximum torque on the bolts necessary to create a seal is $<$5 ft lbs.

The top of the cell is open to a bellows assembly and an upper observation cell, shown in Fig. 3.8. The bellows allows the probe with a SXe sample to be extracted to the upper cell. Between

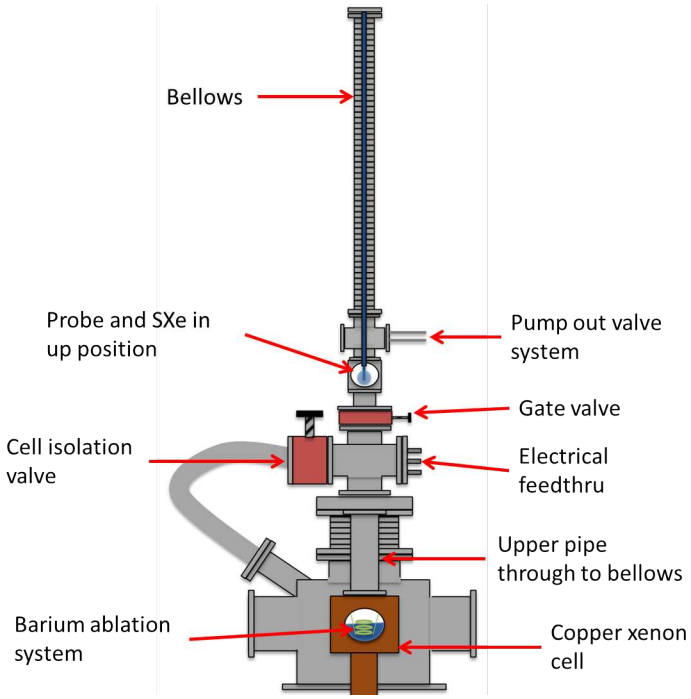


**Figure 3.8:** The LXe apparatus, probe, and lifting system are partially represented. The basic concept is a cooled copper cell containing LXe into which the probe dips to capture a SXe sample and then is extracted via the long bellows at the top of the system.

the LXe cell and upper cell is a gate valve that can be used to isolate the upper cell volume from

the volume below containing LXe. After raising the probe with a SXe sample, it is desirable to decrease temperature of the sample without condensing more xenon onto it. In order to achieve this, the pressure in the upper cell must be decreased as the sample cools such that the xenon pressure in this region coincides with the vapor pressure of xenon at the temperature of the sample surface. In Fig. 3.9, a concept of this system, which has been only partially constructed, is shown. In order to lower the pressure, a pneumatically controlled valve is installed that can be connected to

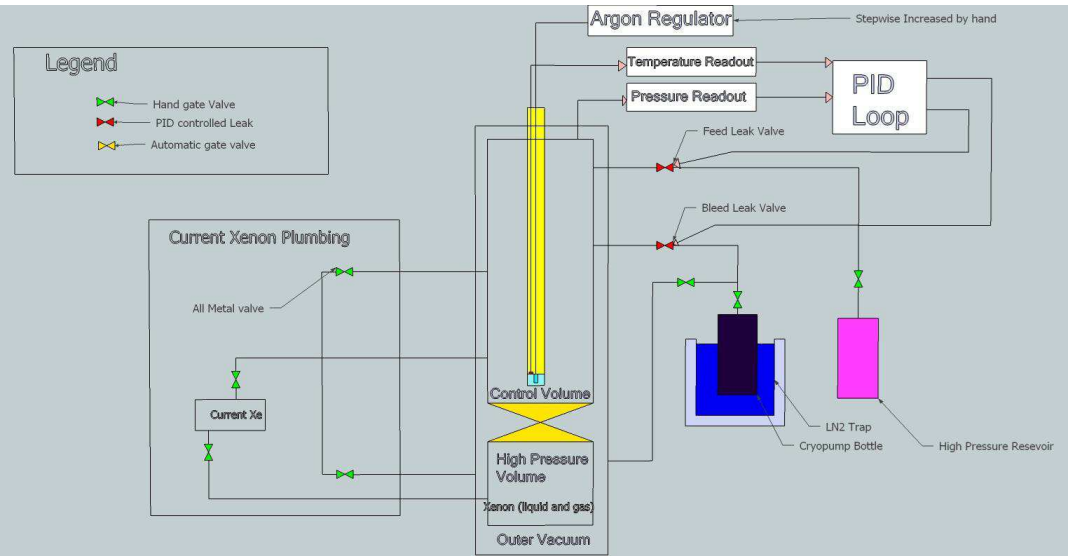


**Figure 3.9:** Diagram of the xenon gas handling system. This system has not been fully constructed at the time of this work. PID control and a high pressure feed valve are not yet implemented fully. The probes discussed in this work lack temperature readout.

a cryopump bottle. This scheme should be capable of reaching and maintaining a specified pressure as long as it is at or below the current pressure of the system. The feed valve for increasing the xenon pressure and the temperature sensor shown in Fig. 3.9 have not been installed at the time of this work.

The five 9's purity or 99.999% pure xenon was purchased from Advanced Specialty Gases [49]. Xenon gas passes from the pressurized gas bottle and through an all metal regulator and a SAES Mono-Torr gas purifier, which removes electro-negative impurities from the xenon before it enters the cell. The cell is held at liquid xenon temperatures and can cool and condense the LXe. The xenon is recovered by cryopumping back into a storage bottle. Cryopumping is done by immersing

the bottom half of the storage bottle in a liquid nitrogen bath. A 3.785 L stainless steel bottle with welded VCR connections was chosen as the storage bottle to avoid cooling connections that might not be robust to thermal shrinking. It was found, for instance, that a Teflon sealed connection to a bottle valve was prone to leaks when cooled below room temperature in the process of xenon recovery.

The pressure of xenon in the cell is measured by a Baratron capacitance manometer, [50] which puts out a 10 V full scale analog signal that is proportional to the pressure. This signal is readout by an Arduino Uno microcomputer and is recorded as ADC counts. The Baratron was calibrated by comparing its output to the pressure measured by a Swagelok 316L VAR analog gauge connected to the xenon system. The results are shown in Fig. 3.10. The resulting calibration is linear and can

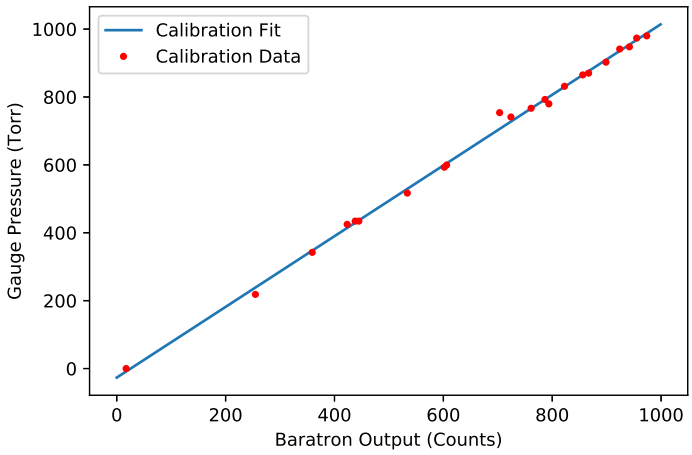


**Figure 3.10:** Calibration curve for the baratron gauge.

be written as:

$$P = aV_{out} + b \tag{3.1}$$

where P is the measured pressure int Torr, $V_{out}$ is the output voltage of the Baratron in ADC counts with $a = 1.04$ Torr/counts and $b = -24$ Torr.

The Arduino uses a TTL signal to actuate switches that turn on or off 120 V AC wall power to open and close the gate, pumpout, and nitrogen valves. It can do all of these things on command or according to a scripted protocol.

## 3.3 Probe Raising and Lowering System

An important aspect of the barium tagging scheme under consideration is the removal of the probe with the SXe sample from the LXe so that it can be further cooled well below the LXe temperature. A lifting system was installed on the LXe apparatus to raise and lower the probe with the SXe sample. A steel bellows to which the probe is mounted allows the probe to be raised and lowered while staying in the LXe environment. When the bellows is compressed and expanded the probe is lowered into and raised out of the copper cell respectively. In the raised position, the bottom of the probe is near the center of a 2.75" conflat cube with four 1.5" viewports on four sides to allow optical access. This is the upper cell mentioned in Sec. 3.2.

The bellows is attached to 2.75" conflat flanges on both ends. It was purchased as a custom order from Bellows Tech Inc. A diagram of the bellows is shown in Fig. 3.11. One concern

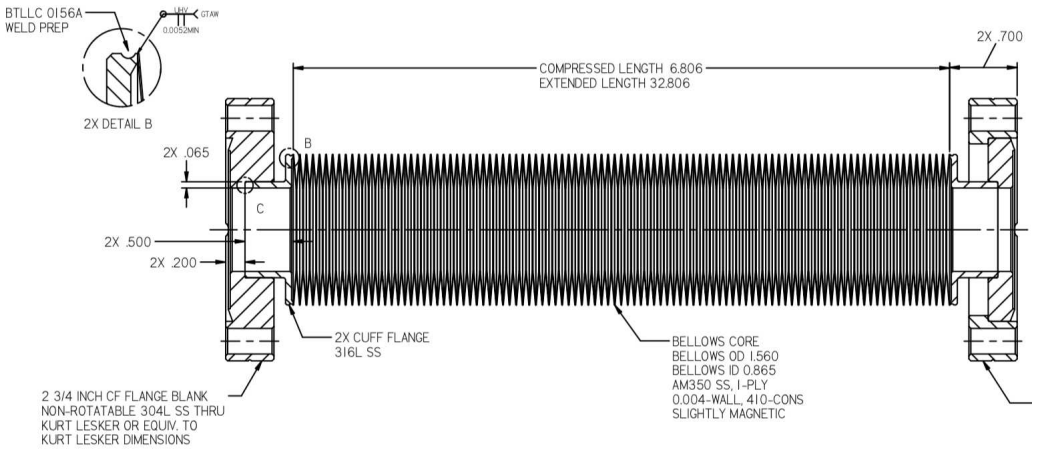


**Figure 3.11:** Technical drawing of the bellows. The guide tube to keep the bellows from buckling when compressed with high internal pressure is not shown.

when designing the bellows system was with buckling of the bellows when there is greater than

an atmosphere of xenon gas inside the bellows. In order to prevent buckling, a tube was welded to the inside opening of the upper flange, and it extends the entire length of the bellows past the bottom flange. As a result, the two flanges and the bellows body are forced to be approximately concentric. The bellows is clamped into a support system, shown in Fig. 3.12, that allows it to be compressed and extended by a motor that turns a screw threaded through a plate clamping the top of the bellows. The full motion of the bellows can be executed as quickly 47 s. The speed of

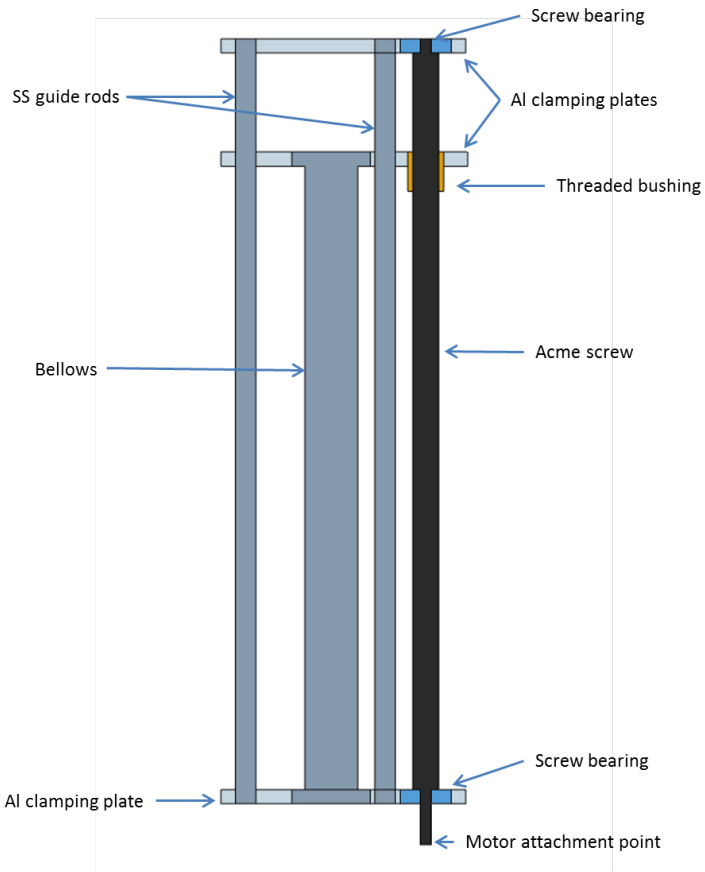


**Figure 3.12:** Diagram of lifting apparatus.

raising and lowering is limited by the motor's torque. The motor used is a 3540i Applied Motion Products stepper motor [51]. It is connected in a high torque parallel input configuration. A custom sprocket and chain set bought from McMaster Carr with a mechanical advantage of 24/9 is also used to increase the torque applied to the screw. A picture of the motor and screw assembly is shown in Fig. 3.13.

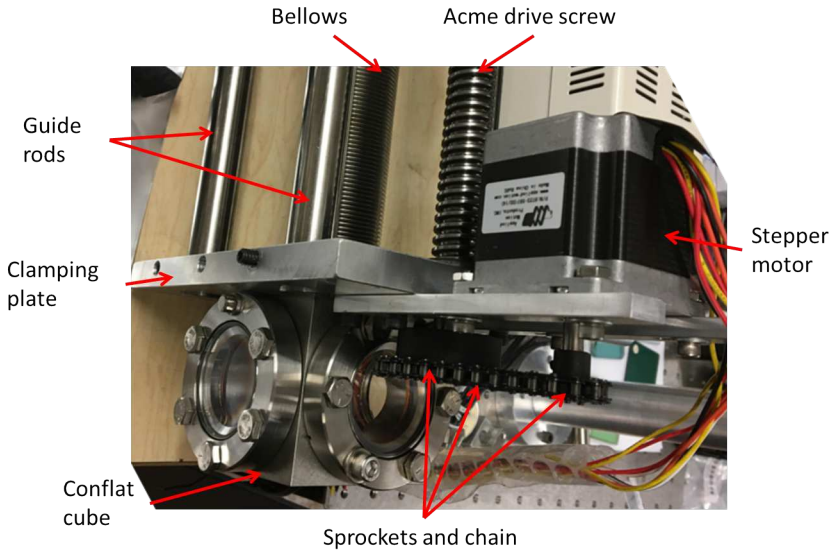


**Figure 3.13:** Photo of the stepper motor and the drive assembly. The 2.75" CF cube is attached to the bottom of the bellows. The sprockets, chain, guide rods, drive screw, clamping plate, and bellows are all visible.

## 3.4 Electrodes and Laser Ablation System

Barium ions are created in gaseous xenon using a laser ablation scheme shown in Fig. 3.14. Laser light from a 1064 nm pulsed Nd:YAG laser is focused by a 40 cm lens incident on the

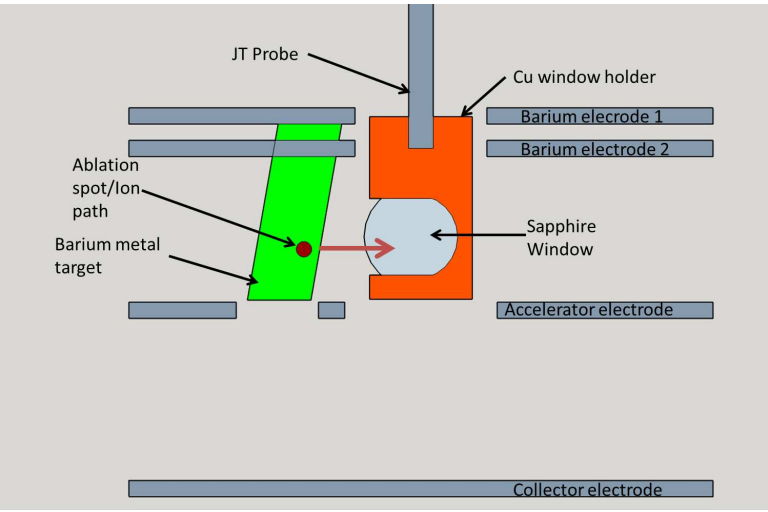


**Figure 3.14:** A simplified diagram of the probe and electrode plates in the configuration is used to collect barium ions from gas on a SXe layer on the sapphire window is shown. The barium metal ablation target and the sapphire window are also shown. Not shown are the electrical connections, quartz rods, and quartz spacers.

surface of the barium sample. The high intensity light ablates and ionizes some Ba metal atoms and produces a cloud of barium and xenon plasma. The ions are drawn off from the edge of the plasma by an electric field created by applying +300 V to the electrodes. Since the probe is grounded to the vacuum system the $Ba^+$ ions will drift in its direction. The probe window is located at the same height as the barium metal when a barium in SXe sample is deposited in xenon gas, as pictured in Fig. 3.15. When liquid extraction is tested, the probe window is below the LXe

**Figure 3.15:** Image of the probe with sapphire window attached in the position for collection of ions in xenon gas. The barium is directly to the left of the probe in this position. The ablation laser strikes the barium sample and creates ions that are pulled from left to right onto the window. The electrodes are visible above and below the probe and barium.

level, which is set at the level of the middle plate. This configuration is shown in Fig. 3.16.

The 1064 nm pulsed laser is a Quanta Ray DCR Nd:YAG laser, which works by exciting emission in an Nd:YAG crystal with flash lamps and activating a Q-Switch to allow lasing to occur for a short period of time. As a result, a 9 ns pulse of light is produced at 1064 nm. Pulses of higher power are produced by this process than is typical with continuous wave lasers. The energy of the pulse can be adjusted by adjusting the lamp energy. It was found using a Coherent FieldMax TOP power/energy meter that a lamp energy of 60 J corresponds roughly to a 1 mJ pulse energy after it passes through deflection optics. The pulse is focused onto the barium sample to create high enough intensity to ablate the barium.

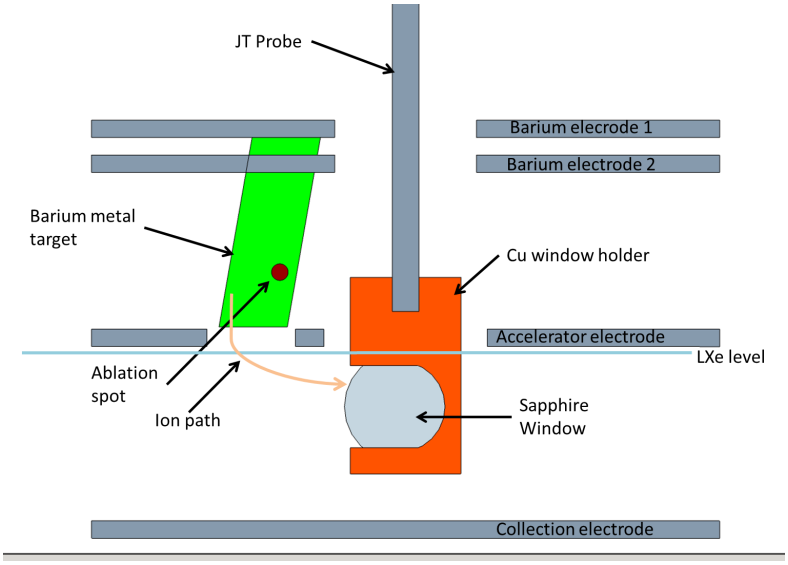


**Figure 3.16:** Simplified diagram of the probe and electrode plates configuration for capture of barium ions out of LXe. The barium metal ablation target and the sapphire window are also shown. Not shown are the electrical connections, quartz rods, and quartz spacers.

The electrodes are suspended from the SS tube attached to the top of the cell. A photo of the fully assembled suspension system and electrodes is shown in Fig. 3.17. The electrodes are


**Figure 3.17:** The plate suspension system is shown. At the top, the aluminum suspension ring is held by set screws pushing out onto the pipe above the LXe cell. The SS rods and guide rings hold up the electrodes and guide the probe as it moves in and out of the pictured assembly.

insulated from each other by quartz posts and spacers, which also hold them up. The plates are suspended using an aluminum suspender ring, which uses four set screws pushing outward to center and hold on the inside of the SS tube above the copper cell. The suspender ring has a center hole that was machined to just allow the bellows tube to pass. This hole also centers the probe since it is chamfered out about a 1/4" at roughly a 45° angle as shown in Fig. 3.18. Four smaller

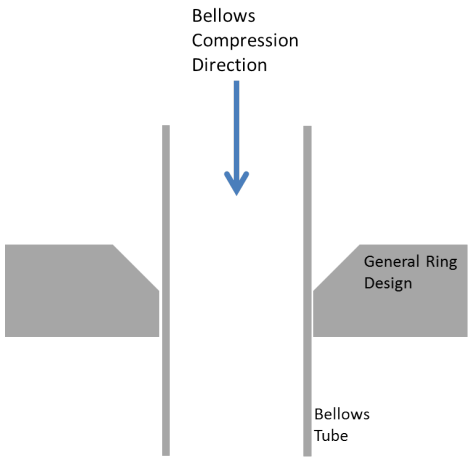


**Figure 3.18:** Conceptual diagram of the guide ring design. The three guide rings and suspension rings all have this chamfered geometry to guid the bellows and are present to force the probe and plates to be concentric. Not shown are the SS tubes that hold the rings up.

holes are arranged in a concentric pattern around the center hole of the suspender ring. Set screws tapped into the sides of these holes clamp SS suspension tubes that hang down into the cell. Along the tubes' length are three other rings machined to hold the suspension tubes and guide the bellows tube. At the end of the suspension tubes is a final SS ring that clamps to the tubes via set screws and also clamps four quartz rods via set screws. These quartz rods hold up the electrodes themselves inside the cell. Each ring also has two holes to allow the electrode wires to pass through and hold them out of the way of the bellows tube and probe. The quartz rods were shaped with a button on one end to hold the bottom plate up. Quartz spacing tubes are placed over the rods between each plate to hold them apart.

A schematic diagram of the electrode plates is shown in Fig. 3.19. The electrode plates themselves installed onto the suspension system are shown in Fig. 3.20. All of the electrode plates have

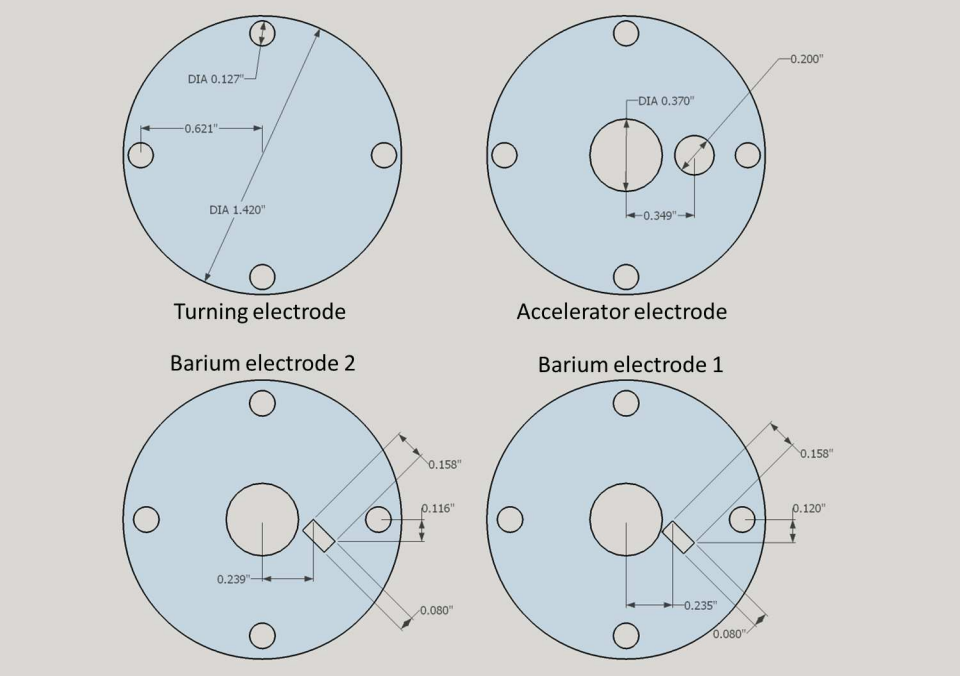


**Figure 3.19:** Schematic drawings of the electrode plates are shown with dimensions used to machine the plates. The plates are made from 1 mm thick SS. They are configured in a concentric stack held up by quartz rods and tubes. They are each soldered to a kapton insulated cable to be held at desired voltages.

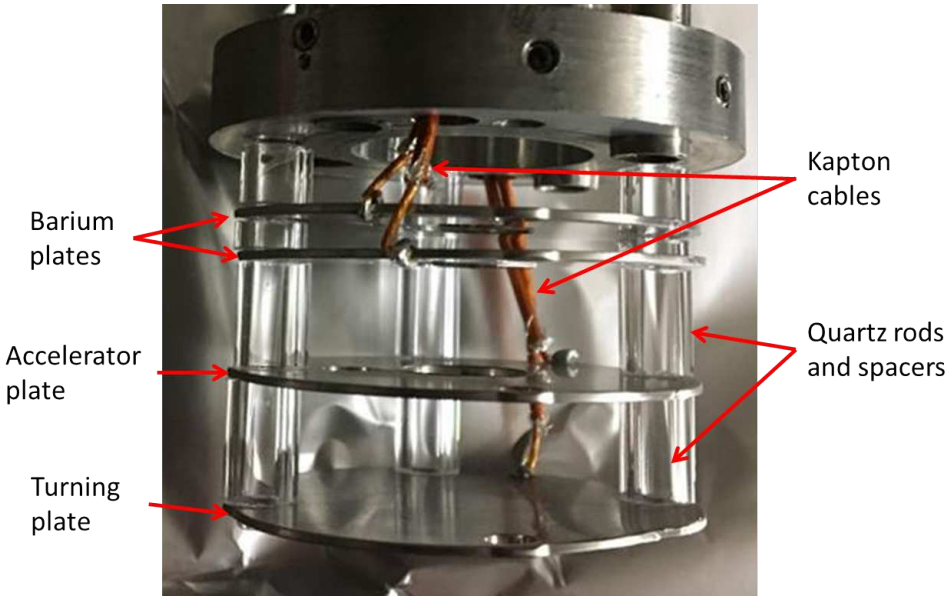


**Figure 3.20:** A photo of the ablation electrodes is shown. The SS plate holder ring is visible at the top. Set screws holding quartz rods and the SS suspension tubes are visible in the ring. The quartz spacing tubes are also visible around the rods themselves. The set of quartz rod and tubes at the front is removed to allow better optical access. The kapton cables soldered to each plate are visible as well. Because the photo was taken in atmosphere the barium sample could not be included.

four holes that the quartz rods pass through, and the top three have center holes to allow the probe to pass through. The electrode plates were constructed out of 1 mm thick SS sheets using a CNC mill. The electrical connections were made via Kapton insulated and coaxial shielded wires from Accu-Glass Products [52], which are soldered to each plate individually. The wires pass up through the plate suspension system as described above and are connected to the posts of CF feedthrough with 4 BNC connections.

A simple drawing of the ablation electrode system is shown in Fig. 3.14. The two top plates, referred to as the barium electrodes, hold up a barium sample at a downward angle. The barium electrodes were each machined with a rectangular notch in which the barium sample sits, as shown in Fig. 3.19. The barium electrodes are held apart by four 1 mm quartz spacers. The middle plate shown in Fig. 3.14 is referred to as the accelerator electrode, is 9 mm below the top two, and has a hole directly below the barium metal position, which allows the barium to pass through this plate. This plate's primary role is to accelerate the ions to the probe. The LXe level in the cell comes up to the level of this plate. The bottom plate, referred to as the the collector electrode, is a solid plate. This electrode turns the ions toward the probe when the probe is dipped in the LXe. It is also used to collect ions when the number of ions ablated per pulse is characterized as described below.

## 3.5 Ablation Ion Current Measurements

To measure the number of ions extracted from the plasma per ablation pulse, the electrode voltages were set in a configuration in which the current from the ions could be collected on the collector plate. The barium plates were set to 400 V, the accelerator plate was set to 200 V, and the collector plate was held at approximately 0 V by a Keithley 610C electometer operated in normal mode. The equivalent circuit of the electrometer is shown in Fig. 3.21. Using Kirchoff's laws one can write:

$$\begin{aligned} I &= I_1 + I_2 \\ V_1 &= -I_1 R_1 = -Q_2/C \end{aligned} \tag{3.2}$$

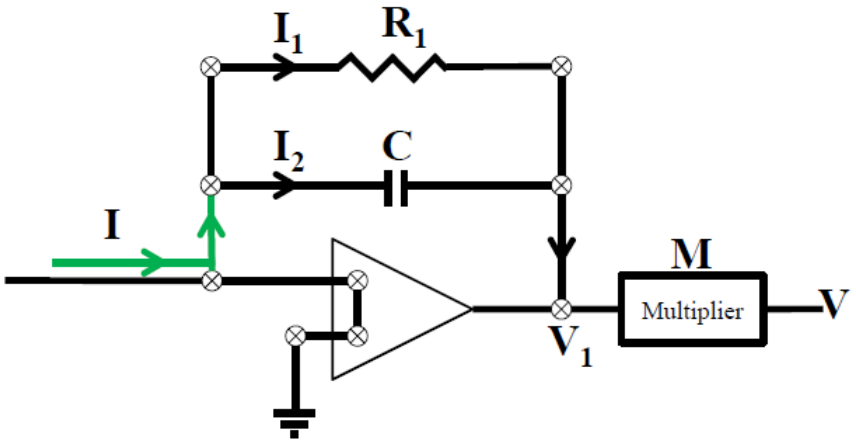


**Figure 3.21:** The equivalent circuit of the electrometer is shown. Current $I$ on the right of the figure is measured by analyzing the output voltage $V$ shown on left. Figure is reproduced from [45].

where $Q_2$ is the charge on the capacitor, $I$ is the input current to be measured by the electrometer, $I_1$ is the current through the resistor $R_1$. The final readout voltage is given by $V = MV_1$ where $M$ is a multiplication factor of the final amplifier. Combining these equations the input current can be written:

$$I(t) = A(V - V_{offset} + \tau \frac{dV}{dt}) \tag{3.3}$$

In this equation, $A \equiv -\frac{1}{R_1 M}$ and $\tau \equiv R_1 C$. There is an offset voltage $V_{offset}$ that can be adjusted on the electrometer.

The quantities $R_1$ and $M$ vary with electrometer setting and are measured by calibrating the electrometer. This calibration procedure involves creating a small current by sending a square wave voltage $V_s$ through a $R$ = 3 G$\Omega$ resistor into the electrometer and reading the voltage out. In this case, the input current in Eq. 3.3 is given by $I(t) = V_s(t)/R$. Solving the result for the electrometer output $V(t)$ gives the following:

$$V(t) = V(0) + \frac{V_s(t)}{RA}(1 - e^{-t/\tau}) \tag{3.4}$$

where $V(0)$ is an initial voltage that is equal to $V_{offset}$ in 3.3. This function is fit to the recorded V(t) and the fit result gives the calibration constants $A$ and $\tau$. An example result of this procedure

is shown in Fig. 3.22. The result of this calibration is $A$ = -5.9$\times 10^{-11}\Omega^{-1}$ and $\tau = 0.0088$ s.

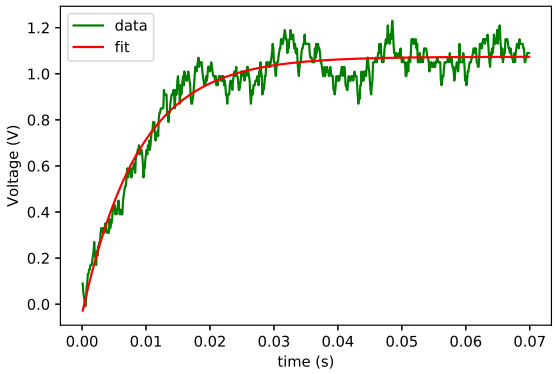


**Figure 3.22:** A fit to electrometer calibration data is shown. A square wave of amplitude 0.2 V was sent through a 3 G$\Omega$ resistor. The result of the fit is $A$ = 5.9$\times 10^{-11}\Omega^{-1}$ and $\tau = 0.0088$ s.

Plugging these values into Eq. 3.3 gives:

$$I(t) = -5.9 \times 10^{-11}(V + 0.0088\frac{dV}{dt}) \tag{3.5}$$

This equation is used to calculate the current signal from the output of the electrometer. The square wave current can be reproduced using this equation. In Fig. 3.23 the reproduced square wave is shown from the same run used for the calibration.

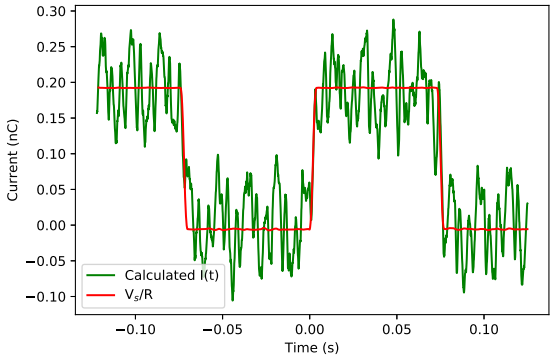


**Figure 3.23:** Calculated current from electrometer data and measured square wave voltage divided by resistance.

An example electrometer signal from ablation of barium is shown in Fig. 3.24. Processing this signal with Eq. 3.5 gives the current shown in Fig. 3.25. A fit with two Gaussian functions

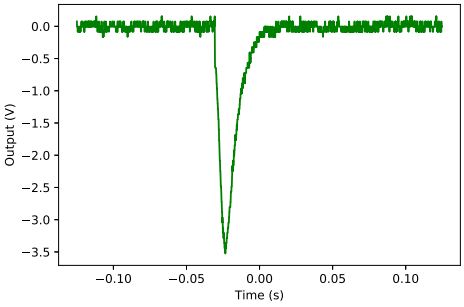


**Figure 3.24:** Raw electrometer output for an ablation run with roughly 1 mJ of pulse energy.

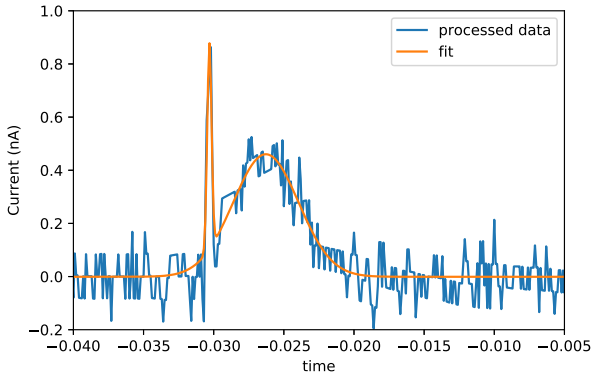


**Figure 3.25:** Input current for an ablation run with roughly 1 mJ of pulse energy. A fit with two Gaussians is applied to determine the number of ions collected.

is applied. The first fit peak is the induction signal from electrons generated by the photoelectric effect moving away from the collection plate. The broader second peak is the induction from the positive ions moving toward the plate. The result of integrating the Gaussian function fit to this peak gives 2.69 pC of charge collected from this ablation pulse. Dividing by the elementary charge gives $1.68 \times 10^7$ ions collected. While the numbers above are representative of a typical pulse, it was seen that there is on the order of a factor of 2 variance in the size of the electrometer signal between ablation pulses. There are also some xenon ions in this signal that cannot be separated

out. Results from past tests done in liquid xenon in which the barium and xenon ions move at very different speeds show that xenon ions do not contribute more than 10% to the correct signal [45,46]. Thus a conservative estimate of the $Ba^+$ charge produced is $\geq$1 pC/pulse.

## 3.6 Simulations of Barium Ion Deposition

Simulations were done using SIMION 8.0 [53] to determine the fraction of ions that are deposited on the window. The simulation was carried out by simulating a hollow sphere of ions representing the edge of the plasma near the ablation target and tracking their flight. To make the calculation run more quickly, a xenon pressure of 20 Torr was used, which is more than a factor of ten less than the pressure used during the experiments. In the absence of Coulomb repulsion, assuming the mean free path is small compared to the length of the trajectory, the pressure does not impact the path ions take, only the speed at which the ions travel along the electric field lines. Higher pressure may also have some impact on the spread of the ions due to Coulomb repulsion. Shown in Fig. 3.26 are 10000 barium trajectories simulated in a 20 Torr environment assuming Coulomb repulsion equivalent to 2 pC of ablated charge. It was found that a number of the ion

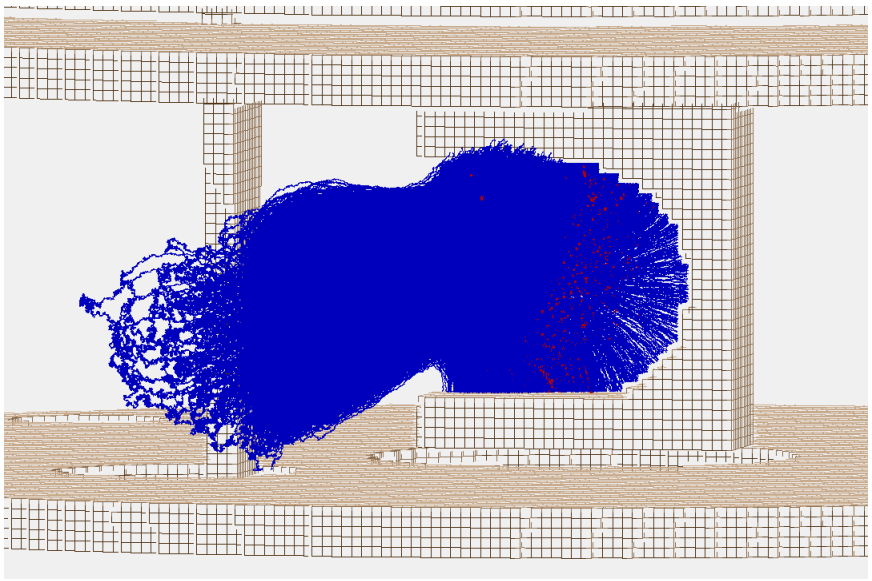

**Figure 3.26:** Flights of 10000 ions are shown with 300 V plate voltage, 20 Torr pressure, and Coulomb repulsion. The tracks travel toward the center of the window and then disperse toward the copper window holder.

paths cross the plane of the window. The final positions of the ions are shown in Fig. 3.27. The ions positions are colored according to (1) ions landing on the barium, (2) on the copper, or (3) on the window. In this simulation, about 18% of the ions landed on the window. To see if the possible change in the effect of Coulomb repulsion expected at higher pressures has a major effect on this outcome, 300 trajectories were simulated both at 200 and 700 Torr. There was a slight increase in the number of ions hitting the window in these cases.

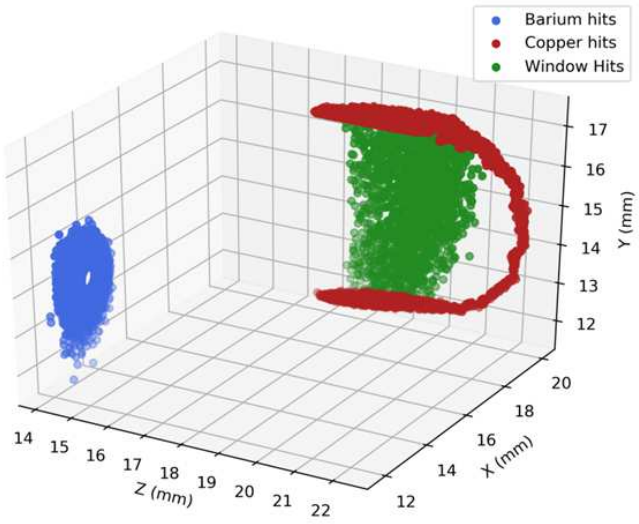


**Figure 3.27:** The positions of ion landings are shown color coded. It can be seen that a portion of the ions land on the window. They are distributed fairly uniformly through the center of the window in an approximate area of 4x4 mm$^2$.

When barium ions are captured in the solid xenon, a local charge density $\sigma$ could be built up on the surface. For a uniform layer of charge density $\sigma$, the electric field due to this charge is $E = \frac{\sigma}{\epsilon_o}$. Once this field is equal and opposite to the applied field, no more charge will land on the window. The minimum number of pulses required to create this balancing field can be estimated based on the simulated charge density per ablation pulse, which can be written:

$$\begin{aligned}\sigma = \frac{Q}{A} &= \frac{.176 \times 2\ \mathrm{pC/pulse}}{.16\ \mathrm{cm}^2} \\ &= 2.2 \frac{\mathrm{pC}}{\mathrm{cm}^2 \cdot \mathrm{pulse}}\end{aligned} \tag{3.6}$$

where $Q$ is the charge per pulse landing on the window and $A$ is the area over which the ions are distributed, which is found in the simulation to be 16 mm$^2$. The field due to a single pulse is therefore:

$$\begin{aligned}E &= \sigma/\epsilon_o \\ &= \frac{2.2 \times 10^{-8}\mathrm{C/m}^2}{8.85 \times 10^{-12}\ \frac{\mathrm{C}}{\mathrm{Vm}}} \\ &= 2.5\mathrm{V/m} = 25\mathrm{V/cm}\end{aligned} \tag{3.7}$$

Since the electric field near the surface without any ions deposited is on the order of 300 V/cm, the minimum number of pulses required to cancel this field out is about 12 and the maximum charge density is $12 \times 2.2\mathrm{pC/cm}^2 = 26\mathrm{pC/cm}^2$. This is an effective limit on the barium ion density that can be deposited on the window if there is no charge compensation. As the charge density on the window increases, the 18% deposition efficiency should decrease significantly. Thus more than 12 pulses are likely required to approach the maximum. In the experiments described in Sec. 4.3, the number of ablation pulses used was 750. Thus the density of ions deposited maybe near the maximum. This is uncertain because an unknown fraction of th ions that land on the window will neutralized over some period of time.

The rate at which neutral barium atoms accumulate on the window depends on (1) the number of neutral atoms that diffuse from the plasma and drift to the window and (2) the number of ions that land on the window and neutralize there. The neutrals are not affected by the charge density on the window so the number of diffusing neutrals will scale linearly with number of pulses. The number of neutralized ions may be some fraction of the number of ions arriving at the window.

## 3.7 Fluorescence and Absorption Optics

The optical system used for excitation and collection of fluorescence at the upper cell consists of two primary subsystems: optics used for the excitation of fluorescence and optics associated with collection of the fluorescence light. A diagram of the optical system is shown in Fig. 3.28. The excitation system consists of a dye laser, an optical fiber with couplers at both ends, two laser filters, two steering mirrors, and a focusing lens. The collection system consists of a collection lens, three steering mirrors, a Raman filter, a camera lens, a spectrometer, and a CCD camera.

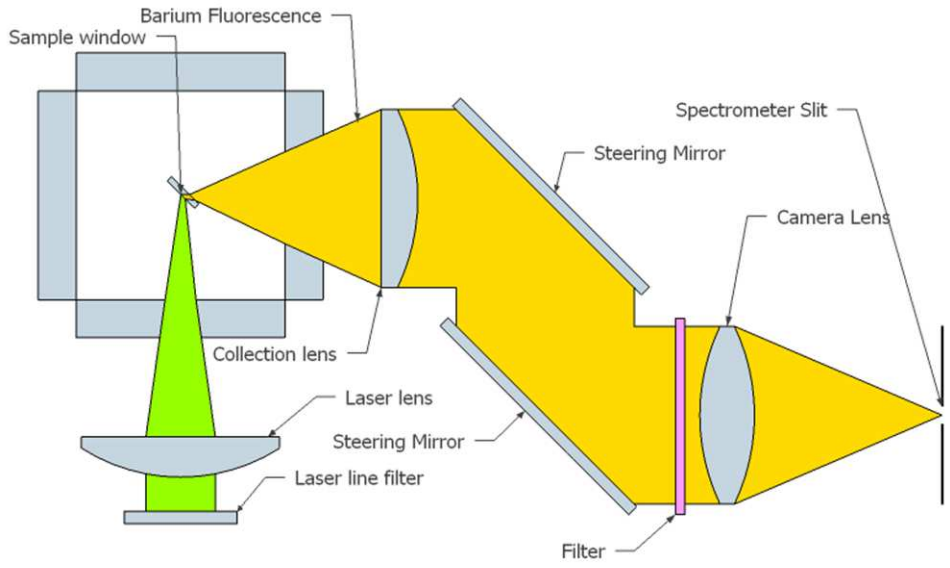


**Figure 3.28:** Diagram of the fluorescence excitation and collection setup from a top view. The spectrometer and CCD camera, which would be on the right, are not shown.

The excitation laser is a dye laser. It uses Rhodamine 6G dissolved in ethanol. This solution is pressurized through a nozzle to form a jet within the dye laser cavity. A 532 nm 2 W Coherent Verdi V8 pump laser is used to excite dye molecules in the jet [54]. These fluoresce at a range of wavelengths. There is a birefringent filter in the laser cavity at a roughly 45° degree angle to the beam propagation. The filter can be rotated to change the index of refraction, which causes most wavelengths to be partially reflected out of the cavity while the selected wavelength is passed with

high transmission to stimulate lasing. The rotation angle is tuned to specify the wavelength of the dye laser, which in practice spans approximately 560-590 nm.

The laser beam, as it exits the dye laser, is filtered by a laser line filter to remove spontaneous emission, which is non-laser light that comes from the dye laser. This spontaneous emission light could make it to the window and contribute background photons at the wavelengths of interest in this work. Once the laser is filtered, it is coupled into a nearly single mode 6 $\mu$m diameter optical fiber that transmits the beam across the lab. The beam exits the fiber and passes through 1 cm focal length lens. This lens is used to collimate and slightly expand the beam beyond this point. The beam is then deflected by the two steering mirrors. It passes through another laser line filter to remove Raman scattering light resulting from traversing the fiber. Finally, the beam is incident onto a 10 cm focal length lens. At this point the beam is about 1 cm in diameter. The position of the lens is adjusted such that the beam waist is on the barium sample window. The beam waist radius was measured at various longitudinal positions by inserting a mirror after the focusing lens and scanning a razor blade transversely across the beam and measuring the transmitted power. The data at each position was fit to an error function. The waist radius at the focus was w = 32 $\mu$m.

Fluorescence is collected at a right angle to the excitation beam. First the fluorescence light is collected and collimated by a 10 cm plano-convex lens. It is then rotated 90° and steered by three mirrors into a 50 mm Nikkor camera lens mounted on the front of the Acton SP-2150i imaging spectrometer. As the collimated fluorescence light passes into the camera lens it passes through a filter that blocks scattered laser light. The filter used in this work is either a 570 nm long pass or 610 nm long pass filter. The filters are fitted with a dark plastic shield that covers the whole lens. As a result virtually no light gets into the camera lens without passing through the filter. The lens images the light onto an input slit on the spectrometer. The light then reflects off of a diffraction grating and is focused onto the nitrogen-cooled CCD chip of a Roper-Scientific camera [55]. The camera and spectrometer are operated in tandem using WinSpec32 software. An example zero-order image of the window with the laser passing through it is shown in Fig. 3.29, which shows a vertical line of $Cr^{3+}$ emission excited by the laser as it transmits through the sapphire window. At

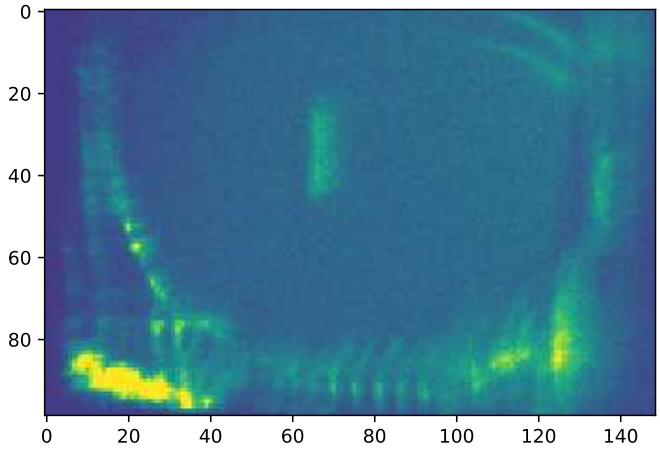


**Figure 3.29:** Example image of the laser beam traversing the window. This image was taken with the spectrometer in 0th-order mode with the slit completely open, and a 568 nm long-pass filter in. The laser wavelength was 565 nm in this image. The laser is traversing the window vertically from bottom to top in the center of the image. Barium ablation occurs on the side of the window that is at the bottom of the image. The light collected in the center of the image is primarily 693 nm $Cr^{3+}$ fluorescence from the interior of the sapphire window.

the ends of each line emission from the two surfaces of the window can be seen. The spot on the bottom is where fluorescence from barium atoms deposited is expected. The line is vertical due to the rotation of the image. In real space, the laser is moving left to right from the perspective of the collection lens.

## 3.8 Apparatus for Barium Lifetime Measurements

Measurements of the fluorescence lifetime for the 620 nm transition in barium were also carried out. In order to do this measurement, a technique known as Time-Correlated Single-Photon Counting (TCSPC) was used. The TCSPC system was composed of a pulsed 561 nm laser, a single photon avalanche diode (SPAD), and a time tagging electronics module. This measurement made use of the ion beam, cryostat, and xenon deposition system described in [28, 56]. The ion beam is mass selected and can deposit varying numbers of barium ion pulses onto a window on which a layer of SXe is growing [27]. More detail regarding the ion beam and the general deposition procedure can be found in [28].

The laser used for the lifetime measurement was a 561 nm diode laser furnished as demonstration equipment from PicoQuant Photonics Incorporated [57]. The laser controlled by a PDL-800 laser controller. The laser puts out 40 ps pulses at up to 80 MHz rep rate. The rep rate can be adjusted down to as low as 5 MHz. The laser controller also puts out a precise timing TTL signal at 10 MHz, simultaneous to the laser pulses. The laser is focused onto the sample window, which is tilted at a 45° angle. The laser pulses excite 619 nm fluorescence of the barium atoms in single-vacancy sites in the SXe matrix deposited on the window. This fluorescence is collected and collimated by a camera lens, passed through a 620 nm bandpass filter, and imaged down onto the SPAD. The SPAD is also a PicoQuant demo unit. It has a detector diameter of 20 $\mu$m and quantum efficiency of approximately 40%.

The timing signal is fed to a time tagging electronics module. This module is a PicoHarp 300 (PH), which was also from PicoQuant. The PH accepts a timing signal from the laser indicating that the laser pulse has occurred and starts a frame. The PH then waits for a photon signal from the SPAD. The SPAD output signal is a TTL pulse read by the PH and has 50 ps timing resolution. When a photon signal arrives from the SPAD the time difference from the initial timing pulse is recorded. In this way, a histogram of photon arrival times is created over the course of many laser pulses. The PH is connected to a PC via USB and interfaces with a data acquisition program.

# Chapter 4

# Barium Tagging Results

In this chapter, results of a variety of tests and experiments pertaining to barium tagging in SXe on a cryoprobe are described. Discussion of results for growth of the SXe ball on a JT probe is given in Sec. 4.1. Results of the tests of raising and lowering the probe using the bellows are presented in Sec. 4.2. Initial observations of the fluorescence from SXe samples on the sapphire window with and without barium deposited are discussed in Sec. 4.3. Results of measurements of the barium fluorescence lifetime are discussed in Sec. 4.4.

## 4.1 Studies of SXe Sample Growth

Several implementations of a Galil Medical JT probe have been used to freeze xenon. It has been shown to freeze SXe at a variety of LXe temperatures. Early tests were done in such a way that a video camera recorded the growth of the SXe probe over time. The size of the sample was then measured from frames of the video with the diameter of the probe itself used as a calibration distance. An example of a still frame used for this procedure is in Fig. 3.2. The measurements were made horizontally at the widest point of the cylinder. Some of the measurements on the frames were done using a simple homemade image processing algorithm. Growth results for several different LXe temperatures at an argon pressure of 1000 PSI are shown in Fig. 4.1. The SXe sample grows more quickly and grows to a larger size when the temperature of the liquid is lower. Other measurements were made with 1300 PSI of argon pressure through the initial probe design with no vacuum jacket. The data are shown in Fig. 4.2. In this plot, it is clear that there is a faster rise at first and then a flat equilibrium size being reached. This data has been fit with a thermal model described below.

The thermal model of the growth of solid xenon on the cryoprobe assumes a precooling level and heat flow through layers of different material as shown in Fig. 4.3. Each layer has a thermal resistance according to its thickness and thermal conductivity. The potential for heat to flow is dic-

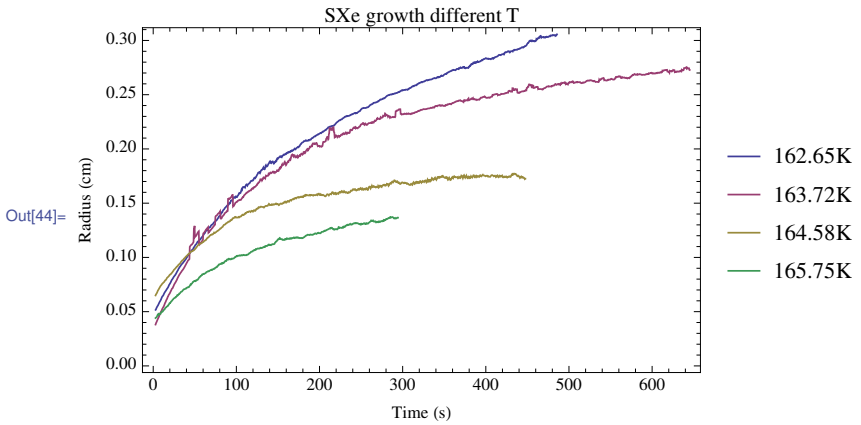


**Figure 4.1:** SXe sample radius versus time curves at different xenon temperatures. These curves were captured by an image processing algorithm applied to successive frames of video of the SXe growing.

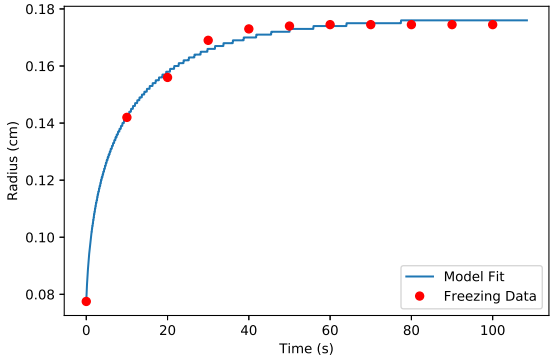


**Figure 4.2:** Red data points show measured radius of a SXe cylinder versus time for 1300 PSI argon pressure. A theoretical model fit to the data is shown in blue.

tated by the difference in temperature across the system from the LXe to the cold argon. Assuming a cylindrical geometry, the mass growth rate, $\frac{dm}{dt}$, of the SXe cylinder can be written:

$$L\frac{dm}{dt} = \frac{dQ_s}{dt} - \frac{dQ_l}{dt} \tag{4.1}$$

where $L$ is the latent heat of fusion for SXe, $\frac{dQ_s}{dt}$ is the heat flow through the solid, and $\frac{dQ_l}{dt}$ is the heat flow from through liquid. The heat flow through the liquid can be written:

$$\frac{dQ_l}{dt} = 2\pi k_{LXe} l \ln\left(\frac{r_l + r}{r}\right)(T_l - T_{sol}) \tag{4.2}$$

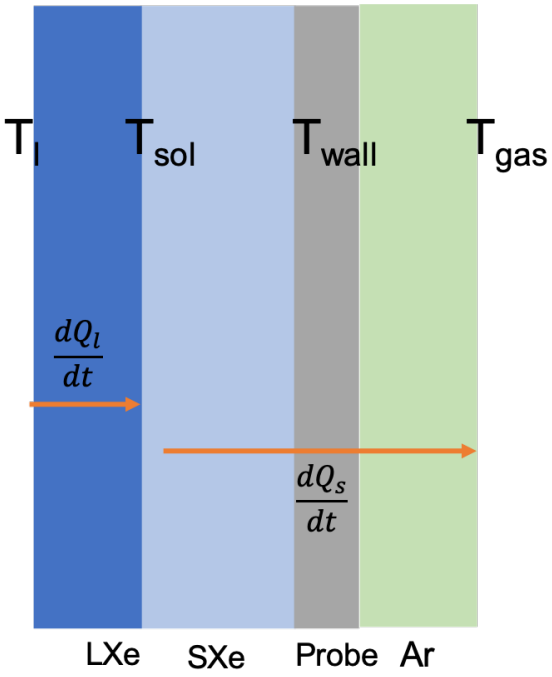


**Figure 4.3:** A diagram of the modeled heat flow and ball growth. The model takes into account heat flow through the layers shown but in a cylindrical geometry.

where $k_{LXe}$ is the thermal conductivity of liquid xenon, $l$ is the length of the SXe cylinder ,$r_l$ is a radial distance over which the heat is conducted through the LXe, $r$ is the radius of the SXe sample, $T_l$ is the liquid temperature (165K in this case), and $T_{sol}$ is the temperature of the solid surface (161K). The heat flow through the solid can be written:

$$\frac{dQ_s}{dt} = 2\pi l k_{SXe} \ln\left(\frac{r}{r_0}\right)(T_{sol} - T_{wall}) \tag{4.3}$$

where $k_{SXe}$ is thermal conductivity of solid xenon, $r_0$ is the radius of the probe, and $T_{wall}$ is the temperature of the SS probe wall. The heat flow through the wall to the gas can be written ignoring the temperature drop across the wall:

$$\frac{dQ_s}{dt} = \pi N u l k_{Ar}(T_{wall} - T_{gas}) \tag{4.4}$$

where $Nu$ is the Nusselt number used to relate conductive to convective heat transfer through gas, $k_{Ar}$ is the thermal conductivity of argon, and $T_{gas}$ is the temperature of the argon as it exits the JT

nozzle. This temperature is given by:

$$\Delta T_{gas} = T_{gas} - T_{pre} = -\mu_{JT} P \tag{4.5}$$

where $T_{gas}$ is the temperature of the argon gas after leaving the JT nozzle, $T_{pre}$ is the temperature of the gas before is enters the nozzle, $P$ is the argon input pressure, and $\mu_{JT}$ is the Joule-Thomson coefficient for argon at the LXe temperature. The heat flow through the solid can be thought of as a current flowing through thermal resistors in series. The total potential drop across the thermal resistors is the temperature drop $T_{sol} - T_{gas}$. Solving these equations under this scenario, including the assumption that the resistance of the wall is negligible, the heat flow through the solid can be written:

$$\frac{dQ_s}{dt} = \frac{T_{sol} - T_{gas}}{R} \tag{4.6}$$

where $R$ is the total thermal resistance mentioned above and is:

$$R = \frac{1}{2\pi k_{SXe} \ln\left(\frac{r}{r_0}\right)} + \frac{1}{\pi l N u l k_{Ar}} \tag{4.7}$$

These equations can be solved numerically for $r(t)$ with $m(t) = \pi \rho_{sol}(r^2(t) - r_0^2))l$ where $\rho_{sol}$ is the density of solid xenon. The precooling value, $T_{pre}$, and the characteristic radius of liquid cooling, $r_l$, are adjusted to fit the model to data. The best fit values for the data in 4.2 are $T_{pre}$ = 198.3 K and $r_l$ = 0.653 mm. The model could also be adapted for different sources of cooling rather than cold argon. It could be used in the future to establish a procedure to maintain the SXe thickness at a constant value.

The model can also be used to qualitatively understand the data in Fig. 4.1. The heat flow through the liquid, $\frac{dQ_l}{dt}$, is larger at higher LXe temperatures, $T_l$. Thus, by Eq. 4.1, the solid growth term $L\frac{dm}{dt}$ will be smaller for the same amount of heat flow to the gas, $\frac{dQ_s}{dt}$. So, the larger growth at lower liquid xenon temperatures can be explained by the model.

## 4.2 Pressure Measurements

In order to optimally preserve the SXe sample on the cryoprobe during the transit from the LXe cell to the upper cell it is necessary to understand the pressure behavior of the liquid/gas system as the probe is being lifted. To that end measurements of the gas pressure above the LXe reservoir in the copper cell were carried out during multiple cycles of expanding and compressing the bellows. Pressure data over time during 20 raising and lowering cycles is shown in Fig. 4.4. The stroke length of the bellows is varied from 1 million steps of the motor for the first 4 cycles to 6 million steps for the last 4 cycles. The length of compression or expansion associated with 1 million steps is 3.125". One notable aspect of this data is that the pressure goes to a quasi-static equilibrium value that depends on whether the bellows has just been compressed or expanded. There is an initial overshoot of the this quasi-static equilibrium pressure then a rapid decay to it.

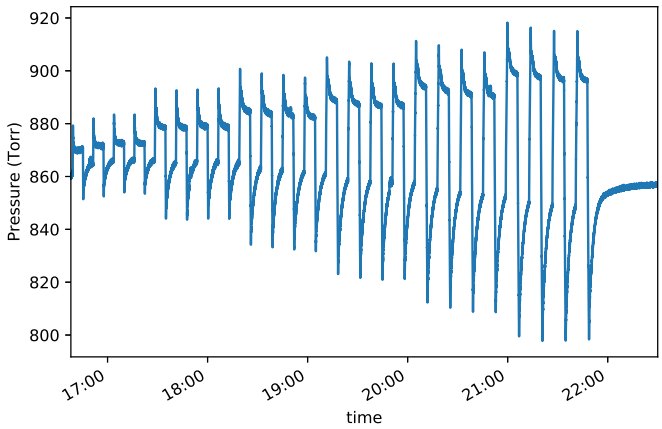


**Figure 4.4:** Pressure as a function of time for twenty raising and lowering cycles over a period of five hours.

Pressure variation with time during one cycle of expansion and compression of the bellows is shown in Fig. 4.5. This cycle was carried out with liquid in the cell and the cell temperature was 165 K. The distance traveled is $6\times10^6$ steps or 18.75" at 20 rev/s or 1.25 in/s. There are two different quasi-static equilibrium pressures in this plot. One is around 845 Torr and the other is near 780 Torr. Both the compression and expansion are characterized by a rapid rise or fall in pressure during transit, then the pressure recovers somewhat to a quasi-static equilibrium that is

different for compression and expansion. Compressions result in a much swifter recovery than expansions. Larger compressions and expansions result in a larger offset between the quasi-static equilibria. The different quasi-static equilibrium pressure after expansion and compression may be an indication of a change in the surface temperature of the LXe

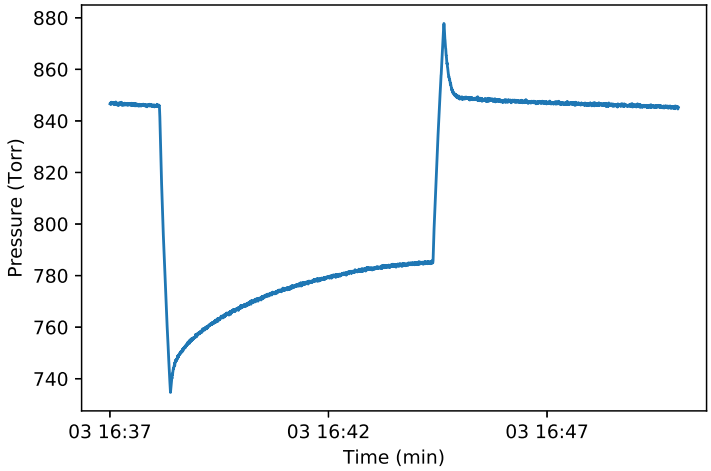


**Figure 4.5:** Pressure vs. time for a single expansion and compression cycle of the bellows is shown. The distance traveled corresponds to $6\times10^6$ steps and the speed was 20 rev/s.

The measured pressure during the bellows expansion is shown by blue dots in Fig. 4.6 on an expanded time scale. An adiabatic expansion model has been applied to this situation. The differential equation that describes this expansion is:

$$\frac{dP}{dt} = -\frac{\gamma P}{V(t)}\frac{dV}{dt} \tag{4.8}$$

where P is the xenon pressure, $\gamma = 5/3$ is the adiabatic constant for xenon gas. The xenon gas volume $V(t)$ increases quadratically over the first 1.33 s of the expansion as the motor accelerates at a constant rate to its maximum speed. The steady state value of $\frac{dV}{dt}$ after the acceleration is .0256 l/s. This model is represented in orange in Fig. 4.6. The adiabatic model agrees with data for the first few seconds but then predicts too large a pressure drop at later times.

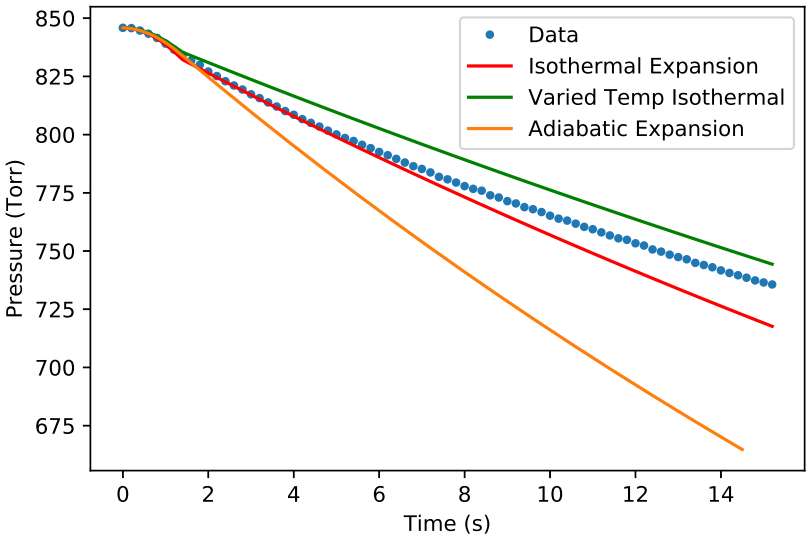


**Figure 4.6:** Bellows expansion data is compared with an adiabatic (orange) and an isothermal expansion model (red). Another model (green) is shown that assumes regions of the gas are at different temperatures.

The pressure behavior during the bellows expansion may also be modeled as an isothermal expansion if the heat exchange between the walls and the cold gas takes place quickly on the time scale of the expansion. The pressure according to this model can be written as:

$$P(t) = P_i \frac{V_i}{V(t)} \tag{4.9}$$

where $P_i$ is the initial pressure, $V_i$ is the initial volume, and $V(t)$ is the volume as a function of time. This model, shown in red, is compared to the expansion data in Fig. 4.6. At early times, this model does not fit the data rquite as well as the adiabatic model. At intermediate times this model fits the data well. At later times the predicted pressure drop is a little greater than that observed.

Some of the gas in the xenon volume is at room temperature (e.g., gas inside the bellows) while some of the gas will be at lower temperatures (e.g., gas in the cell at $\sim$165 K). A modified isothermal expansion model accounting for three regions at different temperatures is given by:

$$P(t) = P_i \frac{\frac{V_{cell}}{T_{cell}} + \frac{V_{tube}}{T_{tube}} + \frac{V_{plumbing}}{T_{room}} + \frac{V_{bellows}}{T_{room}}}{\frac{V_{cell}}{T_{cell}} + \frac{V_{tube}}{T_{tube}} + \frac{V_{plumbing}}{T_{room}} + \frac{V_b(t)}{T_{room}}} \tag{4.10}$$

where each volume at a given temperature is included separately and divided by its temperature. The values of the parameters in this equation are given in table 4.1. This model predicts a somewhat slower drop in pressure as shown in Fig. 4.6. It matches the data best at the end of the expansion period.

**Table 4.1:** Values used in Eq. 4.10 for the various parameters.

| | T(K) | V(l) |
|---|---|---|
| Cell | 165 | 0.49 |
| Tube | 230 | 0.77 |
| Plumbing | 295 | 0.70 |
| Bellows | 295 | Variable (0.29 - 0.67) |

## 4.3 Initial Barium Fluorescence Measurements

Tests were carried out in an effort to observe laser induced fluorescence from barium atoms captured in SXe while freezing from gaseous xenon. Each xenon deposit began by applying a low pressure of argon to flush the probe while the probe remained in the upper cell. After about 30 s of low flow the argon was turned up to 1900 Torr, which causes enough cooling to freeze xenon. Once this flow was established the probe was lowered into the LXe cell to the position shown in figures 3.14 and 3.15. In this case the cell contained xenon gas at room temperature and 400 Torr of pressure. In the cell, the window was observed visually until freezing was seen. At this point either the ablation was triggered in the case of barium deposits or a time delay of 30 s was allowed for a xenon-only deposit. Then, the probe was lifted to the upper cell and exposed to the laser as fluorescence light was collected through the spectrometer.

The first spectra of xenon and barium deposits from GXe using the JT probe and sapphire window were taken. In this experiment, a series of xenon and barium deposits were excited and their fluorescence measured. Stable and consistent conditions were achieved on deposits and exposures associated with runs designated 41, 42, and 43. During these runs first order images of the floures-cence were collected, with the grating set such that 600 nm light is deflected by the diffraction

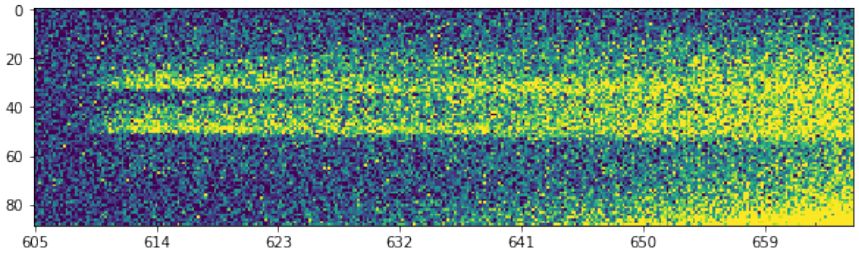


**Figure 4.7:** Example first order image of a barium run (43). This is the first 20s exposure. The x-axis is wavelength in nanometers. The y-axis is pixel number.

grating into the center of the CCD. The excitation wavelength used was 570 nm. The power of the excitation beam was on the order of 26 $\mu$W, and it was focused to a waist radius of w = 32 $\mu$m at the window. An example of a first order image of run 43 is shown in Fig. 4.7. This image shows the way the fluorescence spots in the zero-order image shown in Fig. 3.29 are spread out by the spectrometer. In this first order image, the barium ions, as simulated, are expected to land on the lower window surface in the image. The sharp lines in the first order image are the fluorescence from near the window surfaces spread out by the spectrometer. There is some blurring that gets much worse at higher wavelengths. There is also some scatter from copper that can be seen on the top and bottom right of the image. This scatter also appears to overlap the surface fluorescence at wavelengths above 650 nm. The cut-off below 610 nm due to the Raman filter can be seen as well.

The first good xenon-only deposit (41) was two 20 s laser exposures. This deposit was done after a separate Ba deposit (40) that had poorer optical focusing. After the xenon run was carried out two barium deposits (42 and 43) were done with 30 s of ablation pulses at 25 Hz repetition rate or 750 pulses and an estimated 2 pC of ions ablated/pulse. Two laser exposures of 20 s each were taken of these two deposits with a 10 s readout time between. During the readout time the laser was not illuminating the sample. For all the runs including the xenon run, the first order images were binned in the vertical dimension into 9 pixel bins such that horizontal strips comprising the top surface, the bulk, and the bottom surface are summed together creating three separate spectra. The spectra are then smoothed in x by taking a 10 bin rolling average. These spectra for both frames of all three runs are shown in figures 4.8, 4.9, and 4.10. In all three spectra, there is an increasing

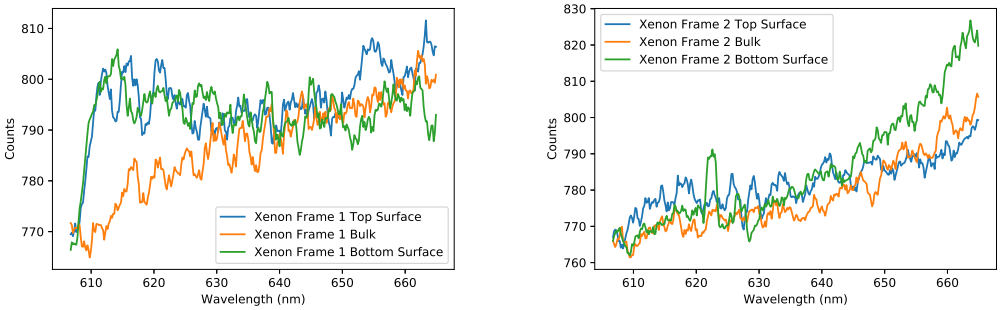


**Figure 4.8:** First and second 20 s frames of the xenon deposit (41). The top surface, bulk, and bottom surface have been separately integrated.

signal from low to high wavelengths that is present in the spectra of the bulk as well as the two surfaces. This is similar to copper fluorescence scatter visible at the bottom right of Fig. 4.7 and may largely be due to such a component.

There is some evidence in these spectra that barium fluorescence may be present. An excess of light on the top and bottom surfaces is seen in all three spectra in the range 610-630 nm. This range is coincident with the 619 nm barium fluorescence band in SXe used for imaging in [27]. For all runs, signal loss between frames can be seen in the wavelength region 610-630 nm. This loss of signal after exposure is consistent with bleaching of neutral barium atoms. The fact that this diminishing peak is present in the xenon run and on the back (top surface in the image) of the window may suggest that a significant number of barium atoms from previous ablations are captured from the gas. There was around 45 min of real time elapsed between ablations from run 40 and the start of run 41. The excess of light from the front surface of the window (bottom surface in the image) in the first barium run (42) is possibly significant. This may be due to an excess of barium ions there that neutralized. This excess is not seen in the second barium run (43).

It is interesting that some barium fluorescence may have been observed at near 160 K. Previous studies at 11-38 K have shown an order of magnitude decrease in 619 nm fluorescence from 11 K to 38 K [24, 56]. Window surface background should also be considered as a possible explanation for this signal as it too can be bleached with laser exposure. However, in the lower temperature experiments, the surface background is lower in the 620 nm region than at higher wavelengths [56].

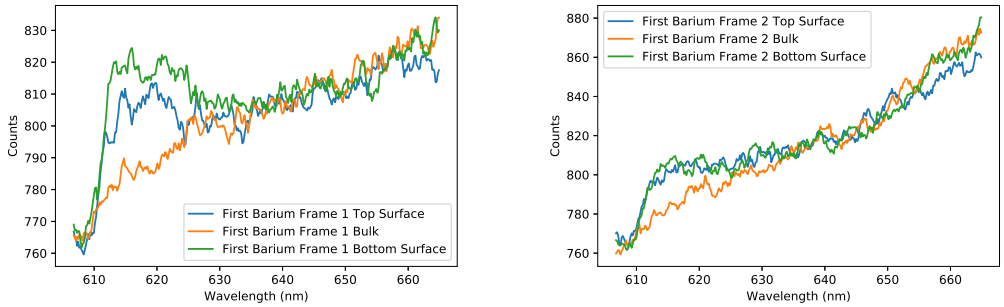


**Figure 4.9:** First and second 20 s frames of the first barium deposit (42). The top surface, bulk, and bottom surface have been separately integrated.

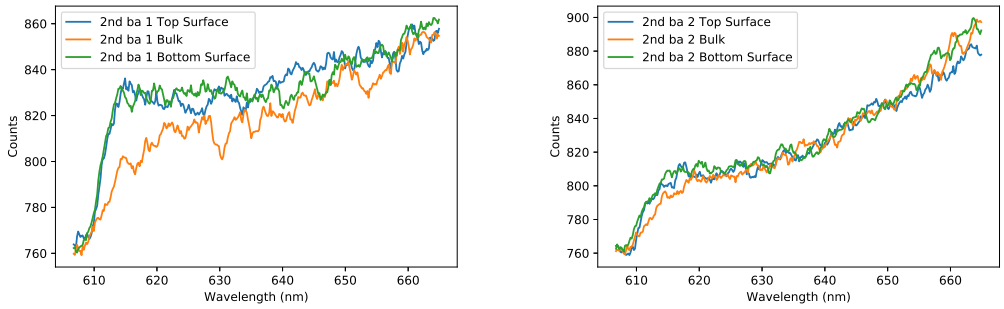


**Figure 4.10:** First and second 20 s frames of the second barium deposit exposure (43). The top surface, bulk, and bottom surface have been separately integrated.

Further investigation of this potential barium peak should ensure that xenon runs are done before any ablation has been done. This would reduce the possibility that neutral barium exists in the xenon gas. Another possibility is to look for the barium ion transitions reported in [24]. If barium ions are able to give sufficient signal when excited at this temperature, their green fluorescence peaks should be in excess only in the bottom spot and when ablation is done during the deposit because $Ba^+$ ions are rapidly drawn out of the xenon gas by the applied electric field.

## 4.4 Barium Fluorescence Lifetime Measurements

Barium fluorescence lifetime measurements were performed using the ion beam and the TCSPC system described in Sec. 3.8. The 619 nm fluorescence decay of large numbers of barium atoms excited at 561 nm is shown in Fig. 4.11. The fluorescence signal decay of an ensemble of excited atoms with a single decay path follows an exponential decay in time. The raw fluorescence observed in Fig. 4.11 is not perfectly represented by a single exponential because there is a small background component with a different lifetime. Thus the slope of the data in log(counts) is not completely constant.

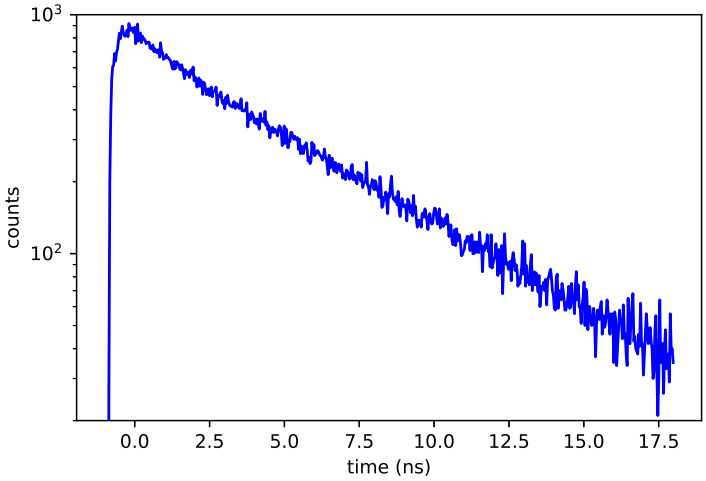


**Figure 4.11:** Fluorescence counts as a function of time. This example shows the exponential decay of fluorescence of barium atoms at 619 nm. This is data from a large deposit of barium ions.

The fluorescence signal of four runs taken in succession after a xenon-only deposit is shown in Fig. 4.12 in the top panel. The overlap shows that the lifetime of the background is repeatable. The second plot shows the average of runs for a later xenon-only deposit. This shows that the background is consistent for different deposits. In Fig. 4.13 the same data as in the bottom panel of Fig. 4.12 is shown on a log scale with an single exponential plus a constant fit to it. The best fit lifetime is 2.2±.06 ns. At long times the fit disagrees with data. This shows that the xenon-only fluorescence is not well described by a single exponential and a constant. This data also shows that there is little variation between deposits.

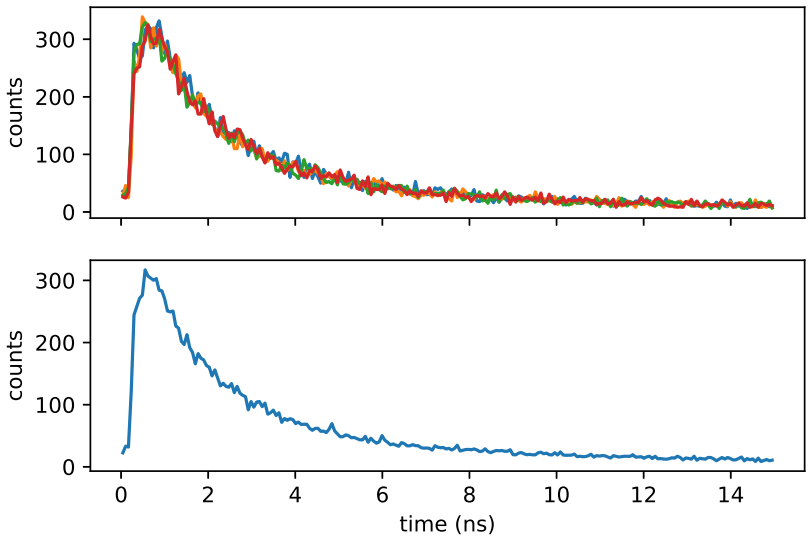


**Figure 4.12:** Top: The histograms of fluorescence at 620 nm of four 2 minute exposures from different xenon-only deposits are shown plotted together. All of the exposures are after a xenon-only deposit. A power setting of 10 and a repetition rate of 10 GHz is used in all exposures. Bottom: Average of the four exposures.

The barium fluorescence lifetime is determined by subtracting xenon-only data from data for large barium deposits with the same exposure time and laser power. The result for one measurement is presented in Fig. 4.14. The curve is linear on a log scale, and the good fit indicates that the barium fluorescence at 619 nm is well characterized by a single exponential with a fit lifetime of 7.0±.06 ns, where the uncertainty is only that associated with the fit.

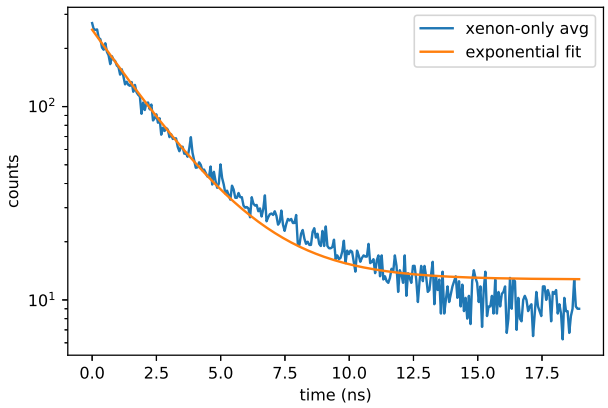


**Figure 4.13:** Data from bottom panel of Fig. 4.12 shown on a log scale with a single exponential plus a constant fit.

A single barium deposit of 5000 ion beam pulses was used to do 50 successive lifetime measurements. These were carried out while the laser was being scanned transversely in x and y in 10 $\mu$m steps within a region that had been bleached to reduce the surface fluorescence background. As a result, there are a large number of runs in the center of the bleached region with good differentiation between barium and background. At the edges of the bleached region, where the background is higher, the barium signal was less clear. To determine the barium fluorescence lifetime a fit function with barium signal and a background component was used with varying amplitudes for each:

$$f(t) = a \times Bkg(t) + be^{-t/\tau} \tag{4.11}$$

where a, b, and $\tau$ are fit parameters and $Bkg(t)$ is a linear interpolation of the average xenon background shown in the bottom of Fig. 4.12. A summary of barium lifetimes measured in the runs near the center of the bleached region is shown in Fig. 4.15. Each fitted lifetime is plotted versus run number with associated fit uncertainty. The average of the barium lifetime resulting from the dual component fit to each run is 7.0$\pm$.03 ns.

An additional source of background fluorescence that is of interest is due to stray light illuminating the cryoprobe used in the LXe system. For this measurement the pulsed 561 nm laser was focused onto the probe and the fluorescence was collected and focused into the detector through a

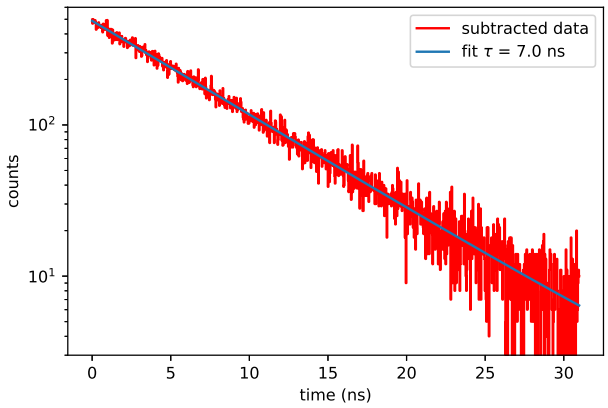


**Figure 4.14:** Fluorescence counts versus time for a 10 minute exposure of a barium deposit with a xenon exposure of the same experimental settings subtracted. The data is fit with a single exponential with a fit lifetime of 7.0 ns.

610 nm long-pass filter. The results of a 2 min exposure with full laser power are shown in Fig. 4.16. The decay is not exponential, which indicates that the fluorescence due to the band structure of the metal is not well described by a single decay. In Fig. 4.17, three representative datasets are plotted for each of the primary measurements reported in this section. The fluorescence of the metal and the xenon only deposits are clearly shorter lived than that of barium at 619 nm.

The possibility of using the difference in lifetime between the barium fluorescence and background to improve the signal to background ratio was investigated. Gating the fluorescence signal such that longer lived transitions contribute more signal is tested by simply discarding counts before a certain time in a normalized dataset then integrating the remaining signal. The fractional change is given by $1 - \frac{BkgIntegral}{BaIntegral}$. The fractional improvement to the signal to background ratio is shown in Fig. 4.18 for both the window surface background and the probe fluorescence. Also shown is the fraction of the total barium signal that is discarded in this procedure. For the case of the window surface background, the signal to background is strong enough in single barium images [27] such that this procedure may not be advantageous given the amount of barium signal that is discarded in order to achieve significant improvement. However, in the case of the probe fluorescence, a roughly 40% improvement can be achieved by discarding only 25% of the barium

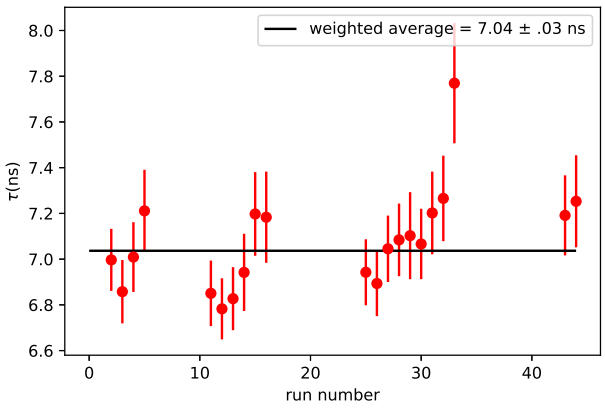


**Figure 4.15:** Barium lifetime measurements from 21 runs with 2 min laser exposures in different positions on one 5000 pulse deposit. The barium lifetime and fit uncertainty is shown for each. The weighted average of the data is plotted. The gaps in between runs are runs near the edge of the bleached region in which the fit performed poorly.

signal. Thus, use of a pulsed laser and TCSPC system may be desirable in the event that probe metal fluorescence is competing significantly with the barium signal.

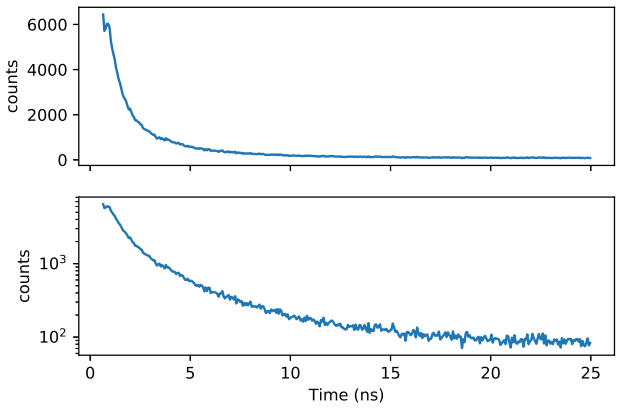


**Figure 4.16:** Fluoresence counts versus time with the 561 nm pulsed laser exciting the metal cryoprobe. The exposure was two minutes with maximum laser power and 10 GHz rep rate.

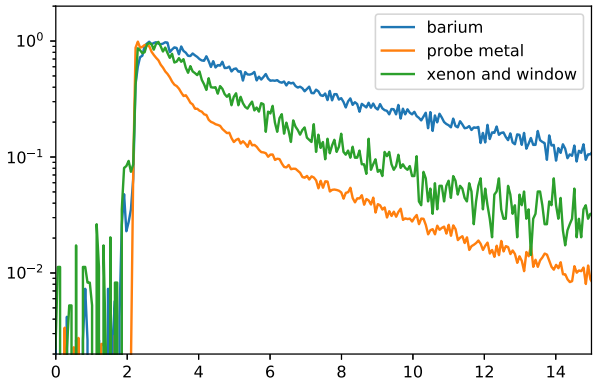


**Figure 4.17:** Fluorescence counts versus time are shown for a barium deposit, a xenon-only deposit, and the cryoprobe. This shows that both background signals decay faster than barium fluorescence.

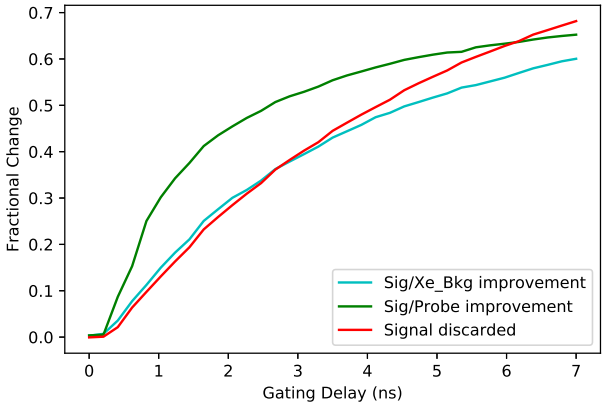


**Figure 4.18:** Signal to background ratio fractional improvement and the fraction of barium signal discarded due to gating for the xenon-only window surface background and probe background. The gating delay is the timed from just before the peak signal.

# Chapter 5

# Conclusions and Outlook

The efforts described in this work were in pursuit of two distinct goals. One was to observe or constrain the lifetime of nucleon decay of $^{136}$Xe to $^{133}$Sb or $^{133}$Te. This effort tested the principle of baryon number conservation. The other objective of this work was to develop a method to observe barium fluorescence from barium ions and/or atoms extracted from LXe in a SXe matrix. The purpose of this barium tagging concept is to increase the sensitivity of a next generation neutrinoless double beta decay experiment.

The search for nucleon decay of $^{136}$Xe to $^{133}$Sb or $^{133}$Te was done by searching for $\beta$ decays of the daughter nuclei $^{133}$Sb or $^{133}$Te. An important consideration was to understand the likelihood that the daughters are ionized versus neutral after the initial nucleon decay. Once this daughter ion fraction was modeled, it was used to create a model of the daughter decay locations and by extension the shape of the energy spectra for the daughter decays. To look for evidence of nucleon decay, a component with this energy spectrum was searched for in the EXO-200 low-background data. After careful consideration of the systematic uncertainties associated with this search, no evidence of nucleon decay of $^{136}$Xe to $^{133}$Sb or $^{133}$Te was observed, and new best limits were set on these decays. The limits exceeded former values by a factor of 9 for decay to $^{133}$Sb and 7 for decay to $^{133}$Te.

Some first spectra were taken of SXe deposits, with and without ablation of barium, on a sapphire window at the end of Joule-Thomson probe. These spectra show an excess of light at the 620 nm wavelength that is similar to that associated with fluorescence of barium atoms in a single-vacancy matrix site in other work [27]. This excess is found on both surfaces of the sapphire window onto which a SXe sample is deposited, even when there is no barium ablation during the deposit. This could be due to the fact that the xenon gas contains barium atoms from earlier ablations that day.

One possible way to increase the barium signal is to decrease the temperature of the SXe sample. In [56], it was shown during annealing studies that the barium fluorescence decreases significantly with temperature for all matrix sites including the 619 nm single vacancy site. For the 619 nm fluorescence, the decrease was a factor of 10 from 11 K to 38 K. So it is possible that lower SXe temperatures will need to be achieved in order to see large barium signal in the matrix. It is possible that a decrease in temperature from roughly 140-150 K achieved with the JT probe to $\sim$80 K will result in a significant increase in fluorescence. A probe that uses liquid nitrogen to cool the tip would be able to reach $\sim$80 K. The system as it exists can be fitted with a liquid nitrogen probe. An effort to do this is underway. Liquid helium could also be used with this liquid probe to get down to or below 10 K.

There are a number of other fluorescence lines that have been observed in association with barium atoms or ions in a SXe matrix [24]. A convenient tool for exciting these transitions has been acquired in the form of a C-WAVE optical parametric oscillator (OPO) light source from Hübner Photonics [58]. In particular, barium ions have transitions that must be excited using blue light, which can be easily generated by the OPO. Barium ions will be drawn out of the LXe in a short period of time. Thus residual $Ba^+$ signal on the back side of the window or on either window side in a xenon-only deposit is not expected.

One of the main challenges going forward is to create a SXe layer that is not too thick and then lift it to the upper cell and cool it to liquid nitrogen temperatures or below. In order to do this, the pressure of the xenon gas will need to be manipulated as the sample is being cooled. As mentioned in Ch.3, the gas handling equipment is in place to do this. The ability to bring the pressure to a set-point was briefly tested and demonstrated, although no data was recorded at the time. The work in this thesis to measure and model both the SXe growth and GXe pressure during lifting will be pivotal input in developing a method to maintain the SXe sample at the desired thickness during the transit to the upper cell and during spectroscopic measurements.

Ultimately these efforts will need to incorporate the single barium imaging techniques being pursued with the barium ion beam. Already, single barium has been imaged in the single-vacancy

site. Work is ongoing to observe single barium images in other matrix sites. This work is critical as the distribution of matrix sites of single atom/ions extracted from a detector is not yet known. Once the extraction and observation of single barium atoms and ions has been improved in the lab enough, a probe apparatus will likely need to be tested for tagging efficiency. This means that an apparatus similar to that discussed in Ch. 3 will need to be built and operated in an accelerator facility.

In summary, a successful search for nucleon decay of $^{136}$Xe to $^{133}$Sb or $^{133}$Te was carried out using EXO-200 data. Work on barium tagging to extract barium ions or atoms in a SXe matrix on a Joule-Thomson probe was carried out. Efforts to observe fluorescence spectra of barium extracted in this way were not conclusive, but this and related efforts have laid the foundation for future work to achieve this milestone in barium tagging.

# Bibliography


[1] F. Reines C. L. Cowan Jr. et al. Detection of the free neutrino: A confirmation. *Science*, 124:103–104, 1956.

[2] J. Schechter and J. W. F. Valle. Neutrinoless double-beta decay in su(2)xu(1) theories. *Phys. Rev. D*, 25:2951–2954, Jun 1982.

[3] Frank T. Avignone, Steven R. Elliott, and Jonathan Engel. Double beta decay, majorana neutrinos, and neutrino mass. *Rev. Mod. Phys.*, 80:481–516, Apr 2008.

[4] A. G. Cohen and A. De Rújula. Scars on the cosmic background radiation? *The Astrophysical Journal*, 496(2):L63–L65, apr 1998.

[5] Sakharov A.D. Violation of cp invariance, c asymmetry, and baryon asymmetry of the universe. *Journal of Experimental and Theoretical Physics*, 1967.

[6] Joel Holdsworth. The feynman diagramen for the beta-negative decay of a neutronen into a proton, 2007.

[7] R. Davis et al. Measurement of the solar electron neutrino flux with the homestake chlorine detector. *The Astrophysical Journal*, 496:505–526, 1998.

[8] B. Aharmim et al. Combined analysis of all three phases of solar neutrino data from sudbury neutrino observatory. *Phys. Rev. C*, 88, 2013.

[9] M. Tanabashi et al. Review of particle physics. *Phys. Rev. D*, 98, 2018.

[10] JUNO collaboration.

[11] J. B. Albert et al. Improved measurement of the $2\nu\beta\beta$ half-life of $^{136}$Xe with the EXO-200 detector. *Phys. Rev. C*, 89:015502, Jan 2014.

[12] A. Gando et al. Search for Majorana Neutrinos Near the Inverted Mass Hierarchy Region with KamLAND-Zen. *Phys. Rev. Lett.*, 117:082503, 2016.

[13] Stefano Dell Oro et al. Neutrinoless double beta decay: 2015 review. *Advances in High Energy Physics*, 2016, 2016.

[14] M. Auger et al. The EXO-200 detector, part I: Detector design and construction. *J. Instrum.*, 7:P05010, 2012.

[15] J. B. Albert et al. Search for neutrinoless double-beta decay with the upgraded exo-200 detector. *Phys. Rev. Lett.*, 120:072701, Feb 2018.

[16] E. Conti et al. Correlated fluctuations between luminescence and ionization in liquid xenon. *Phys. Rev. B*, 68:054201, Aug 2003.

[17] J. B. Albert et al. Measurements of the ion fraction and mobility of alpha and beta decay products in liquid xenon using EXO-200. *Phys. Rev. C*, 92:045504, June 2015.

[18] J. B. Albert et al. Search for nucleon decays with exo-200. *Phys. Rev. D*, 97:072007, Apr 2018.

[19] H. Nishino et al. Search for Proton Decay via $p \to e^+\pi^0$ and $p \to \mu^+\pi^0$ in a Large Water Cherenkov Detector. *Phys. Rev. Lett.*, 102:141801, Apr 2009.

[20] K. Abe et al. Search for proton decay via $p \to \nu K^+$ using 260 kiloton·year data of Super-Kamiokande. *Phys. Rev. D*, 90:072005, Oct 2014.

[21] J. B. an others Albert. Investigation of radioactivity-induced backgrounds in exo-200. *Phys. Rev. C*, 92:015503, Jul 2015.

[22] S. Al Kharusi et al. The nEXO Pre-Conceptual Design Report. arxiv:1805.11142v2, 2018.

[23] J. B. Albert et al. Sensitivity and discovery potential of the proposed nexo experiment to neutrinoless double-Îš decay. *Phys. Rev. C*, 97:065503, Jun 2018.

[24] B. Mong et al. Spectroscopy of ba and $\mathrm{ba}^+$ deposits in solid xenon for barium tagging in nexo. *Phys. Rev. A*, 91:022505, Feb 2015.

[25] K. Twelker and S. Kravitz. Barium tagging from nexo using resonance ionization spectroscopy. *Physics Procedia*, 61:278 – 282, 2015. 13th International Conference on Topics in Astroparticle and Underground Physics, TAUP 2013.

[26] T. Brunner et al. An rf-only ion-funnel for extraction from high-pressure gases. *International Journal of Mass Spectrometry*, 379:110 – 120, 2015.

[27] C. Chambers et al. Imaging individual barium atoms in solid xenon for barium tagging in nexo. *Nature*, 2019.

[28] Christopher Chambers. *Imaging Individual Barium Atoms in Solid Xenon by Scannin of a Focused Laser for us in the nEXO Experiment*. PhD thesis, Colorado State University, 2019.

[29] J. B. Albert et al. Search for Majorana neutrinos with the first two years of EXO-200 data. *Nature*, 510:229, Jun 2014.

[30] J. B. Albert et al. Search for Majoron-emitting modes of double-beta decay of $^{136}$Xe with EXO-200. *Phys. Rev. D*, 90:092004, Nov 2014.

[31] M. Agostini et al. Background-free search for neutrinoless double-beta decay of $^{76}$Ge with GERDA. *Nature*, 544:47–52, April 2017.

[32] C. McGrew et al. Search for nucleon decay using the IMB-3 detector. *Phys. Rev. D*, 59:052004, Feb 1999.

[33] R. Bernabei et al. Search for rare processes with DAMA/LXe experiment at Gran Sasso. *The European Physical Journal A - Hadrons and Nuclei*, 27(1):35–41, 2006.

[34] H.O. Back et al. New limits on nucleon decays into invisible channels with the BOREXINO counting test facility. *Phys. Lett. B*, 563(1âĂŞ2):23 – 34, 2003.

[35] R. Bernabei et al. Search for the nucleon and di-nucleon decay into invisible channels. *Phys. Lett. B*, 493(1âĂŞ2):12 – 18, 2000.

[36] H. Braun et al. Absolute Gamma-Ray Line Intensities and Branching Ratios in Mass Chain 133. *Radiochimica Acta*, 36(3):95–102, 1984.

[37] Rene Brun and Fons Rademakers. Root an object oriented data analysis framework. *Nuclear Instruments and Methods in Physics Research Section A: Accelerators, Spectrometers, Detectors and Associated Equipment*, 389(1):81 – 86, 1997. New Computing Techniques in Physics Research V.

[38] G. van Rossum. Python tutorial. *Technical Report CS-R9526, Centrum voor Wiskunde en Informatica (CWI), Amsterdam*, May 1995.

[39] F. James and M. Roos. Minuit: A System for Function Minimization and Analysis of the Parameter Errors and Correlations. *Comput. Phys. Commun.*, 10:343–367, 1975.

[40] K.S. Babu, Ilia Gogoladze, and Kai Wang. Gauged baryon parity and nucleon stability. *Phys. Lett. B*, 570(1âĂŞ2):32 – 38, 2003.

[41] J.F. Zielger, M.D. Ziegler, and J.P. Biersack. SRIM-The stopping and range of ions in matter. *Nucl. Instrum. Methods. A*, 268:1818–1823, 2010.

[42] J. Allison et al. Recent Developements in Geant4. *Nucl. Instrum. Methods. A*, 835:186 – 225, 2016.

[43] http://www.galilmedical.com Galil Medical Cryoblation Needles.

[44] USA Meller Optics, www.melleroptics.com Providence RI.

[45] K. Hall. *In-Situ Laser Tagging of Barium Ions in Liquid Xenon for the EXO Experiment*. PhD thesis, Colorado State University, 2012.

[46] J.C. Benitez Medina. *Mobility and Fluorescence of Barium Ions in Xenon Gas for tthe EXO Experiment*. PhD thesis, Colorado State University, 2013.

[47] S.C. Jeng. *New Fluorescence Technique to Search for Neutrino Masses by identification of $0\nu\beta\beta$ $^{136}Ba^{+}$ Ion Daughters in Liquid Xenon*. PhD thesis, Colorado State University, 2004.

[48] USA Lakeshore Cryotronics Inc. www.lakeshore.com Westerville OH.

[49] https://www.advancedspecialtygases.com/ Advanced specialty gases.

[50] https://www.mksinst.com/c/capacitance-manometers Baratron Capacitance Manometers.

[51] USA Applied Motion Products www.applied-motion.com Watsonville CA.

[52] Accu-Glass Products https://www.accuglassproducts.com/wire-and-cable/uhv-kapton

[53] SIMION 8.0 http://www.simion.com.

[54] https://www.coherent.com/lasers/laser/verdi-v-series Verdi V Series V8.

[55] https://www.roperscientific.de/Spec10.html Spec-10 LN Cooled Spectroscopy Detector.

[56] Timothy Walton. *Imaging Single Barium Atoms in Solid Xenon for Barium Tagging in the nEXO Neutrinoless Double Beta Decay Experiment*. PhD thesis, Colorado State University, 2016.

[57] https://www.picoquant.com/products/category/photon-counting-instrumentation Time-Correlated Single Photon Counting.

[58] Hübner Photonics https://www.hubner-photonics.com/products/laser-technology/tunable lasers/.